

Photometric and Spectroscopic Properties of Type Ia Supernova 2018oh with Early Excess Emission from the *Kepler 2* Observations

```
W. Li<sup>1,2</sup>, X. Wang<sup>1</sup>, J. Vinkó<sup>3,4,5</sup>, J. Mo<sup>1</sup>, G. Hosseinzadeh<sup>2,6,7</sup>, D. J. Sand<sup>8</sup>, J. Zhang<sup>9,10,11</sup>, H. Lin<sup>1</sup>
                                                                                                              PTSS/TNTS,
    T. Zhang<sup>12</sup>, L. Wang<sup>13,14</sup>, J. Zhang<sup>1</sup>, Z. Chen<sup>1</sup>, D. Xiang<sup>1</sup>, L. Rui<sup>1</sup>, F. Huang<sup>1,15</sup>, X. Li<sup>1</sup>, X. Zhang<sup>1</sup>, L. Li<sup>1</sup>, E. Baron<sup>16</sup>,
                                                            J. M. Derkacy<sup>16</sup>, X. Zhao<sup>17</sup>, H. Sai<sup>1</sup>, K. Zhang<sup>1,5</sup>, L. Wang<sup>12,18</sup>
                              LCO, D. A. Howell<sup>2,6</sup>, C. McCully<sup>2</sup>, I. Arcavi<sup>2,6,19,77</sup>, S. Valenti<sup>20</sup>, D. Hiramatsu<sup>2,6</sup>, J. Burke<sup>2,6</sup>
                                                                                                                    KEGS,
A. Rest<sup>21,22</sup>, P. Garnavich<sup>23</sup>, B. E. Tucker<sup>24,25,26</sup>, G. Narayan<sup>21,78</sup>, E. Shaya<sup>27</sup>, S. Margheim<sup>28</sup>, A. Zenteno<sup>29</sup>, A. Villar<sup>7</sup>
G. Dimitriadis<sup>30</sup>, R. J. Foley<sup>30</sup>, Y.-C. Pan<sup>30</sup>, D. A. Coulter<sup>30</sup>, O. D. Fox<sup>21</sup>, S. W. Jha<sup>31</sup>, D. O. Jones<sup>30</sup>, D. N. Kasen<sup>32,33</sup>, C. D. Kilpatrick<sup>30</sup>, A. L. Piro<sup>34</sup>, A. G. Riess<sup>21,22</sup>, C. Rojas-Bravo<sup>30</sup>
    ASAS-SN,

B. J. Shappee<sup>35</sup>, T. W.-S. Holoien<sup>34,79</sup>, K. Z. Stanek<sup>36,37</sup>, M. R. Drout<sup>34,80,81</sup>, K. Auchettl<sup>36,38</sup>, C. S. Kochanek<sup>36,37</sup>, J. S. Brown<sup>37</sup>, S. Bose<sup>39</sup>, D. Bersier<sup>40</sup>, J. Brimacombe<sup>41</sup>, P. Chen<sup>39</sup>, S. Dong<sup>39</sup>, S. Holmbo<sup>42</sup>, J. A. Muñoz<sup>43,44</sup>, R. L. Mutel<sup>45</sup>, R. S. Post<sup>46</sup>, J. L. Prieto<sup>47,48</sup>, J. Shields<sup>37</sup>, D. Tallon<sup>45</sup>, T. A. Thompson<sup>36,37</sup>, P. J. Vallely<sup>37</sup>,
                                                                                                          S. Villanueva, Jr. 37
                                                                                                              Pan-STARRS,
            S. J. Smartt<sup>49</sup>, K. W. Smith<sup>50</sup>, K. C. Chambers<sup>51</sup>, H. A. Flewelling<sup>51</sup>, M. E. Huber<sup>51</sup>, E. A. Magnier<sup>51</sup>, C. Z. Waters<sup>51</sup>, A. S. B. Schultz<sup>51,52</sup>, J. Bulger<sup>51</sup>, T. B. Lowe<sup>51</sup>, M. Willman<sup>51</sup>
                                                                                                            Konkoly/Texas,
 K. Sárneczky<sup>3</sup>, A. Pál<sup>3</sup>, J. C. Wheeler<sup>14,53</sup>, A. Bódi<sup>3</sup>, Zs. Bognár<sup>3</sup>, B. Csák<sup>3</sup>, B. Cseh<sup>3</sup>, G. Csörnyei<sup>3</sup>, O. Hanyecz<sup>3</sup>,
  B. Ignácz<sup>3</sup>, Cs. Kalup<sup>3</sup>, R. Könyves-Tóth<sup>3</sup>, L. Kriskovics<sup>3</sup>, A. Ordasi<sup>3</sup>, I. Rajmon<sup>54</sup>, A. Sódor<sup>3</sup>, R. Szabó<sup>3,52</sup>, R. Szakáts<sup>3</sup>, R. Szakáts<sup>3</sup>
                                                                                                                   G. Zsidi<sup>3</sup>
                                                                                                      University of Arizona,
                                                                         P. Milne<sup>8</sup>, J. E. Andrews<sup>8</sup>, N. Smith<sup>8</sup>, C. Bilinski<sup>8</sup>
                                                                                                                      Swift,
                                                                                                          P. J. Brown 14,55
                                                                                                                 ePESSTO.
 J. Nordin<sup>56</sup>, S. C. Williams<sup>57</sup>, L. Galbany<sup>58</sup>, J. Palmerio<sup>59</sup>, I. M. Hook<sup>57</sup>, C. Inserra<sup>60</sup>, K. Maguire<sup>61</sup>, Régis Cartier<sup>62</sup>, A. Razza<sup>63,64</sup>, C. P. Gutiérrez<sup>65</sup>
                                                                                               University of North Carolina,
                                                                              J. J. Hermes<sup>66,80</sup>, J. S. Reding<sup>66</sup>, B. C. Kaiser<sup>66</sup>
                                                                                                                   ATLAS.
                                               J. L. Tonry<sup>35</sup>, A. N. Heinze<sup>35</sup>, L. Denneau<sup>35</sup>, H. Weiland<sup>35</sup>, B. Stalder<sup>67</sup>
                                                                                                          K2 Mission Team,
        G. Barentsen<sup>68,69</sup>, J. Dotson<sup>68</sup>, T. Barclay<sup>70,71</sup>, M. Gully-Santiago<sup>68,69</sup>, C. Hedges<sup>68,69</sup>, A. M. Cody<sup>68,69</sup>
                                                                                                              S. Howell<sup>72</sup>
      Kepler Spacecraft Team,

J. Coughlin<sup>72,73</sup>, J. E. Van Cleve<sup>72,73</sup>, J. Vinícius de Miranda Cardoso<sup>72,74</sup>, K. A. Larson<sup>75</sup>, K. M. McCalmont-Everton<sup>75</sup>,

C. A. Peterson<sup>75</sup>, S. E. Ross<sup>75</sup>, L. H. Reedy<sup>76</sup>, D. Osborne<sup>76</sup>, C. McGinn<sup>76</sup>, L. Kohnert<sup>76</sup>, L. Migliorini<sup>76</sup>, A. Wheaton<sup>76</sup>,

B. Spencer<sup>76</sup>, C. Labonde<sup>76</sup>, G. Castillo<sup>76</sup>, G. Beerman<sup>76</sup>, K. Steward<sup>76</sup>, M. Hanley<sup>76</sup>, R. Larsen<sup>76</sup>, R. Gangopadhyay<sup>76</sup>,
R. Kloetzel<sup>76</sup>, T. Weschler<sup>76</sup>, V. Nystrom<sup>76</sup>, J. Moffatt<sup>76</sup>, M. Redick<sup>76</sup>, K. Griest<sup>76</sup>, M. Packard<sup>76</sup>, M. Muszynski<sup>76</sup>, J. Kampmeier<sup>76</sup>, R. Bjella<sup>76</sup>, S. Flynn<sup>76</sup>, and B. Elsaesser<sup>76</sup>

Physics Department and Tsinghua Center for Astrophysics (THCA), Tsinghua University, Beijing, 100084, People's Republic of China
                                                            Las Cumbres Observatory, 6740 Cortona Dr. Ste. 102, Goleta, CA 93117-5575, USA
                                                     <sup>3</sup> Konkoly Observatory, MTA CSFK, Konkoly Thege M. ut 15-17, Budapest, 1121, Hungary
                                           <sup>4</sup> Department of Optics & Quantum Electronics, University of Szeged, Dom ter 9, Szeged, 6720 Hungary
                                                            <sup>5</sup> Department of Astronomy, University of Texas at Austin, Austin, TX 78712, USA
                                                        <sup>6</sup> Department of Physics, University of California, Santa Barbara, CA 93106-9530, USA
                                                  <sup>7</sup> Harvard-Smithsonian Center for Astrophysics, 60 Garden Street, Cambridge, MA 02138, USA
                                   Steward Observatory, University of Arizona, 933 North Cherry Avenue, Rm. N204, Tucson, AZ 85721-0065, USA
                                        Yunnan Observatories (YNAO), Chinese Academy of Sciences, Kunming 650216, People's Republic of China
         10 Key Laboratory for the Structure and Evolution of Celestial Objects, Chinese Academy of Sciences, Kunming 650216, People's Republic of China
    11 Center for Astronomical Mega-Science, Chinese Academy of Sciences, 20A Datun Road, Chaoyang District, Beijing, 100012, People's Republic of China
```

```
<sup>12</sup> National Astronomical Observatory of China, Chinese Academy of Sciences, Beijing, 100012, People's Republic of China
                            <sup>13</sup> Purple Mountain Observatory, Chinese Academy of Sciences, Nanjing 210034, People's Republic of China
<sup>14</sup> George P. and Cynthia Woods Mitchell Institute for Fundamental Physics & Astronomy, Texas A&M University, Department of Physics and Astronomy, 4242
                                                                TAMU, College Station, TX 77843, USA
         <sup>15</sup> Department of Astronomy, School of Physics and Astronomy, Shanghai Jiao Tong University, Shanghai 200240, People's Republic of China
                                Homer L. Dodge Department of Physics and Astronomy, University of Oklahoma, Norman, OK, USA
                                   School of Science, Tianjin University of Technology, Tianjin, 300384, People's Republic of China
  18 Chinese Academy of Sciences South America Center for Astronomy, China-Chile Joint Center for Astronomy, Camino El Observatorio 1515, Las Condes,
                                                                              Santiago, Chile
                       <sup>19</sup> The Raymond and Beverly Sackler School of Physics and Astronomy, Tel Aviv University, Tel Aviv 69978, Israel

Department of Physics, University of California, Davis, CA 95616, USA
                                      <sup>21</sup> Space Telescope Science Institute, 3700 San Martin Drive, Baltimore, MD 21218, USA
                                  Department of Physics and Astronomy, Johns Hopkins University, Baltimore, MD 21218, USA
                      <sup>23</sup> Department of Physics, University of Notre Dame, 225 Nieuwland Science Hall, Notre Dame, IN 46556-5670, USA
      The Research School of Astronomy and Astrophysics, Mount Stromlo Observatory, Australian National University, Canberra, ACT 2611, Australia
                         National Centre for the Public Awareness of Science, Australian National University, Canberra, ACT 2611, Australia
                                    The ARC Centre of Excellence for All-Sky Astrophysics in 3 Dimension (ASTRO 3D), Australia
                                          Astronomy Department, University of Maryland, College Park, MD 20742-2421, USA
                                   28 Gemini Observatory, Southern Operations Center, c/o AURA, Casilla 603, La Serena, Chile
                                                 Cerro Tololo Inter-American Observatory, Casilla 603, La Serena, Chile
                               <sup>30</sup> Department of Astronomy and Astrophysics, University of California, Santa Cruz, CA 95064, USA
          <sup>31</sup> Department of Physics and Astronomy, Rutgers, The State University of New Jersey, 136 Frelinghuysen Road, Piscataway, NJ 08854, USA
                                          Department of Astronomy, University of California, Berkeley, CA 94720-3411, USA
                                                   Lawrence Berkeley National Laboratory, Berkeley, CA 94720, USA
                           The Observatories of the Carnegie Institution for Science, 813 Santa Barbara St., Pasadena, CA 91101, USA
                                   Institute for Astronomy, University of Hawai'i, 2680 Woodlawn Drive, Honolulu, HI 96822, USA
          <sup>36</sup> Center for Cosmology and AstroParticle Physics (CCAPP), The Ohio State University, 191 W. Woodruff Ave., Columbus, OH 43210, USA
                              Department of Astronomy, The Ohio State University, 140 West 18th Avenue, Columbus, OH 43210, USA
                           Department of Physics, The Ohio State University, 191 W. Woodruff Avenue, Columbus, OH 43210, USA
   Kavli Institute for Astronomy and Astrophysics, Peking University, Yi He Yuan Road 5, Hai Dian District, Beijing 100871, People's Republic of China 40 Astrophysics, Peccasch Letitute, Liverpool Lohn Moores University, 146 Provenow Hill Liverpool L3 5RF, LIK
                            Astrophysics Research Institute, Liverpool John Moores University, 146 Brownlow Hill, Liverpool L3 5RF, UK
                                                        Coral Towers Observatory, Cairns, QLD 4870, Australia
                         Department of Physics and Astronomy, Aarhus University, Ny Munkegade 120, DK-8000 Aarhus C, Denmark Departamento de Astronomía y Astrofísica, Universidad de Valencia, E-46100 Burjassot, Valencia, Spain
                                        <sup>4</sup> Observatorio Astronómico, Universidad de Valencia, E-46980 Paterna, Valencia, Spain
                                      Department of Physics and Astronomy, University of Iowa, Iowa City, IA 52242, USA
Post Observatory, Lexington, MA 02421, USA
                        <sup>47</sup> Núcleo de Astronomía de la Facultad de Ingeniería, Universidad Diego Portales, Av. Ejército 441, Santiago, Chile Millennium Institute of Astrophysics, Santiago, Chile
               49 Astrophysics Research Centre, School of Mathematics and Physics, Queen's University Belfast, Northern Ireland, BT7 1NN, UK
50 Queen's University Belfast, Northern Ireland, BT7 1NN, UK
                           <sup>51</sup> Institute for Astronomy, University of Hawaii at Manoa, 2680 Woodlawn Drive, Honolulu, HI 96822, USA
                                            MTA CSFK Lendület Near-Field Cosmology Research Group, Budapest, Hungary
                                         MTA CSFR Lenduict red - Line Cosmology Recent Strain, Austin, TX 78712, USA
                                            <sup>54</sup>Berzsenyi Dániel High School, Kárpát utca 49-53, Budapest, 1133, Hungary
                         55 Department of Physics and Astronomy, Texas A&M University, 4242 TAMU, College Station, TX 77843, USA
                                    Institute of Physics, Humboldt-Universität zu Berlin, Newtonstr. 15, D-12489 Berlin, Germany
                                                   Physics Department, Lancaster University, Lancaster LA1 4 YB, UK
                            <sup>58</sup> PITT PACC, Department of Physics and Astronomy, University of Pittsburgh, Pittsburgh, PA 15260, USA
         59 Sorbonne Universités, UPMC Univ. Paris 6 et CNRS, UMR 7095, Institut d'Astrophysique de Paris, 98 bis bd Arago, F-75014 Paris, France
60 Department of Physics and Astronomy, University of Southampton, Southampton, SO17 1BJ, UK
                     <sup>61</sup> Astrophysics Research Centre, School of Mathematics and Physics, Queen's University Belfast, Belfast BT7 1NN, UK
                          Cerro Tololo Inter-American Observatory, National Optical Astronomy Observatory, Casilla 603, La Serena, Chile
                                         European Southern Observatory, Alonso de Córdova 3107, Casilla 19, Santiago, Chile
                         <sup>64</sup> Departamento de Astronomía, Universidad de Chile, Camino El Observatorio 1515, Las Condes, Santiago, Chile
                                                       <sup>65</sup> University of Southampton, Southampton, SO17 1BJ, UK
                               <sup>66</sup> Department of Physics and Astronomy, University of North Carolina, Chapel Hill, NC 27599, USA
                                                        LSST, 950 North Cherry Avenue, Tucson, AZ 85719, USA
                                          <sup>68</sup> NASA Ames Research Center, Moffett Blvd., Mountain View, CA 94035, USA
                                     <sup>69</sup> Bay Area Environmental Research Institute, P.O. Box 25, Moffett Field, CA 94035, USA
<sup>70</sup> NASA Goddard Space Flight Center, 8800 Greenbelt Rd., Greenbelt, MD 20771, USA
                                    71 University of Maryland, Baltimore County, 1000 Hilltop Cir., Baltimore, MD 21250, USA
                                                      NASA Ames Research Center, Moffett Field, CA 94035, USA
                                              73 SETI Institute, 189 Bernardo Avenue, Mountain View, CA 94043, USA
                                                   <sup>4</sup> Universidade Federal de Campina Grande, Campina Grande, Brazil
                                                 <sup>75</sup> Ball Aerospace and Technologies Corp., Boulder, CO 80301, USA
                                                <sup>76</sup> LASP, University of Colorado at Boulder, Boulder, CO 80303, USA
                             Received 2018 July 31; revised 2018 October 12; accepted 2018 October 12; published 2018 December 28
```

Einstein Fellow.

⁷⁸ Lasker Fellow.

⁷⁹ Carnegie Fellow.

⁸⁰ Hubble Fellow.

⁸¹ Dunlap Fellow.

Abstract

Supernova (SN) 2018oh (ASASSN-18bt) is the first spectroscopically confirmed Type Ia supernova (SN Ia) observed in the *Kepler* field. The *Kepler* data revealed an excess emission in its early light curve, allowing us to place interesting constraints on its progenitor system. Here we present extensive optical, ultraviolet, and near-infrared photometry, as well as dense sampling of optical spectra, for this object. SN 2018oh is relatively normal in its photometric evolution, with a rise time of 18.3 ± 0.3 days and $\Delta m_{15}(B) = 0.96 \pm 0.03$ mag, but it seems to have bluer B - V colors. We construct the "UVOIR" bolometric light curve having a peak luminosity of 1.49×10^{43} erg s⁻¹, from which we derive a nickel mass as $0.55 \pm 0.04 \, M_{\odot}$ by fitting radiation diffusion models powered by centrally located ⁵⁶Ni. Note that the moment when nickel-powered luminosity starts to emerge is +3.85 days after the first light in the *Kepler* data, suggesting other origins of the early-time emission, e.g., mixing of ⁵⁶Ni to outer layers of the ejecta or interaction between the ejecta and nearby circumstellar material or a nondegenerate companion star. The spectral evolution of SN 2018oh is similar to that of a normal SN Ia but is characterized by prominent and persistent carbon absorption features. The C II features can be detected from the early phases to about 3 weeks after the maximum light, representing the latest detection of carbon ever recorded in an SN Ia. This indicates that a considerable amount of unburned carbon exists in the ejecta of SN 2018oh and may mix into deeper layers.

Key words: supernovae: general – supernovae: individual (SN 2018oh)

1. Introduction

Type Ia supernovae (SNe Ia) have been used as standardizable candles for measuring cosmic expansion, leading to the discovery of the accelerating expansion of the universe and hence the "mysterious" dark energy (Riess et al. 1998; Perlmutter et al. 1999). However, the exact nature of their progenitor systems is still highly controversial (Wang et al. 2013; Maoz et al. 2014). Two popular scenarios have been proposed so far for SN Ia progenitors. One is an explosion of a carbon-oxygen (CO) white dwarf (WD) that accretes hydrogen- or helium-rich materials from a nondegenerate companion that could be a main-sequence star, a red giant, or even a helium star (Whelan & Iben 1973; Nomoto 1982; Nomoto et al. 1997). This single-degenerate (SD) scenario is favored by possible detections of circumstellar material (CSM) around some SNe Ia (Hamuy et al. 2003; Aldering et al. 2006; Patat et al. 2007; Sternberg et al. 2011; Dilday et al. 2012; Maguire et al. 2013; Silverman et al. 2013). It is disfavored by the lack of narrow hydrogen emission lines in late-time spectra (Mattila et al. 2005; Leonard 2007; Shappee et al. 2013; Maguire et al. 2016). The other scenario involves the merging explosion of two WDs, dubbed a double-degenerate (DD) scenario (Iben & Tutukov 1984; Webbink 1984). The DD model has recently gained more attention due to the observational findings that there are no companion signatures for some SNe Ia, including the nearby object SN 2011fe and the supernova remnants SN 1006 and SNR 0509-67.5 in the Large Magellanic Cloud, down to the luminosity that is much fainter than the Sun (Li et al. 2011; González Hernández et al. 2012; Schaefer & Pagnotta 2012). Some population synthesis calculations predict delay-time distribution shapes for the birth rate of SNe Ia in the DD scenario, which are consistent with observations (Mennekens et al. 2010; Toonen et al. 2012).

The SNe Ia also show increasing diversity in their spectroscopic and photometric properties. For instance, members of the so-called high-velocity (HV) subclass are found to have larger ejecta velocities, redder peak B-V colors, and slower late-time decline rates at bluer wavelengths than those with normal ejecta velocities (Wang et al. 2008, 2009b; Foley & Kasen 2011; Foley et al. 2011; Foley 2012; Mandel et al. 2014). The observed differences between the HV and normal SNe Ia have been interpreted as a geometric consequence of asymmetric explosions (Maeda et al. 2010; Maund et al. 2010).

However, the fact that the HV subclass tends to be associated with more metal-rich and luminous stellar environments indicates that SNe Ia likely arise from more than one progenitor population (Wang et al. 2013).

Very early observations of SNe Ia can provide clues to distinguish different progenitor models. According to the theoretical analysis by Kasen (2010), the collision between the material ejected by the SN and a nondegenerate companion star will produce extra emission, leading to a "bump" feature in the early-time light curves. This amount depends on the viewing angle, companion size, and separation. Possible detections of such bump features have been reported for SNe 2012cg (Marion et al. 2016; although see Shappee et al. 2018a), iPTF14atg (Cao et al. 2015), iPTF16abc (Miller et al. 2018), and 2017cbv (Hosseinzadeh et al. 2017; although see Sand et al. 2018), indicating that they might have SD progenitor systems. Of these, iPTF14atg is a peculiar lowluminosity SN like SN 2002es (Ganeshalingam et al. 2012) and is not representative of normal SNe Ia. Miller et al. (2018) suggested the early flux of iPTF16abc can be explained by the collision of the SN with nearby material and/or strong mixing of ⁵⁶Ni in the SN ejecta. For SN 2017cbv, however, the collision of SN ejecta with a nondegenerate companion star matches well with the optical observations but overpredicts the UV flux.

The *Kepler Space Telescope*, observing with a time resolution of 30 minutes, can be an extremely powerful tool for finding excess early-time emission (Haas et al. 2010). Olling et al. (2015) studied the *Kepler* light curves of three SNe Ia, and they found no signatures of ejecta—companion interaction in the early phase of the explosions. This is consistent with DD models. However, further studies of these SNe were limited by the lack of prompt follow-up observations by other facilities.

An SN Ia in the face-on spiral galaxy UGC 4780 (see Figure 1) at a distance of about \sim 53 Mpc ($z \sim 0.0109$), SN 2018oh (ASASSN-18bt) provides us a rare opportunity to examine the progenitor of an SN Ia system through the observed properties based on both continuous *Kepler* data and extensive follow-up observations. This SN was discovered by the All Sky Automated Survey for SuperNovae (ASAS-SN; Shappee et al. 2014) on 2018 February 4.41 (UT time is used throughout this paper) at R.A. = $09^h06^m39^s59$, decl. = $+19^\circ$

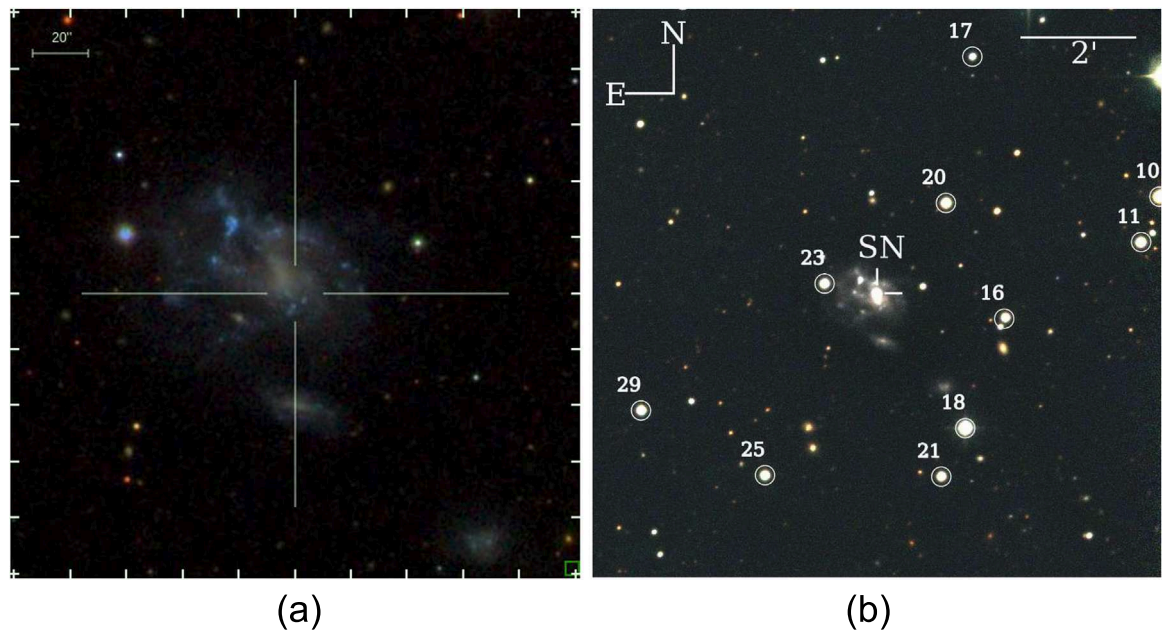


Figure 1. (a) Pre-explosion image from the SDSS. (b) Image of SN 2018oh in UGC 4780, taken with the TNT. Some of the reference stars listed in Table 1 are marked. North is up and east is to the left.

20'17.''47 (Brown et al. 2018; Shappee et al. 2018b), located at 2.''0 east and 7.''8 north of the center of UGC 4780. It was soon identified as a normal SN Ia at about 10 days before the maximum light (Leadbeater 2018; Zhang et al. 2018). The ASAS-SN monitors the K2 fields at heightened cadence to help identify such SNe at the earliest possible phases for detailed study. The excess flux above a quadratic rise detected in the early rising phase of the *Kepler* light curve cannot be well modeled as a single power law. This is alternately explained as the collision of the SN ejecta with a nondegenerate $1-6 M_{\odot}$ Roche-lobe-filling star at 2×10^{12} cm (Dimitriadis et al. 2018; but see the caveats in Shappee et al. 2018b).

In this paper, we present extensive follow-up observations of SN 2018oh in the optical, ultraviolet (UV), and near-infrared (NIR) bands and analyze its observational properties and explosion parameters in contrast to other well-studied SNe Ia. The observations and data reductions are described in Section 2, Section 3 presents the light/color curves, and Section 4 presents the spectral evolution. We discuss the properties of SN 2018oh and its explosion parameters in Section 5. The conclusions are summarized in Section 6.

2. Observations

2.1. Photometry

After the discovery of SN 2018oh and the recognition that it would have a *Kepler* light curve, follow-up photometric observations started immediately using more than a dozen telescopes, including the (1) 0.8 m Tsinghua-NAOC Telescope (TNT) in China (Huang et al. 2012); (2) 2.4 m Lijiang Telescope (LJT) of Yunnan Astronomical Observatory (YNAO) in China (Fan et al. 2015); (3) Las Cumbres Observatory (LCO) 1 m telescope network (Brown et al. 2013); (4) Pan-STARRS1 survey (PS1) telescopes (Chambers et al. 2016); (5) Swope 1.0 m telescope at Las Campanas Observatory; (6) DEMONEXT 0.5 m telescope (Villanueva et al. 2018); (7) 0.61 m at Post Observatory (PONM), Mayhill, NM; (8) 60/90 cm Schmidt telescope on Piszkéstető Mountain Station of Konkoly Observatory in

Hungary; (9) Gemini 0.51 m telescope at the Winer Observatory; (10) CTIO 4 m Blanco telescope with DECam (Honscheid et al. 2008; Flaugher et al. 2015); (11) 0.51 m T50 at the Astronomical Observatory of the University of Valencia in Spain; and (12) 0.6 m Super-LOTIS (Livermore Optical Transient Imaging System; Williams et al. 2008) telescope at Kitt Peak Steward Observatory. Broadband *BV*- and Sloan *gri*-band photometry were obtained with all of these telescopes except the 60/90 cm Schmidt telescope of Konkoly Observatory and the 0.6 m Super-LOTIS telescope, which both used the *BVRI* bands. Observations made with the LCO 1 m telescope and Swope also used the *U* and *u* bands, respectively.

All CCD images were preprocessed using standard IRAF⁸² routines, including bias subtraction, flat fielding, and the removal of cosmic rays. No template-subtraction technique was applied in measuring the magnitudes, as the SN was still relatively bright in preparation of this work. We performed point-spread function (PSF) photometry for both the SN and the reference stars using the pipeline *Zuruphot* developed for automatic photometry on the TNT, LJT, LCO, DEMONEXT, PONM, Gemini, and T50 images (J. Mo et al. 2018, in preparation). This pipeline was modified to analyze the data obtained with the other telescopes involved in our study. All Swope imaging was processed using photpipe (Rest et al. 2005, 2014).

The instrumental magnitudes of the SN were converted into the standard Johnson *UBV* (Johnson et al. 1966), Kron-Cousins *RI* (Cousins 1981), and Sloan *gri* systems using observations of a series of Landolt (1992) and SDSS/PS1 (Chambers et al. 2016; Flewelling et al. 2016; Magnier et al. 2016; Waters et al. 2016; Albareti et al. 2017) standard stars on a few photometric nights. We transformed the PS1 *gri*-band magnitudes to the Swope natural system (see, e.g., Contreras et al. 2010;

⁸² IRAF is distributed by the National Optical Astronomy Observatories, which are operated by the Association of Universities for Research in Astronomy, Inc., under cooperative agreement with the National Science Foundation (NSF).

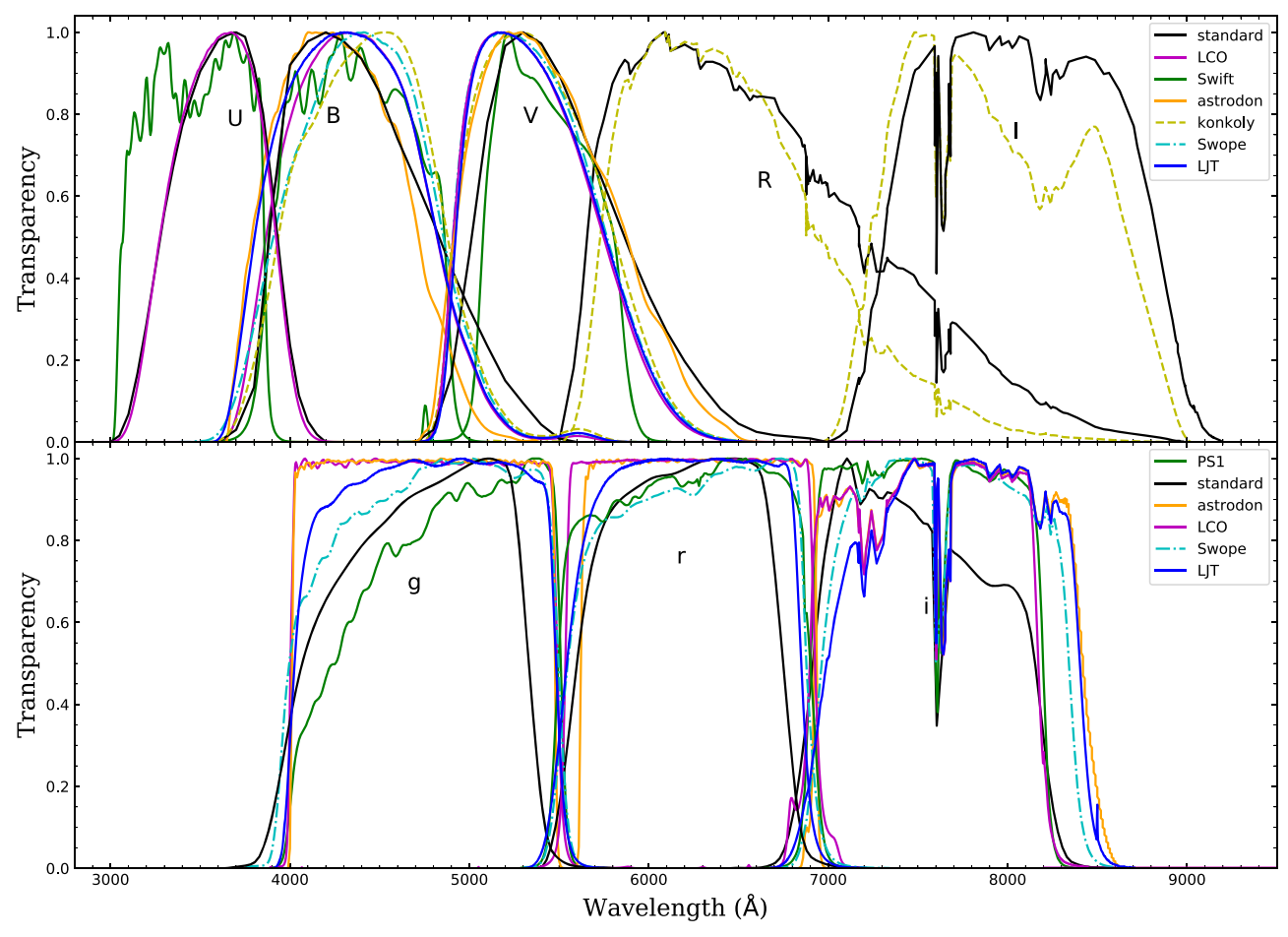


Figure 2. Transmission curves of different telescopes. Curves are normalized to the peak. Black curves represent the standard filter transmission curves.

Krisciunas et al. 2017) using Supercal transformations as described in Scolnic et al. (2015). The filter transmission curves of different telescopes, which are not far from the standard ones, are displayed in Figure 2. These filter transmissions are multiplied by the CCD quantum efficiency and atmospheric transmission when information on the latter two is available. The Astrodon filters are used by the PONM and Gemini observations. Tables 1 and 2 list the standard UBVRI and gri magnitudes of the comparison stars. The photometric results for the different photometric systems are consistent to within 0.05 mag after applying the color-term corrections. As the instrumental responses from the different photometric systems do not show noticeable differences, as shown in Figure 2, we did not apply additional corrections (i.e., S-corrections) to the photometry due to the lack of telescope information such as CCD quantum efficiency and the mirror reflectivity for some telescopes. The final calibrated U(u)BVRIgri magnitudes are presented in Table 3.

The NIR photometry of SN 2018oh was obtained with two telescopes, the 3.6 m ESO New Technology Telescope (NTT) with SOFI and the 1.3 m CTIO telescope with ANDICAM. The *JHK*-band photometry from the NTT was reduced using the SOFI reduction pipeline and calibrated against the 2MASS stars in the field. The *YJH*-band images obtained with the CTIO 1.3 m telescope were first subtracted with the sky background and then reduced with SExtractor (Bertin & Arnouts 1996). Magnitudes were then calibrated with the 2MASS catalog in the *JH* bands

and the Pan-STARRS catalog in the *Y* band. The final NIR magnitudes are listed in Table 4.

SN 2018oh was also observed with the Ultraviolet/Optical Telescope (UVOT; Roming et al. 2005) onboard the Neil Gehrels Swift Observatory (Swift; Gehrels et al. 2004). The space-based observations were obtained in the uvw1, uvm2, uvw2, U, B, and V filters, starting from 2018 February 05.4. The Swift/UVOT data reduction is based on that of the Swift Optical Ultraviolet Supernova Archive (SOUSA; Brown et al. 2014). A 3" aperture is used to measure the source counts with an aperture correction based on an average PSF. Magnitudes are computed using the zero points of Breeveld et al. (2011) for the UV and Poole et al. (2008) for the optical and the 2015 redetermination of the temporal sensitivity loss. Table 5 lists the final background-subtracted UVOT UV/ optical magnitudes. The instrumental response curves of the UVOT B and V bands are similar to those of the standard Johnson B and V bands. Therefore, our ground-based and Swift photometry of these two bands can be compared directly. Note that some differences exist between the *U*-band observations of Swift UVOT and LCO due to different transmission curves (see Figure 2).

2.2. Spectroscopy

A total of 56 optical spectra were obtained from the Xinglong 2.16 m telescope (+BFOSC), the LJT 2.4 m

Table 1 Photometric Standards in the SN 2018oh Field 1^a

Num.	α(J2000)	δ(J2000)	U (mag)	B (mag)	V (mag)	g (mag)	r (mag)	i (mag)
1	09h05m59 s 52	+19°15′08″52	17.207(045)	16.391(156)	15.528(022)	15.839(004)	15.111(003)	14.839(001)
2	09 ^h 05 ^m 59 ^s .95	+19°20′47.″95	17.495(234)	17.294(136)	16.594(018)	16.787(004)	16.278(003)	16.091(004)
3	09h06m02 s 44	+19°25′11.″44	14.466(128)	14.265(012)	13.785(036)	•••	•••	
4	09h06m02 s 74	+19°22′59″74	16.876(225)	16.411(136)	15.682(063)	15.889(002)	15.377(002)	15.189(003)
5	09 ^h 06 ^m 05 ^s 30	+19°15′21.″30	18.374(121)	17.322(161)	16.094(030)	16.637(005)	15.538(001)	14.899(003)
6	09h06m08:24	+19°23′45″24	14.683(130)	14.562(093)	14.089(051)	14.177(003)	13.877(001)	13.754(007)
7	09 ^h 06 ^m 09 ^s .43	+19°19′47″43	16.944(205)	16.190(108)	15.371(027)	15.612(002)	14.998(003)	14.777(002)
8	09h06m09 s. 72	+19°26′37″72	14.249(157)	14.085(119)	13.530(051)			
9	09 ^h 06 ^m 11 ^s .47	+19°23′57″47	14.049(117)	13.876(117)	13.336(045)			
10	09h06m18:41	+19°21′59″41	15.101(122)	14.207(142)	13.265(037)			
11	09 ^h 06 ^m 19 ^s .78	+19°21′11″78	15.624(116)	15.034(140)	14.300(037)	14.504(001)	13.989(004)	13.794(002)
12	09h06m22 s 84	+19°11′53″84	•••	•••	•••	17.049(003)	15.857(003)	15.206(003)
13	09h06m23 s 26	+19°27′45″26			11.120(005)			
14	09 ^h 06 ^m 25 ^s 39	+19°26′07″39	•••		•••	13.991(002)	13.547(003)	13.401(006)
15	09h06m28 s 27	+19°13′37″27	16.763(165)	16.324(098)	15.654(029)	15.818(004)	15.371(001)	15.213(001)
16	09 ^h 06 ^m 30 ^s .03	+19°19′50″03	•••	•••	•••	15.225(002)	14.559(003)	14.305(001)
17	09h06m32:41	+19°24′27″41	16.777(175)	16.659(117)	16.120(051)	16.227(003)	15.886(003)	15.760(005)
18	09 ^h 06 ^m 32 ^s .94	+19°17′54″94			12.832(012)			
19	09h06m34 s 32	+19°28′33″32	17.113(179)	16.248(103)	15.445(076)	15.663(001)	15.028(003)	14.773(003)
20	09h06m34s39	+19°21′52″39	15.806(063)	15.085(130)	14.215(028)	14.485(003)	13.851(004)	13.586(003)
21	09 ^h 06 ^m 34 ^s .74	+19°17′03″74	16.377(162)	15.671(110)	14.867(012)	15.112(002)	14.537(003)	14.315(003)
22	09h06m36s26	+19°29′46″26	14.544(113)	14.470(059)	13.949(071)	14.067(002)	13.711(005)	13.562(001)
23	09 ^h 06 ^m 43 ^s .46	+19°20′27″46	15.631(135)	15.244(108)	14.606(016)	14.765(005)	14.329(001)	14.183(001)
24	09 ^h 06 ^m 47 ^s 84	+19°25′33″84	15.742(079)	15.395(123)	14.760(056)	14.929(002)	14.502(002)	14.373(001)
25	09 ^h 06 ^m 47 ^s .92	+19°17′04″92	15.781(157)	15.318(070)	14.615(037)	14.813(001)	14.324(004)	14.141(002)
26	09 ^h 06 ^m 48 ^s 17	+19°13′56″17	14.501(06)	14.504(082)	13.928(016)	14.065(002)	13.715(005)	13.563(002)
27	09 ^h 06 ^m 52 ^s .18	+19°11′57″18	•••		16.723(122)	16.773(002)	16.411(003)	16.269(003)
28	09 ^h 06 ^m 54 ^s .07	+19°25′28″07	14.718(118)	14.603(097)	14.087(052)	14.204(002)	13.886(002)	13.766(008)
29	09 ^h 06 ^m 57 ^s .19	+19°18′13″19	15.555(151)	15.226(058)	14.562(022)	14.766(003)	14.322(003)	14.139(004)
30	09 ^h 06 ^m 58 ^s .25	+19°13′56″25	16.208(156)	16.047(051)	15.389(018)	15.557(001)	15.158(001)	15.009(004)
31	09h07m02:35	+19°17′23″35	14.296(083)	14.237(081)	13.623(007)	•••	•••	
32	09h07m02s62	+19°13′50″62	14.784(190)	14.403(054)	13.763(021)	13.936(001)	13.561(002)	13.432(007)
33	09h07m03 s 14	+19°15′58″14	16.385(141)	16.251(074)	15.469(014)	15.713(001)	15.173(002)	14.914(003)
34	09h07m03 s 82	+19°17′49″82	15.334(171)	14.481(074)	13.531(009)			
35	09 ^h 07 ^m 04 ^s .07	+19°26′20″07	`	`	12.647(039)	•••	•••	
36	09h07m16s62	+19°21′05″62	14.992(097)	14.878(071)	14.288(034)	14.441(003)	14.103(006)	13.984(008)
37	09h07m20 s 56	+19°21′50″56			`	15.357(002)	14.823(003)	14.621(005)
38	09h07m20 s 99	+19°23′49″99	16.216(221)	16.153(062)	15.558(018)	15.742(003)	15.394(003)	15.264(003)
39	$09^{h}07^{m}21\stackrel{s}{.}73$	+19°15′09″73	15.603(164)	15.536(026)	14.904(038)	15.106(001)	14.756(002)	14.639(002)

Notes. Uncertainties, in units of 0.001 mag, are 1σ .

Table 2 Photometric Standards in the SN 2018oh Field 2^a

Num.	α(J2000)	δ(J2000)	B (mag)	V (mag)	R (mag)	I (mag)
1	09h06m53 s 43	+19°18′22″43	16.553(032)	15.932(012)	15.567(015)	15.189(017)
2	09 ^h 06 ^m 36 ^s 12	$+19^{\circ}20'24''12$	19.686(033)	18.143(014)	17.237(015)	16.027(018)
3	09 ^h 06 ^m 54 ^s 98	+19°21′32″98	18.460(032)	17.350(012)	16.706(015)	16.151(018)
4	09 ^h 06 ^m 58 ^s 91	+19°20′26″91	18.413(032)	17.563(013)	17.070(016)	16.572(017)
5	09 ^h 06 ^m 30 ^s 32	+19°19′41″32	17.908(032)	17.173(012)	16.746(015)	16.309(017)
6	09 ^h 06 ^m 55 ^s 78	+19°15′40″78	17.785(032)	17.189(013)	16.837(015)	16.464(017)
7	09 ^h 06 ^m 55 ^s 71	+19°14′56″71	17.990(032)	17.170(012)	16.693(015)	16.204(017)
8	09 ^h 06 ^m 57 ^s 27	+19°23′16″27	17.654(032)	16.772(012)	16.261(015)	15.777(017)
9	09 ^h 07 ^m 07 ^s 05	+19°18′52″05	19.857(033)	18.292(014)	17.372(015)	16.333(018)
10	09 ^h 06 ^m 29 ^s 08	+19°22′45″08	19.367(033)	18.039(013)	17.265(016)	16.581(018)
11	09 ^h 06 ^m 36 ^s 11	$+19^{\circ}14'10''11$	19.765(032)	18.286(013)	17.418(015)	16.608(018)
12	09 ^h 07 ^m 09 ^s 67	+19°20′53″67	17.617(032)	16.848(012)	16.400(015)	15.973(017)
13	09 ^h 06 ^m 50 ^s 90	+19°13′22″90	18.832(033)	17.281(013)	16.370(015)	15.384(017)
14	$09^{h}07^{m}07\stackrel{s}{.}41$	$+19^{\circ}22'17\rlap.{''}41$	17.490(032)	16.434(012)	15.822(015)	15.235(017)

^a See Figure 1 for a finder chart of SN 2018oh and part of the comparison stars.

Notes. Uncertainties, in units of 0.001 mag, are 1σ . ^a Standards for Konkoly and Super-LOTIS observations.

Table 3
Ground-based Optical Photometry of SN 2018oh

Date	^a Epoch	U (mag)	B (mag)	V (mag)	R (mag)	I (mag)	g (mag)	r (mag)	i (mag)	Telescope
2018 Jan 26.6	-18.1	•••	•••				20.852(223)	•••	21.025(269)	PS1
2018 Jan 27.2	-17.5								19.039(009)	Decam
2018 Jan 27.3	-17.4	•••		•••		•••	•••	•••	18.957(008)	Decam
2018 Feb 03.1	-10.6	•••		•••		•••	15.500(010)	•••	•••	ASAS-SN
2018 Feb 03.3	-10.4	•••	•••	•••	•••	•••	•••	•••	15.671(004)	PS1
2018 Feb 04.3	-9.4	•••	•••	•••	•••	•••	•••	•••	15.446(004)	PS1
2018 Feb 04.5	-9.2	•••	•••	•••	•••	•••	•••	•••	15.389(003)	PS1
2018 Feb 05.1	-8.6	•••	14.982(025)	15.085(025)	•••	•••	•••	14.988(017)	15.305(025)	DEMONEXT
2018 Feb 05.2	-8.5	•••	14.940(026)	15.067(025)	•••	•••	•••	15.005(013)	15.262(024)	PONM
2018 Feb 05.2	-8.5	•••	•••	14.915(005)	14.832(006)	14.879(007)	•••	•••	•••	slotis
2018 Feb 05.4	-8.3	•••	•••	•••	•••	•••	•••	•••	15.264(010)	PS1
2018 Feb 05.8	-7.9	•••	14.818(031)	14.931(011)	•••	•••	14.707(005)	14.872(007)	15.089(009)	TNT
2018 Feb 05.9	-7.8	•••	•••	•••	•••		•••	14.883(006)	15.142(008)	LCO
2018 Feb 06.2	-7.5	•••	14.789(031)	14.879(013)	•••		•••	14.803(007)	15.101(006)	PONM
2018 Feb 06.2	-7.5	15.615(013)	14.762(012)	14.722(010)			14.711(010)	14.835(008)	15.149(009)	Swope
2018 Feb 06.2	-7.5			14.771(005)	14.709(006)	14.774(006)				slotis
2018 Feb 06.5	-7.2		14.758(027)	14.857(024)				14.789(016)	15.085(022)	DEMONEXT
2018 Feb 06.6	-7.1	14.285(027)	14.723(016)	14.799(014)			14.610(003)	14.798(003)	15.089(006)	LCO
2018 Feb 06.8	-6.9	14.213(062)	14.691(043)	14.818(015)	14.660(041)	14.662(029)				LJT
2018 Feb 06.8	-6.9		14.703(072)	14.724(027)	14.609(032)	14.637(035)				Konkoly
2018 Feb 07.2	-6.5		14.666(022)	14.783(016)				14.688(013)	14.972(019)	DEMONEXT
2018 Feb 07.2	-6.5	•••	14.681(034)	14.797(014)	•••	•••	•••	14.725(004)	15.010(007)	PONM
2018 Feb 07.2	-6.5	15.345(035)	14.600(012)	14.584(011)			14.531(010)	14.635(008)	14.985(009)	Swope
2018 Feb 07.2	-6.5		•••	14.668(006)	14.569(006)	14.650(006)	•••	•••	•••	slotis
2018 Feb 07.5	-6.2	14.173(026)	14.618(015)	14.697(014)		•••	14.494(002)	14.702(003)	14.987(006)	LCO
2018 Feb 07.7	-6.0		14.578(034)	14.701(020)			14.499(016)	14.713(018)	15.003(013)	TNT
2018 Feb 08.2	-5.5	15.291(032)	14.469(011)	14.471(010)	•••	•••	14.408(010)	14.557(008)	14.926(008)	Swope
2018 Feb 08.3	-5.4	•••	•••	•••	•••	•••	•••	14.609(009)	•••	Gemini
2018 Feb 08.4	-5.3		•••			•••	14.483(002)	14.613(002)		PS1
2018 Feb 08.5	-5.2	14.082(027)	14.529(015)	14.608(014)	•••		14.409(002)	14.614(003)	14.947(006)	LCO
2018 Feb 08.7	-5.0	•••	14.514(030)	14.622(010)	•••		14.421(003)	14.646(004)	14.963(006)	TNT
2018 Feb 09.1	-4.6	•••	14.521(025)	14.584(022)	•••	•••	•••	14.550(014)	14.940(026)	DEMONEXT
2018 Feb 09.2	-4.5	14.030(027)	14.509(015)	14.549(013)			14.382(001)	14.551(002)	14.904(003)	LCO
2018 Feb 09.2	-4.5	`	14.487(033)	14.591(012)	•••		`	14.540(004)	14.887(005)	PONM
2018 Feb 09.2	-4.5			14.450(004)	14.397(005)	14.555(006)			`	slotis
2018 Feb 09.3	-4.4			`	`		14.342(018)	14.556(019)		Gemini
2018 Feb 09.5	-4.2						14.359(002)	`	14.926(003)	PS1
2018 Feb 09.7	-4.0		14.411(030)	14.505(010)			14.327(003)	14.543(004)	`	TNT
2018 Feb 10.3	-3.4						14.266(008)	14.471(012)		Gemini
2018 Feb 10.5	-3.2						14.307(002)	14.476(002)		PS1
2018 Feb 10.5	-3.2		14.426(032)	14.520(032)				14.511(027)		DEMONEXT
2018 Feb 10.7	-3.0		14.375(031)	14.483(010)			14.287(005)	14.528(008)	14.949(010)	TNT
2018 Feb 10.9	-2.8	13.950(026)	14.323(015)	14.443(013)				14.493(010)		LCO
2018 Feb 10.9	-2.8							14.499(005)	14.936(007)	LCO
2018 Feb 11.2	-2.5		14.383(022)	14.476(022)				14.449(013)	14.905(024)	DEMONEXT
2018 Feb 11.2	-2.5		14.352(028)	14.438(010)				14.441(005)	14.884(007)	PONM
2018 Feb 11.3	-2.3	•••			•••		14.273(002)		14.961(003)	PS1
2010 100 11.0	2.5						11.273(002)		1 1.701(003)	101

Γ.

et

2

Table 3 (Continued)

Date	^a Epoch	U (mag)	B (mag)	V (mag)	R (mag)	I (mag)	g (mag)	r (mag)	i (mag)	Telescope
2018 Feb 23.3	+9.6						14.516(011)	14.727(033)		Gemini
018 Feb 23.4	+9.7	•••	14.803(025)	14.660(026)	•••	•••	•••	14.735(019)	15.535(032)	DEMONEX
018 Feb 23.7	+10.0	•••	14.774(031)	14.648(010)	•••	•••	14.556(003)	14.785(005)	•••	TNT
018 Feb 23.9	+10.2	•••	•••	•••	•••	•••	•••	14.829(009)	•••	T50
018 Feb 24.2	+10.5	14.793(027)	14.821(016)	14.726(015)	•••	•••	14.588(003)	14.820(007)	15.600(014)	LCO
018 Feb 24.3	+10.6	•••	14.854(024)	14.745(019)	•••	•••	•••	14.773(016)	15.583(029)	DEMONEX
018 Feb 24.6	+10.9	•••	14.887(032)	14.758(012)	•••	•••	14.646(004)	14.899(006)	15.643(010)	TNT
018 Feb 24.9	+11.2	•••	•••	14.649(126)	14.695(081)	15.102(039)	•••	•••	•••	Konkoly
018 Feb 25.2	+11.5	16.307(027)	14.866(012)	14.618(010)	•••	•••	14.652(009)	14.794(008)	15.686(009)	Swope
018 Feb 25.4	+11.7	14.885(032)	14.903(018)	14.769(017)	•••	•••	14.683(004)	14.947(008)	•••	LCO
018 Feb 25.8	+12.1	•••	•••	•••	•••	•••	•••	14.944(010)	15.684(017)	LCO
018 Feb 25.8	+12.1	•••	•••	14.809(076)	14.767(076)	15.171(035)	•••	•••	•••	Konkoly
018 Feb 26.1	+12.4	•••	15.034(024)	14.841(026)	•••	•••	•••	14.956(023)	15.765(028)	DEMONEX
018 Feb 26.2	+12.5	•••	15.028(031)	14.856(013)	•••	•••	•••	14.969(006)	15.757(011)	PONM
118 Feb 26.2	+12.5	16.489(036)	14.973(013)	14.711(011)			14.791(010)	14.940(009)	15.847(011)	Swope
018 Feb 26.6	+12.9		15.070(032)	14.860(011)			14.780(006)	15.055(007)	15.827(012)	TNT
18 Feb 27.2	+13.5		15.088(027)	14.872(026)				14.998(018)	15.742(030)	DEMONEX
018 Feb 27.2	+13.5	16.564(035)	15.061(016)	14.790(013)			14.879(012)	15.019(012)	15.913(016)	Swope
118 Feb 27.3	+13.6							14.992(013)		Gemini
018 Feb 27.7	+14.0		15.159(045)	14.963(022)			14.964(014)		15.932(056)	LJT
018 Mar 01.6	+15.9		15.323(038)	15.058(016)			15.025(012)	15.235(012)	15.941(020)	TNT
018 Mar 01.7	+16.0		15.312(043)	14.977(015)			15.062(013)	15.164(010)		LJT
018 Mar 02.1	+16.4	15.489(054)	15.451(028)	15.035(021)			15.067(013)	15.201(015)	15.902(029)	LCO
018 Mar 02.2	+16.5		15.425(034)	15.062(034)				15.157(028)	15.859(052)	DEMONEX
18 Mar 02.3	+16.6						15.033(011)	15.189(017)		Gemini
018 Mar 02.5	+16.8		15.590(089)							TNT
018 Mar 02.5	+16.8							15.210(012)	15.897(016)	LCO
018 Mar 03.2	+17.5		15.499(032)	15.113(031)				15.169(021)	15.874(031)	DEMONEX
018 Mar 03.2	+17.5						15.126(009)	15.202(018)		Gemini
018 Mar 03.9	+18.2							15.213(008)	15.850(013)	LCO
018 Mar 04.2	+18.5						15.195(009)	15.221(012)		Gemini
018 Mar 04.7	+19.0		15.706(036)	15.161(013)			15.228(008)	15.220(007)	15.827(013)	TNT
018 Mar 04.8	+19.1		15.708(068)	15.127(068)	15.025(025)	15.180(031)				Konkoly
018 Mar 05.2	+19.5		15.739(026)	15.137(043)				15.185(023)	15.764(039)	DEMONE
018 Mar 05.2	+19.5		15.782(033)	15.216(023)				15.244(010)	15.850(020)	PONM
018 Mar 05.2	+19.5						15.265(012)	15.232(020)		Gemini
018 Mar 05.5	+19.8		15.767(032)	15.196(011)			15.286(005)	15.219(007)	15.768(011)	TNT
018 Mar 05.9	+20.2							15.244(007)	15.817(012)	LCO
018 Mar 06.2	+20.5			•••	•••	•••	15.356(020)	15.249(022)		Gemini
018 Mar 06.2	+20.5			15.156(008)	15.108(009)	15.226(013)	•••	•••		slotis
18 Mar 06.4	+20.7		15.859(040)	15.180(039)				15.150(017)	15.726(031)	DEMONEX
018 Mar 07.2	+21.5		15.945(032)	15.233(041)				15.200(015)	15.736(031)	DEMONE
018 Mar 07.2	+21.5		15.970(029)	15.287(033)				15.255(012)	15.749(017)	PONM
018 Mar 07.2	+21.5		•••	•••			15.437(012)	15.253(019)	•••	Gemini
018 Mar 07.2	+21.5	•••	•••	15.200(006)	15.122(007)	15.253(008)	`		•••	slotis
018 Mar 07.8	+22.1	•••	15.915(069)	15.236(041)	14.967(075)	15.106(059)	•••	•••	•••	Konkoly
018 Mar 08.1	+22.4	17.766(037)	15.984(014)	15.228(010)		•••	15.577(010)	15.184(009)	15.761(010)	Swope
018 Mar 08.5	+22.8		16.113(032)	15.350(011)			15.566(004)	15.270(005)	15.780(007)	TNT

Table 3 (Continued)

Date	^a Epoch	U (mag)	B (mag)	V (mag)	R (mag)	I (mag)	g (mag)	r (mag)	i (mag)	Telescope
2018 Mar 08.8	+23.1							15.289(007)	15.753(010)	LCO
2018 Mar 08.9	+23.2	16.398(032)	16.143(019)	15.361(015)	•••	•••	15.637(005)	15.275(006)	15.725(019)	LCO
2018 Mar 08.9	+23.2	•••	16.083(100)	15.303(035)	15.041(033)	15.070(041)	•••	•••	•••	Konkoly
2018 Mar 09.1	+23.4	17.813(033)	16.144(014)	15.304(010)	•••	•••	15.680(010)	15.216(008)	15.770(009)	Swope
2018 Mar 09.2	+23.5	•••	16.126(031)	15.375(035)	•••	•••	•••	15.297(024)	15.694(043)	PONM
2018 Mar 09.2	+23.5	•••	•••	15.297(008)	15.156(009)	15.206(009)	•••	•••	•••	slotis
2018 Mar 09.6	+23.9	•••	16.192(032)	15.379(011)	•••	•••	15.629(006)	15.262(005)	15.701(008)	TNT
2018 Mar 10.2	+24.5	•••	16.165(036)	15.372(045)	•••	•••	•••	15.242(024)	15.620(026)	DEMONEX
2018 Mar 10.2	+24.5	•••	•••	15.338(016)	15.163(024)	15.206(023)	•••	•••	•••	slotis
2018 Mar 10.7	+25.0	•••	16.330(033)	15.444(011)	•••	•••	15.744(005)	15.311(005)	15.720(007)	TNT
2018 Mar 11.8	+26.1	•••	16.368(051)	15.473(016)	•••	•••	15.880(043)	15.287(010)	15.656(027)	LJT
2018 Mar 11.9	+26.2	16.765(045)	16.452(031)	•••	•••	•••	•••	•••	•••	LCO
2018 Mar 12.1	+26.4	•••	16.389(037)	15.504(055)	•••	•••	•••	15.282(020)	15.641(036)	DEMONEX
2018 Mar 12.2	+26.5	17.965(116)	16.406(016)	15.486(010)	•••	•••	15.949(010)	15.267(008)	15.734(009)	Swope
2018 Mar 12.6	+26.9	•••	16.349(045)	•••	•••	•••	•••	•••	•••	TNT
2018 Mar 12.7	+27.0	•••	16.452(046)	15.549(016)	•••	•••	15.964(011)	15.306(013)	15.647(029)	LJT
2018 Mar 12.8	+27.1	•••	•••	15.482(103)	15.155(064)	15.117(072)	•••	•••	•••	Konkoly
018 Mar 13.1	+27.4	18.174(058)	16.468(018)	15.477(011)		•••	15.965(011)	15.314(009)	15.641(010)	Swope
2018 Mar 13.2	+27.5	16.774(031)	16.472(018)	15.549(015)		•••	16.001(005)	15.365(005)	15.633(011)	LCO
2018 Mar 13.3	+27.6	•••	•••	15.481(009)	15.167(009)	15.075(009)	•••	•••	•••	slotis
018 Mar 13.4	+27.7	•••	•••	•••	•••	•••	•••	15.373(008)	15.616(014)	LCO
018 Mar 13.8	+28.2	•••	16.559(075)	15.529(023)	15.134(044)	14.995(036)	•••	•••	•••	Konkoly
2018 Mar 14.1	+28.4	18.259(055)	16.503(016)	15.561(011)	•••	•••	16.094(010)	15.335(008)	15.662(009)	Swope
018 Mar 14.2	+28.5	•••	•••	•••		•••	•••	•••		slotis
018 Mar 14.7	+29.0	•••	16.634(054)	15.666(026)	•••	•••	16.118(014)	15.357(020)	15.603(036)	LJT
018 Mar 14.8	+29.1	•••	16.612(051)	15.572(035)	15.161(045)	14.998(041)	•••	•••	•••	Konkoly
018 Mar 15.1	+29.4	18.335(059)	16.591(018)	15.600(011)		•••	16.159(010)	15.353(009)	15.645(009)	Swope
2018 Mar 15.6	+29.9	•••	16.650(034)	15.673(015)	•••	•••	16.092(009)	15.411(011)	15.635(017)	TNT
2018 Mar 16.1	+30.4	16.902(081)	16.724(018)	15.718(015)	•••	•••	16.245(005)	15.446(004)	15.621(007)	LCO
2018 Mar 16.1	+30.4	18.300(054)	16.650(016)	15.672(012)	•••	•••	16.214(011)	15.411(009)	15.621(009)	Swope
018 Mar 16.3	+30.6	•••	•••	15.601(013)	•••	•••	•••	•••	•••	slotis
2018 Mar 17.1	+31.4	18.478(064)	16.754(018)	15.768(012)	•••	•••	16.314(011)	15.437(009)	15.642(009)	Swope
2018 Mar 18.1	+32.4	18.632(107)	16.832(018)	15.847(012)	•••	•••	16.395(011)	15.502(008)	15.722(009)	Swope
2018 Mar 18.5	+32.8	•••	16.973(039)	15.876(015)	•••	•••	16.350(008)	15.599(013)	15.746(014)	TNT
2018 Mar 19.1	+33.4	•••	16.919(022)	15.878(015)	•••	•••	16.436(007)	15.605(006)	15.706(009)	LCO
2018 Mar 19.1	+33.4	18.615(148)	16.910(018)	•••	•••	•••	16.383(011)	15.534(008)	15.684(009)	Swope
2018 Mar 19.5	+33.8	•••	16.996(036)	15.941(014)		•••	16.385(012)	15.660(009)	15.804(016)	TNT
2018 Mar 20.1	+34.4	18.770(153)	16.984(018)	15.868(013)	•••	•••	16.535(011)	15.644(008)	•••	Swope
018 Mar 20.1	+34.4	•••	16.983(015)	15.866(010)	•••	•••	16.540(008)	15.649(005)	•••	Konkoly
018 Mar 21.0	+35.3	18.759(154)	17.012(018)	15.968(012)		•••	16.542(012)	15.656(009)	15.820(009)	Swope
018 Mar 21.3	+35.6	•••	•••	15.884(011)	15.539(012)	15.267(013)	•••	•••	•••	slotis
018 Mar 21.6	+35.9		17.114(039)	16.047(021)			16.496(018)	15.823(037)	15.926(069)	TNT
018 Mar 22.5	+36.8	•••	17.128(035)	16.068(013)	•••	•••	16.528(008)	15.831(008)	15.930(011)	TNT
018 Mar 23.1	+37.4	19.104(161)	17.196(020)	•••		•••				Swope
2018 Mar 23.6	+37.9		17.123(037)	16.137(018)		•••	16.583(013)	15.907(012)	16.017(016)	TNT
2018 Mar 24.1	+38.4	17.359(131)	17.170(133)	16.152(021)		•••	16.687(016)	15.882(011)	15.964(017)	LCO
2018 Mar 24.1	+38.4	19.102(168)	17.149(023)	16.117(013)			16.679(015)	15.870(010)	16.002(011)	Swope
2018 Mar 24.3	+38.6	•••	•••	•••	•••	15.414(306)	•••	•••		slotis

Li et al.

Table 3 (Continued)

Date	^a Epoch	U (mag)	B (mag)	V (mag)	R (mag)	I (mag)	g (mag)	r (mag)	i (mag)	Telescope
2018 Mar 24.7	+39.0						16.635(012)	15.957(010)	16.074(015)	TNT
2018 Mar 25.1	+39.4	•••	17.266(025)	16.205(015)	•••	•••	16.681(016)	15.948(011)	16.054(012)	Swope
2018 Mar 26.1	+40.4	19.129(157)	17.190(025)	16.239(015)	•••	•••	16.804(016)	16.011(011)	•••	Swope
2018 Mar 27.1	+41.4	•••	•••	•••	•••	•••	16.794(048)	15.984(034)	16.269(044)	Swope
2018 Mar 29.1	+43.4	17.372(135)	17.140(079)	16.272(051)			16.983(055)	16.159(041)	16.293(061)	LCO
2018 Mar 29.3	+43.6			16.276(021)	15.926(023)	15.721(022)				slotis
2018 Mar 31.3	+45.6	•••	•••	16.298(054)	16.037(073)	•••	•••	•••	•••	slotis
2018 Apr 01.7	+47.0		17.283(049)	16.459(019)			16.864(015)	16.257(015)	16.467(030)	LJT
2018 Apr 02.7	+48.0		17.296(063)	16.507(028)			16.936(020)	16.346(035)		LJT
2018 Apr 03.7	+49.0		17.404(047)	16.584(028)			16.912(017)	16.358(016)	16.544(032)	LJT
2018 Apr 04.1	+49.4	17.502(093)	•••	16.482(028)			16.912(026)	16.321(019)	16.541(028)	LCO
2018 Apr 04.2	+49.5		•••			•••	•••	•••	•••	slotis
2018 Apr 05.3	+50.6			16.445(016)	16.229(017)	16.021(018)		•••		slotis
2018 Apr 07.0	+52.3			`	`	`	16.885(002)		16.819(002)	Decam
2018 Apr 07.1	+52.4	19.186(284)	17.438(018)	16.593(013)			17.001(011)	16.451(010)	16.700(013)	Swope
2018 Apr 07.6	+52.9	`	`	`			`	16.396(221)	`	TNT
2018 Apr 08.6	+53.9						16.989(009)	16.553(010)	16.779(013)	TNT
2018 Apr 10.6	+55.9						16.992(008)	16.590(008)	16.820(010)	TNT
2018 Apr 12.0	+57.3	19.274(126)	17.541(014)	16.761(011)			17.159(011)	16.649(009)	16.937(012)	Swope
2018 Apr 12.7	+58.0		17.473(056)	16.831(101)	•••		17.043(048)	16.861(340)		LJT
2018 Apr 13.0	+58.3	19.290(240)	17.518(015)	16.759(012)			17.100(010)	16.653(009)	16.915(011)	Swope
2018 Apr 14.0	+59.3						16.978(002)		17.09(001)	Decam
2018 Apr 14.1	+59.4		17.570(015)	16.768(011)			17.149(010)	16.660(009)	16.978(011)	Swope
2018 Apr 15.1	+60.4	19.439(167)	17.537(015)	16.731(011)			17.108(010)	16.654(009)	16.926(011)	Swope
2018 Apr 15.5	+60.8	17.457(107)					17.133(011)	16.814(016)	17.080(017)	TNT
2018 Apr 16.0	+61.3	19.431(274)	17.678(016)	16.826(013)			17.513(031)	16.808(011)	17.097(016)	Swope
2018 Apr 16.6	+61.9	17.431(274)	17.076(010)	10.020(013)	•••	•••	17.143(015)	16.829(017)	17.106(015)	TNT
2018 Apr 17.0	+62.3	19.540(264)	17.495(028)	16.857(024)		•••	17.173(015)	16.696(016)	17.100(013)	Swope
2018 Apr 17.0	+63.3	17.540(204)	17.473(020)	10.037(024)		•••	17.173(013)	10.070(010)	17.243(002)	Decam
2018 Apr 17.6	+62.9			•••			17.133(017)	16.841(014)	17.073(018)	TNT
2018 Apr 17.0 2018 Apr 18.0	+63.3	19.553(246)	17.686(022)	16.933(016)			17.133(017)	16.823(015)	17.129(027)	Swope
2018 Apr 18.0 2018 Apr 20.5	+65.8	19.555(240)	17.536(069)	16.908(039)			17.297(013)	16.835(023)	17.129(027)	TNT
2018 Apr 20.5 2018 Apr 23.5	+63.8	•••	17.802(114)	10.908(039)		•••	17.119(040)	10.655(025)	17.040(043)	TNT
2018 Apr 24.0	+08.8 +70.3		17.802(114)	•••			17.229(002)		17.519(002)	Decam
		10.519(266)			•••		• •		` '	
2018 Apr 25.0	+70.3	19.518(266)	17.711(030)	17.030(019)			17.401(019)	17.022(015)	17.438(020)	Swope
2018 Apr 25.6	+70.9	•••	17.687(079)	17.054(041)	•••	•••	17.271(049)	17.070(042)	17.384(084)	TNT
2018 Apr 26.5	+71.8	•••		17.122(039)	•••	•••	17.271(040)	17.157(035)	17.430(063)	TNT
2018 Apr 28.5	+73.8	•••	17.674(150)	17.115(127)	•••	•••	17.336(108)	17.042(076)	17.268(114)	TNT
2018 May 02.0	+78.3	•••	•••		•••	•••			17.797(004)	Decam
2018 May 03.0	+79.3	•••		17.279(011)	•••	•••	17.477(011)	17.296(010)	17.703(016)	Swope
2018 May 04.5	+79.8		17.747(051)	17.282(039)	•••	•••	17.388(034)	17.331(029)	17.593(055)	TNT
2018 May 06.0	+81.3	19.837(241)	17.944(019)	17.326(016)	•••	•••	17.538(013)	17.382(013)	17.775(022)	Swope
2018 May 07.0	+83.3	•••	•••	•••	•••	•••	17.473(004)	•••	18.028(01)	Decam
2018 May 07.0	+83.3	•••	•••	•••	•••	•••	17.495(009)	•••	18.042(016)	Decam
2018 May 08.5	+83.8	•••	17.840(047)	17.384(042)	•••	•••	17.378(032)	17.483(066)	17.497(045)	TNT
2018 May 09.0	+84.3	•••	17.921(017)	17.332(014)	•••	•••	17.528(012)	17.448(015)	17.855(020)	Swope
2018 May 10.0	+86.3	19.585(252)	17.976(021)	17.398(016)			17.601(014)	17.525(019)	17.906(029)	Swope

Table 3 (Continued)

Date	^a Epoch	U (mag)	B (mag)	V (mag)	R (mag)	I (mag)	g (mag)	r (mag)	i (mag)	Telescope
2018 May 12.0	+88.3	19.440(359)	18.126(019)	17.545(017)	•••		17.699(013)	17.672(016)	18.018(027)	Swope
2018 May 17.0	+92.3	19.717(242)	18.111(016)	17.587(016)			17.721(011)	17.719(012)	18.176(022)	Swope
2018 May 18.6	+93.9		17.818(063)	17.550(056)						TNT
2018 May 19.0	+95.3		18.196(018)				17.827(014)			Swope
2018 May 20.0	+95.3	19.922(271)								Swope
2018 May 22.0	+98.3	20.149(316)	18.259(017)					17.911(013)	18.325(019)	Swope
2018 May 24.5	+99.8		17.938(174)	17.739(080)			17.714(060)	17.813(050)	18.131(108)	TNT
2018 May 25.0	+100.3						17.897(013)	17.962(013)	18.402(017)	Swope
2018 Jun 03.0	+110.3	19.680(241)	18.386(012)	17.921(010)			18.000(010)	18.260(018)	18.664(030)	Swope
2018 Jun 06.9	+113.3	20.098(306)	18.326(016)	18.011(015)				•••	•••	Swope
2018 Jun 07.0	+114.3	•••	•••	•••	•••	•••	18.014(010)	18.325(013)	18.677(025)	Swope

Notes. Uncertainties, in units of 0.001 mag, are 1σ . a Days relative to the *B*-band maximum on 2018 February 13.7 (JD 2,458,163.2).

Table 4
NIR Photometry of SN 2018oh

Date	^a Epoch	Y (mag)	J (mag)	H (mag)	K (mag)
2018 Feb 07.2	-6.5	15.571(051)	14.900(061)	15.196(111)	
2018 Feb 09.2	-4.5	15.442(049)	14.767(061)	15.215(121)	
2018 Feb 13.2	-0.5	15.778(047)	14.891(058)	15.208(100)	
2018 Feb 15.2	+1.5		15.032(055)	15.361(124)	
2018 Feb 16.2	+2.5	16.136(069)	15.106(067)	15.581(159)	
2018 Feb 17.2	+3.5		15.177(051)	15.347(070)	14.986(098)
2018 Feb 18.2	+4.5	16.344(079)	15.385(074)	15.715(156)	
2018 Feb 20.1	+6.4	16.627(108)	15.600(079)	15.488(114)	
2018 Feb 21.1	+7.4		15.603(052)	15.424(070)	15.234(098)
2018 Feb 23.2	+9.5	16.570(099)	16.026(100)	15.562(147)	
2018 Feb 25.1	+11.4	16.848(099)	16.607(112)	15.648(113)	
2018 Mar 03.2	+17.5	16.757(110)	16.854(163)	15.597(111)	
2018 Mar 05.1	+19.4	16.428(090)	16.883(194)	15.481(125)	
2018 Mar 08.1	+22.4	16.195(054)	16.462(134)	15.152(108)	
2018 Mar 09.1	+23.4		16.340(054)	15.164(071)	15.086(098)
2018 Mar 11.1	+25.4	15.856(041)	16.564(120)	15.175(098)	
2018 Mar 27.1	+41.4		16.380(057)	15.651(071)	15.757(100)
2018 Apr 08.0	+53.3	•••	17.258(059)	16.234(073)	16.238(102)

Notes. Uncertainties, in units of 0.001 mag, are 1σ .

Table 5
Swift Photometry of SN 2018oh

Date	^a Epoch	uvw2 (mag)	uvm2 (mag)	uvw1 (mag)	U (mag)	B (mag)	V (mag)
2018 Feb 05.4	-8.3	17.117(092)	18.04(146)	15.783(065)	14.228(045)	14.784(045)	14.804(061)
2018 Feb 06.8	-6.9	16.889(087)	17.981(116)	15.499(066)	13.955(044)	14.611(044)	14.688(063)
2018 Feb 07.5	-6.2	16.967(096)	17.98(135)	15.394(069)	13.912(044)	14.501(044)	14.675(067)
2018 Feb 10.4	-3.3	16.647(086)	17.73(116)	15.295(066)	13.714(043)	14.305(043)	14.247(054)
2018 Feb 17.0	+4.3	16.848(102)	17.708(132)	15.678(078)	14.147(047)	14.36(043)	14.251(056)
2018 Feb 19.4	+5.7	17.042(083)	17.805(1)	15.784(066)	14.291(046)	14.4(043)	14.4(057)
2018 Feb 22.7	+9.0	17.448(11)		16.279(076)	14.735(052)	14.66(044)	
2018 Feb 26.4	+12.7	17.586(098)	18.003(107)	16.498(077)	15.153(058)	14.911(046)	14.719(06)
2018 Mar 11.5	+25.8	18.374(117)	18.645(121)	17.595(099)	16.792(082)	16.332(063)	15.416(064)
2018 Mar 17.1	+31.4	18.351(125)	18.55(133)	17.861(119)	16.887(091)	16.719(07)	15.663(071)

Notes. Uncertainties, in units of 0.001 mag.

telescope (+YFOSC), the Lick 3 m Shane telescope (+KAST; Miller & Stone 1993), the SOAR 4.1 m telescope (+Goodman Spectrograph; Clemens et al. 2004), the Bok 2.3 m telescope, the HET 10 m telescope (+LRS2; Chonis et al. 2016), the MMT 6.5 m telescope, the Magellan 6.5 m telescope, the LCO 2.0 m telescopes (+FLOYDS), NTT (+EFOSC2; Buzzoni et al. 1984; Smartt et al. 2015), 83 and the APO 3.5 m telescope (+DIS). These spectra covered the phases from -8.5 to +83.8days after the maximum light. A log of the spectra is given in Table 6. All spectra were reduced using standard IRAF routines. Flux calibration of the spectra was performed using spectrophotometric standard stars observed at similar airmass on the same night as the SN. The spectra were corrected for atmospheric extinction using the extinction curves of local observatories; in most cases, the telluric lines were removed. All of the spectra presented in this paper will be made available via WISeREP (Yaron & Gal-Yam 2012).

2.3. K2 Photometry

We performed an independent photometric analysis on the Kepler long-cadence imaging data by involving the FITSH package (Pál 2012) and using our former experience with photometry of stars appearing in the vicinity of background galaxies (Molnár et al. 2015). Astrometric jitters were derived using a dozen nearby K2 stamps (see also Molnár et al. 2015; Pál et al. 2015), and the derived information is used afterward to perform frame registration at a subpixel level with an effective pixel scale of 1."0 pixel⁻¹. Pre-explosion images with small pointing errors were used to construct a background reference image prior to applying image subtraction. This construction is based on median averaging of the first 400 frames that were taken days before the explosion. During the subsequent differential aperture photometry, this mediancombined image was used as a template frame. In order to correct for various systematic effects, including instrumental artifacts and intrinsic background-level variations such as the rolling-band issue (see, e.g., Shappee et al. 2018b), we

^a Days relative to *B*-band maximum on 2018 February 13.7 (JD 2,458,163.2).

^a Days relative to *B*-band maximum on 2018 February 13.7 (JD 2,458,163.2).

⁸³ NTT spectra were reduced using the PESSTO pipeline (Smartt et al. 2015).

 Table 6

 Log of Spectroscopic Observations of SN 2018oh

UT Date	MJD	Epoch ^a	Range (Å)	Res. (Å)	Inst.
2018 Feb 05.2	58,154.2	-8.5	3640-10298	4.0	HET
2018 Feb 05.2	58,154.2	-8.5	3640-5220	2.0	SOAR
2018 Feb 05.5	58,154.5	-8.2	3300-10000	10.0	LCO
2018 Feb 06.2	58,155.2	-7.5	3380-10320	15.8	NTT
2018 Feb 06.7	58,155.7	-7.0	3498–9173	25.0	LJT
2018 Feb 07.2	58,156.2	-6.5	3190-10914	7.0	Shane
2018 Feb 07.3	58,156.3	-6.4	3640-7977	10.0	Bok
2018 Feb 07.3	58,156.3	-6.4	3685-9315	21.2	NTT
2018 Feb 08.2	58,157.2	-5.5	3640-10298	4.0	HET
2018 Feb 08.3	58,157.3	-5.4	3180-11252	7.0	Shane
2018 Feb 09.4	58,158.4	-4.3	3250-10000	10.0	LCO
2018 Feb 09.5	58,158.5	-4.2	3986-8834	15.0	XLT
2018 Feb 10.1	58,159.1	-3.6	3640-5220	2.8	SOAR
2018 Feb 10.3	58,159.3	-3.4	3799–9627	15.0	APO
2018 Feb 11.7	58,160.7	-2.0	3976–8830	15.0	XLT
2018 Feb 13.6	58,162.6	-0.1	3966–8816	15.0	XLT
2018 Feb 14.2	58,163.2	+0.5	3380–10320	15.8	NTT
2018 Feb 14.2	58,163.2	+0.5	3640–5220	2.8	SOAR
2018 Feb 14.6	58,163.6	+0.9	3249–10000	10.0	LCO
2018 Feb 15.5	58,164.5	+1.8	3976–8831	2.8	XLT
2018 Feb 16.3	58,165.3	+2.6	3380–7520	15.8	NTT
2018 Feb 16.6	58,165.6	+2.9	3975–8831	15.0	XLT
2018 Feb 18.7	58,167.7	+5.0	3958-8812	15.0	XLT
2018 Feb 19.2	58,168.2	+5.5	3380–7520	15.8	NTT
2018 Feb 19.5	58,168.5	+5.8	3959-8816	15.0	XLT
2018 Feb 20.5	58,169.5	+6.8	3400–10000	10.0	LCO
2018 Feb 21.7	58,170.7	+8.0	3981–8835	15.0	XLT
2018 Feb 22.2	58,171.2	+8.5	3380–7520	15.8	NTT
2018 Feb 22.2 2018 Feb 27.7	58,176.7	+6.5 +14.0	3501–9166	25.0	LJT
2018 Heb 27.7 2018 Mar 01.7	58,178.7	+14.0 $+16.0$	3501–9100	25.0	LJT
2018 Mar 06.2	58,183.2	+10.0 +20.5	5601–6905	1.5	MMT
2018 Mar 07.4	58,184.4	+20.3 +21.7	3250–10000	10.0	LCO
2018 Mar 08.2	58,185.2	+21.7 +22.5	3380–10320	15.8	NTT
					XLT
2018 Mar 09.6	58,186.6	+23.9	3961–8815	15.0	
2018 Mar 11.6	58,188.6	+25.9	3899–9299	10.0	LCO LJT
2018 Mar 12.7	58,189.7	+27.0	3497–9166	25.0	
2018 Mar 14.2	58,191.2	+28.5	3752–9208	2.0	Magellan
2018 Mar 15.6	58,192.6	+29.9	3600–9999	10.0	LCO
2018 Mar 19.4	58,196.4	+33.7	3249–9999	10.0	LCO
2018 Mar 19.7	58,196.7	+34.0	3503–9165	25.0	LJT
2018 Mar 22.1	58,199.1	+36.4	3500–9040	6.0	SOAR
2018 Mar 23.5	58,200.5	+37.8	3965–8822	15.0	XLT
2018 Mar 23.7	58,200.7	+38.0	3492–9160	25.0	LJT
2018 Mar 24.1	58,201.1	+38.4	3380–10320	15.8	NTT
2018 Mar 25.0	58,202.0	+39.3	3966–8822	15.0	XLT
2018 Apr 06.1	58,214.1	+51.4	3715–8061	10.0	Bok
2018 Apr 06.1	58,214.1	+51.4	3380–10320	15.8	NTT
2018 Apr 07.5	58,215.5	+52.8	3966–8822	15.0	XLT
2018 Apr 21.0	58,229.0	+66.3	3560–8948	6.0	SOAR
2018 Apr 21.0	58,229.0	+66.3	3380–10320	15.8	NTT
2018 Apr 25.0	58,233.0	+70.3	3180–11252	7.0	Shane
2018 Apr 27.6	58,235.6	+72.9	3966–8822	15.0	XLT
2018 Apr 27.6	58,235.6	+72.9	3492–9160	25.0	LJT
2018 May 02.6	58,240.6	+77.9	3966-8822	15.0	XLT
2018 May 08.0	58,246.0	+83.3	3180-11252	7.0	Shane
2018 May 08.5	58,246.5	+83.8	3966-8822	15.0	XLT

Note.

performed an additional background estimation on the subtracted images. Finally, the background-subtracted instrumental light curve was calibrated to physical units by comparing with synthetic photometry computed with the

SNCOSMO code (Barbary et al. 2016). This was obtained using the *Kepler* bandpass on the extended SALT 2 templates with the light-curve parameters derived in Section 3.3. The resulting *K*2 light curve agreed well within the error bars of those

^a Days relative to *B*-band maximum on 2018 February 13.7 (JD 2,458,163.2).

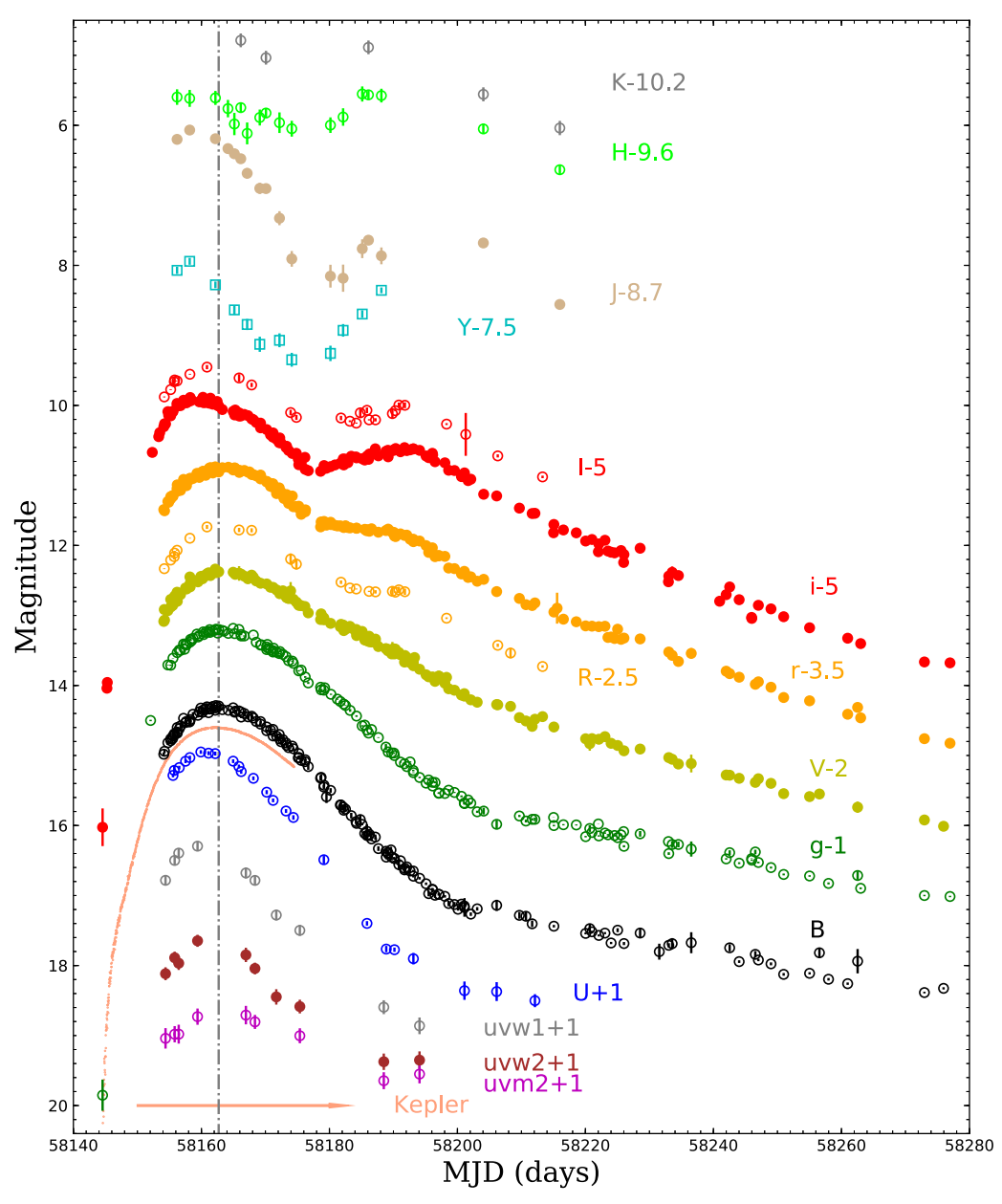


Figure 3. The NIR, optical, and UV light curves of SN 2018oh. The vertical dot-dashed line marks the date for the *B*-band maximum light, $t_{\rm Bmax} = {\rm MJD}$ 58,162.7 \pm 0.3 (2018 February 13.7).

presented in Dimitriadis et al. (2018) and Shappee et al. (2018b).

3. Light Curves

3.1. UV/Optical Light Curves

Figures 3 and 5 show the optical, UV, and NIR light curves of SN 2018oh. The optical light curves have a nearly daily cadence from $\sim \! 10$ days before to about 100 days after the maximum light of the B band. The earliest detections of this SN can actually be traced back to the PS1 images taken on 2018 January 26.56, corresponding to -18.1 days relative to the peak, when the g- and i-band magnitudes were 20.85 ± 0.22 and 21.03 ± 0.27 , respectively. We take MJD $58,144.37 \pm 0.04$ as the explosion time, which is the average of the values adopted in Dimitriadis et al. (2018) and Shappee et al. (2018b). Like other normal SNe Ia, the light curves of SN 2018oh show

prominent shoulders in the R/r bands and secondary peaks in the I/i and NIR YJHK bands, and they reached their peaks slightly earlier in the I/i, YJHK, and UV bands relative to the B band.

Using a polynomial fit to the observed light curves, we find that SN 2018oh reached a peak magnitude of $B_{\rm max}=14.31\pm0.03$ mag and $V_{\rm max}=14.37\pm0.03$ mag on MJD 58,162.7 \pm 0.3 (2018 February 13.7) and 58,163.7 \pm 0.3, respectively. The post-maximum decline rate in the B band, $\Delta m_{15}(B)$, is 0.96 \pm 0.03 mag. The results for all of the UBVRIgriYJHK-band light curves are reported in Table 7. Results from standard light-curve models like MLCS2k2 (Jha et al. 2007), SALT 2 (Guy et al. 2010), and SNooPy2 (Burns et al. 2011) will be used to derive the distance to the SN and discussed in Section 3.3.

In Figure 4, we compare the light curves of SN 2018oh with other well-observed SNe Ia that have similar $\Delta m_{15}(B)$. The

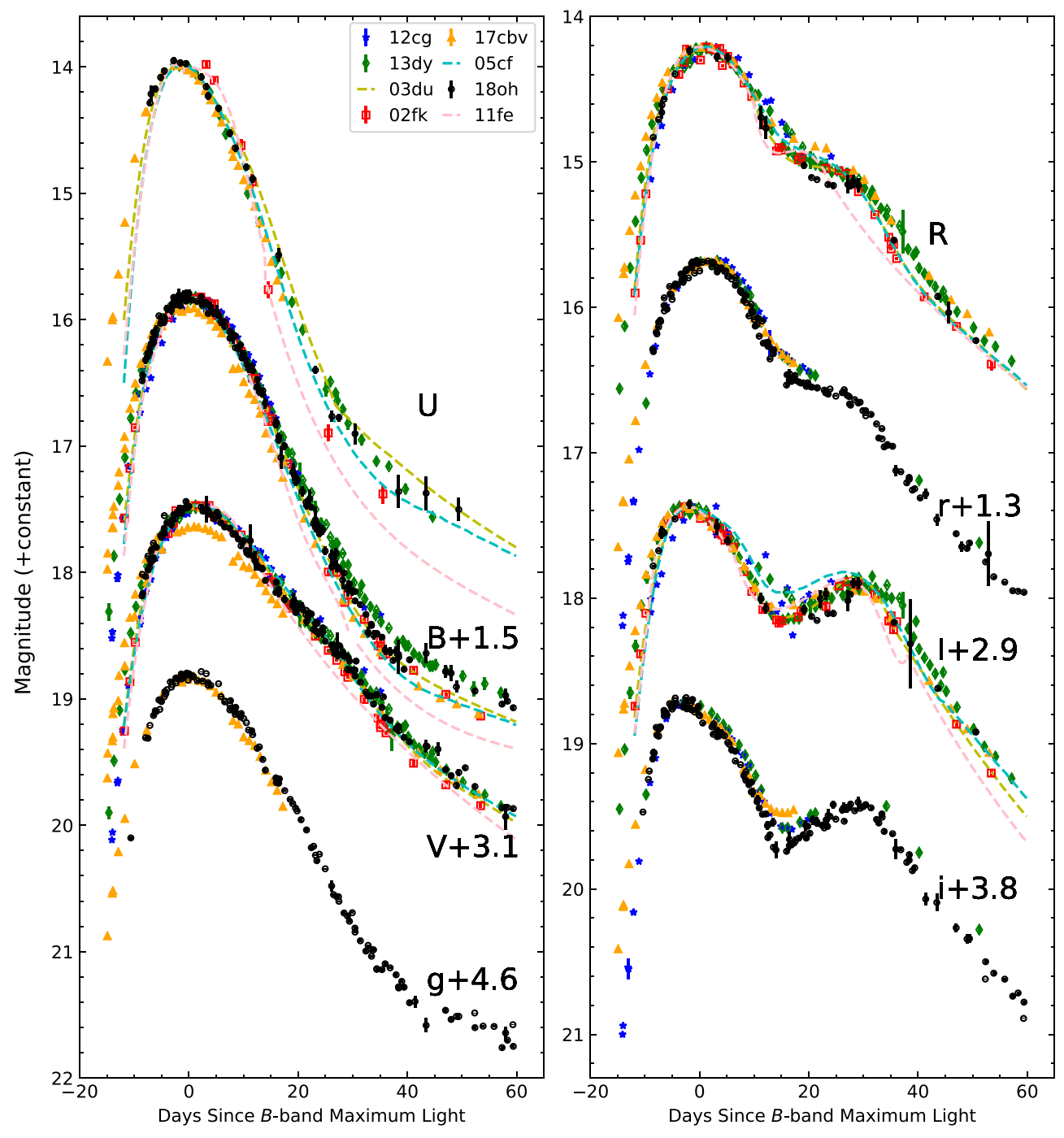


Figure 4. Comparison of the optical light curves of SN 2018oh to other well-observed SNe Ia with similar decline rates. The light curves of the comparison SNe Ia are normalized to match the peak magnitudes of SN 2018oh.

comparison sample includes SN 2002fk ($\Delta m_{15}(B) = 1.02 \pm 0.04$ mag; Cartier et al. 2014), SN 2003du ($\Delta m_{15}(B) = 1.02 \pm 0.03$ mag; Stanishev et al. 2007), SN 2005cf ($\Delta m_{15}(B) = 1.07 \pm 0.03$ mag; Wang et al. 2009a), SN 2011fe ($\Delta m_{15}(B) = 1.10 \pm 0.02$ mag; Munari et al. 2013), SN 2012cg ($\Delta m_{15}(B) = 1.04 \pm 0.03$; Munari et al. 2013), SN 2013dy ($\Delta m_{15}(B) = 0.92 \pm 0.03$; Pan et al. 2015), and SN 2017cbv ($\Delta m_{15}(B) = 1.06 \pm 0.03$; Hosseinzadeh et al. 2017). The morphology of the light curves of SN 2018oh closely resembles to that of SN 2003du and SN 2013dy, with $\Delta m_{15}(B)$ lying between these two comparison SNe Ia.

Figure 6 shows that the optical color evolution of SN 2018oh is similar to that of the comparison sample. At $t \gtrsim -10$ days, both the U-B and B-V colors become progressively redder until $t \sim 4$ –5 weeks after the maximum light. The V-I color initially becomes bluer until $t \sim +10$ days; it then turns redder, reaching the reddest color at $t \sim +35$ days. After $t \sim +35$ days, both the B-V and V-I curve colors become bluer. In the very early phases (at $t \lesssim -14$ days), however, the color evolution of the SN is scattered. For instance, SN 2011fe evolved from very red colors toward blue ones, while SN 2017cbv (and perhaps SN 2012cg) shows the opposite trend.

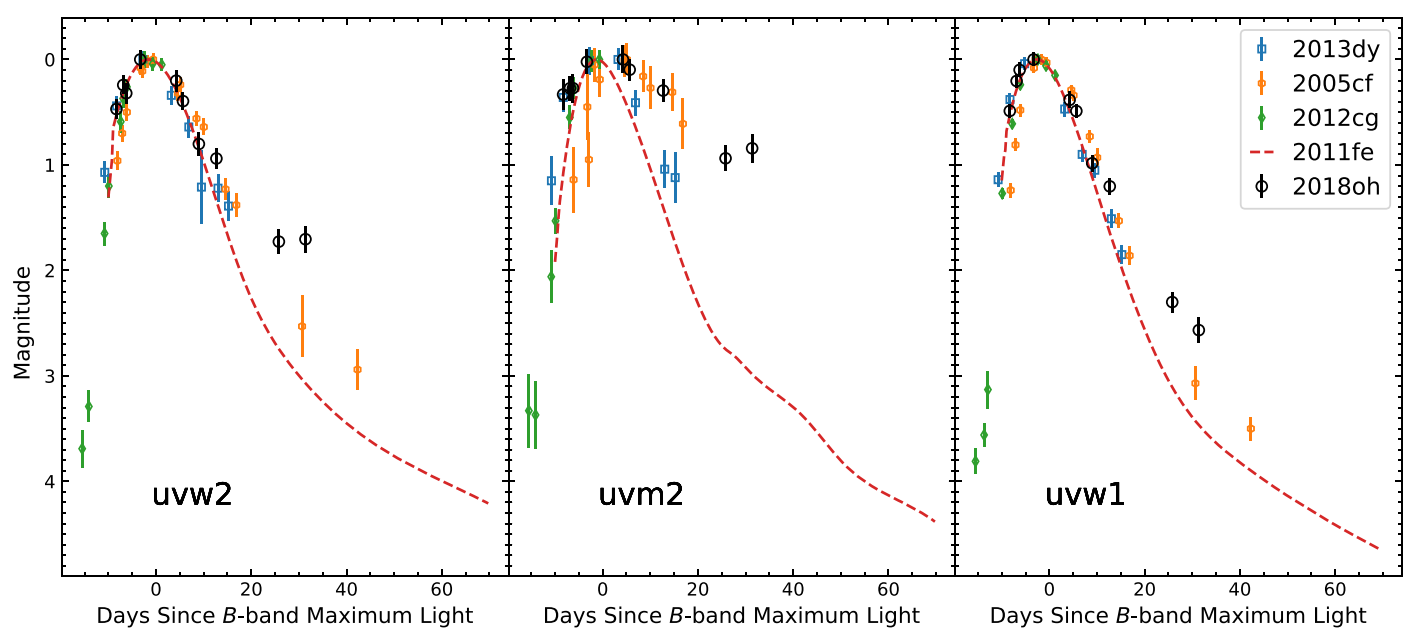


Figure 5. Comparison of the *UV* light curves of SN 2018oh with other well-observed SNe Ia with similar decline rates. The magnitudes and phases of all SNe Ia are normalized to the corresponding values at maximum light.

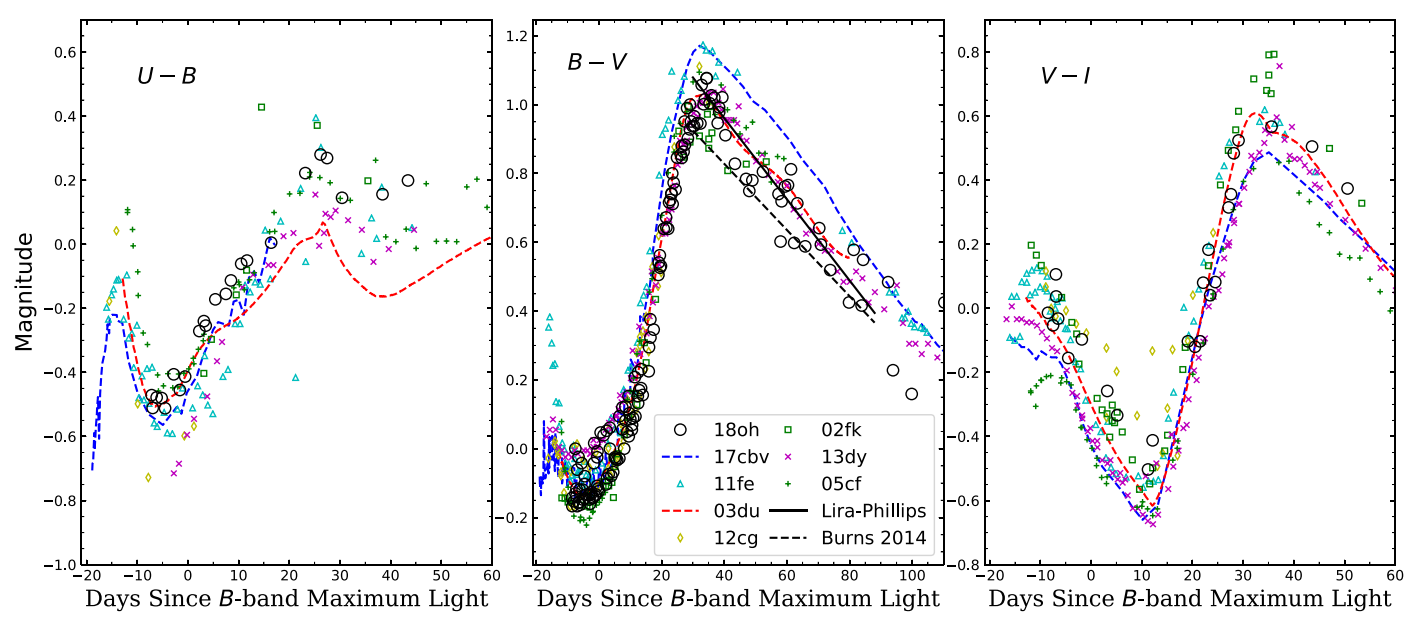


Figure 6. The U-B, B-V, and V-I color curves of SN 2018oh compared with those of SNe 2002fk, 2003du, 2005cf, 2011fe, 2012cg, 2013dy, and 2017cbv. All of the comparison SNe have been dereddened. The dash-dotted line in the B-V panel shows the unreddened Lira–Phillips loci and updated version from Burns et al. (2014). The data sources are cited in the text.

Bluer colors seen in the early phase of some SNe Ia have been interpreted as a result of interactions between the ejecta and a companion star, supporting the SD progenitor scenario (Brown et al. 2012; Marion et al. 2016; Hosseinzadeh et al. 2017). It is not clear whether SN 2018oh had such blue colors due to the lack of color information at very early times. It shows relatively bluer B-V colors than the comparison SNe Ia, but it is redder in the U-B and V-I colors. The slightly redder U-B color seen in SN 2018oh could be related to stronger Ca II H&K and iron-group element (IGE) absorption at shorter wavelengths. We do not show the gri-band color evolution due to the lack of data in these bands for most of our comparison sample, but SN 2018oh shows a similar evolutionary trend to SN 2017cbv in its g-r and r-i colors at comparable

Table 7
Photometry Parameters of SN 2018oh

Band	$\lambda_{\mathrm{eff}} (\mathring{\mathrm{A}})$	$t_{\rm max}~({ m MJD})$	$m_{\rm peak}~({\rm mag})$	Δm 15 (mag)
uvw2	2030	$58,161.2 \pm 0.2$	16.67 ± 0.07	1.08 ± 0.49
uvm2	2228	$58,164.1 \pm 0.8$	17.71 ± 0.05	0.49 ± 0.46
uvw1	2589	$58,160.5 \pm 0.1$	15.31 ± 0.07	1.32 ± 0.45
U	3663	$58,161.1 \pm 0.1$	13.98 ± 0.01	1.19 ± 0.12
B	4360	$58,162.9 \pm 0.1$	14.32 ± 0.01	0.96 ± 0.02
V	5446	$58,164.1 \pm 0.1$	14.37 ± 0.01	0.63 ± 0.06
R	6414	$58,163.7 \pm 0.2$	14.21 ± 0.01	0.69 ± 0.09
I	7979	$58,161.7 \pm 0.2$	14.47 ± 0.02	0.64 ± 0.15
g	4640	$58,163.6 \pm 0.2$	14.22 ± 0.01	0.82 ± 0.07
r	6122	$58,163.3 \pm 0.1$	14.38 ± 0.01	0.70 ± 0.08
i	7440	$58,160.4 \pm 0.1$	14.91 ± 0.01	0.85 ± 0.07

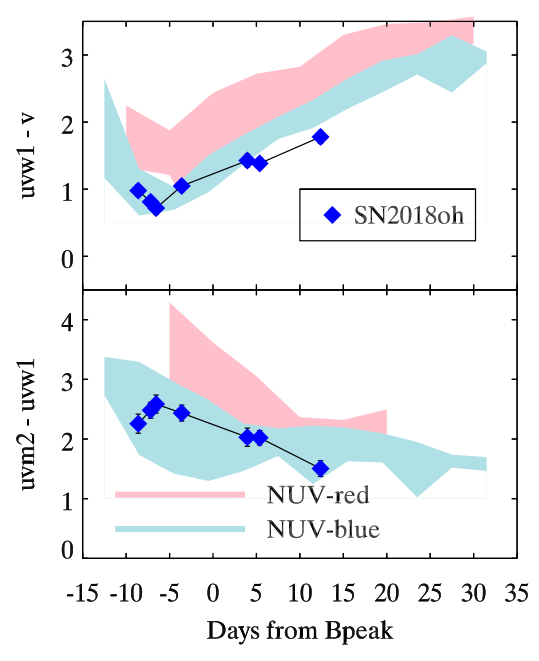


Figure 7. The uvm2–uvw1 and uvw1– ν colors of SN 2018oh compared to a group of NUV-blue and NUV-red SNe (see, e.g., Milne et al. 2013).

 Table 8

 Best-fit Parameters from the Applied Light-curve Fitters

Parameter	SALT 2.4	SNooPy2	MLCS2k2
$T_{\text{max}}(B) \text{ (MJD)}$	58,163.34 (0.02)	58,162.67 (0.05)	58,162.70 (0.02)
x_0	0.038 (0.001)		
x_1	0.879 (0.012)		
C	-0.09(0.010)		
$E(B-V)_{\rm host}$		0.00 (0.01)	0.00 (0.01)
Δm_{15}		0.865 (0.060)	
Δ_{MLCS}			-0.100(0.08)
μ_0 (mag)	33.614 (0.05)	33.62 (0.22)	33.57 (0.06)

phases. Dimitriadis et al. (2018) showed the very early g-i color and concluded that before $t\sim-10$ days, SN 2018oh looks bluer than SN 2011fe and is similar to SN 2017cbv.

Milne et al. (2013) found that the near-UV (NUV) colors of SNe Ia can be divided into NUV-blue and NUV-red groups. We compare SN 2018oh with these two groups in Figure 7. As shown in Figure 7, SN 2018oh belongs to the NUV-blue group, consistent with the finding of Milne et al. (2013) that the detection of C II (see Section 4.3) is common among the NUV-blue SNe Ia and rare among NUV-red SNe Ia. SN 2018oh has a normal velocity and low velocity gradient of Si II λ 6355 absorption features, which also follows the same trend as the NUV-blue group (Milne et al. 2013). These groupings (or the positions of SNe along a continuum of NUV colors) are affected by reddening but still present for SNe Ia with low reddening (Brown et al. 2017).

We also compare the color evolution of SN 2018oh with SN 2005cf (Wang et al. 2009a), SN 2017cbv (Wang et al., in preparation), and SN 2011fe (Matheson et al. 2012) in the NIR bands, as shown in Figure 8. SN 2017cbv is bluer in both NIR colors before maximum, and SN 2018oh is bluer around maximum in V-H. The last two V-J points of SN 2018oh are significantly redder than the others.

3.2. Reddening Correction

The Galactic extinction toward SN 2018oh is estimated as A_V (Gal) = 0.124 mag (Schlafly & Finkbeiner 2011), corresponding to $E(B - V)_G = 0.040$ mag for a Cardelli et al. (1989) extinction law with $R_V = 3.1$. As SN 2018oh appears close to the projected center of its host galaxy, it is necessary to examine the reddening due to the host galaxy. After corrections for the Galactic extinction, the B-V colors at peak and t=+35 days are found to be -0.10 ± 0.03 and 1.02 ± 0.03 0.04 mag, respectively, which are consistent with typical values of unreddened SNe Ia with comparable $\Delta m_{15}(B)$ (Phillips et al. 1999; Jha et al. 2007; Wang et al. 2009a; Burns et al. 2014). Similarly, if we fit the B-V evolution over the phases from t = 30 to 90 days past the peak (Lira-Phillips relation; Phillips et al. 1999) using Burns et al. (2014), we derive a reddening of -0.06 ± 0.04 and 0.06 ± 0.04 mag, respectively. Finally, we did not find any evidence for Na I D (λ 5890) absorption due to the host galaxy. We thus conclude that there is no significant host galaxy extinction, even though the SN is located near the projected center of its host galaxy.

3.3. Light-curve Fitting

We adopt SALT 2.4 (Betoule et al. 2014) as our primary light-curve fitter because it has the most flexibility in fitting multiband light curves taken in different photometric systems, and the most recent calibrations include the dependence on the host galaxy stellar mass. We also use SNooPy2 (Burns et al. 2011) and MLCS2k2 (Jha et al. 2007) to verify the distances (see also Vinko et al. 2018).

The final, best-fit results are shown in Figures 9 and 10. Table 8 summarizes the light-curve parameters and the inferred distance moduli. The distance moduli from the SALT 2.4 best-fit parameters are derived using the calibration by Betoule et al. (2014). The stellar mass of the host of SN 2018oh (UGC 04780) is $\log_{10}(M_{\rm stellar}/M_{\odot}) \sim 6.9$ (see Section 5.1) and is taken into account as a "mass-step" correction of \sim 0.06 mag in the Betoule et al. (2014) calibration. The distance moduli listed in the last row of Table 8 are brought to a common Hubble constant of $H_0 = 73 \, \mathrm{km \, s^{-1} \, Mpc^{-1}}$ (Riess et al. 2016, 2018).

It is readily seen that the distances from the three independent light-curve fitting codes are in excellent agreement. We adopt the SALT 2.4 distance modulus of $\mu_0=33.61\pm0.05$ mag, corresponding to 52.7 ± 1.2 Mpc, as the final result in our following analysis.

4. Optical Spectra

Figure 11 displays the spectral evolution of SN 2018oh. The earlier spectra are dominated by absorption features of Si, Ca, S, and Fe. Near maximum light, the spectral evolution follows that of a normal SN Ia, with the distinctive "W"-shaped S II lines near 5400 Å, the blended lines of Fe II and Si II near 4500 Å, and the prominent Ca II absorption feature near 8300 Å. A weak absorption feature that can be attributed to C II λ 6580 is seen on the red edge of the Si II λ 6355 absorption feature for a long time (see discussion in Section 4.3). We discuss the spectral evolution of SN 2018oh in detail in the following subsections.

4.1. Temporal Evolution of the Spectra

In Figure 12, we compare the spectra of SN 2018oh with those of SNe Ia having similar decline rates at several epochs. The

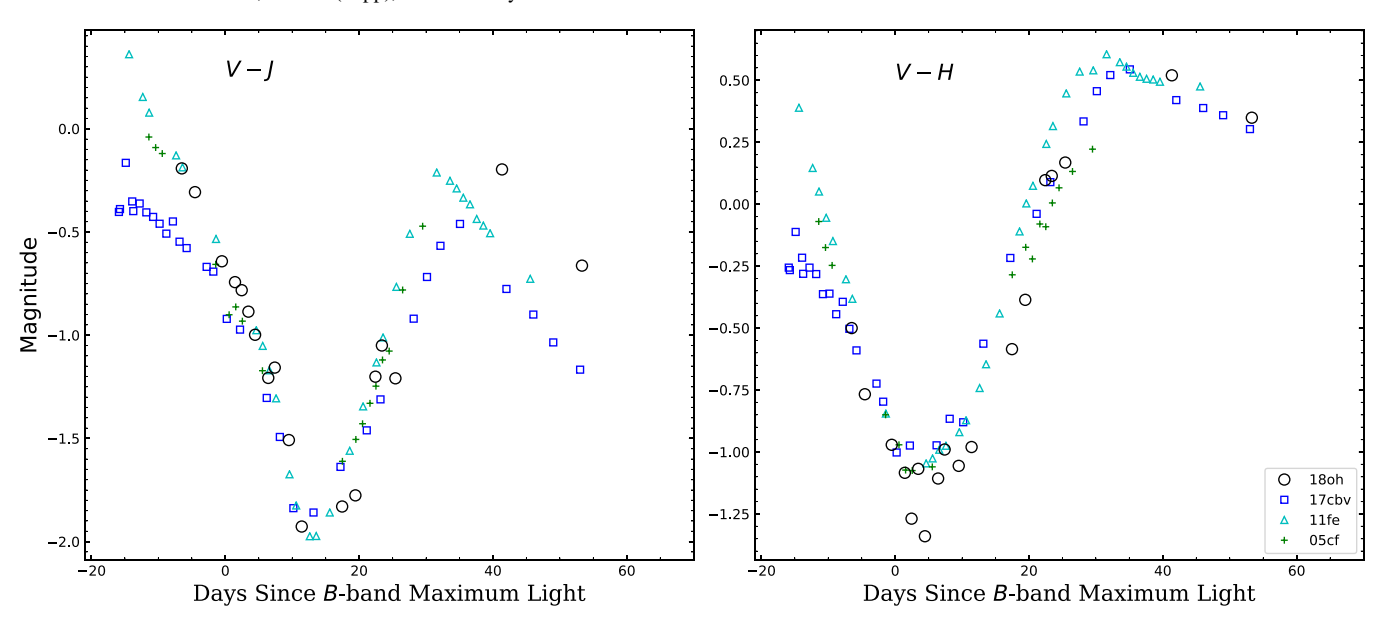


Figure 8. The V-J and V-H color curves of SN 2018oh compared with those of SNe 2005cf, 2011fe, and 2017cbv. All of the SNe have been dereddened. The data sources are cited in the text.

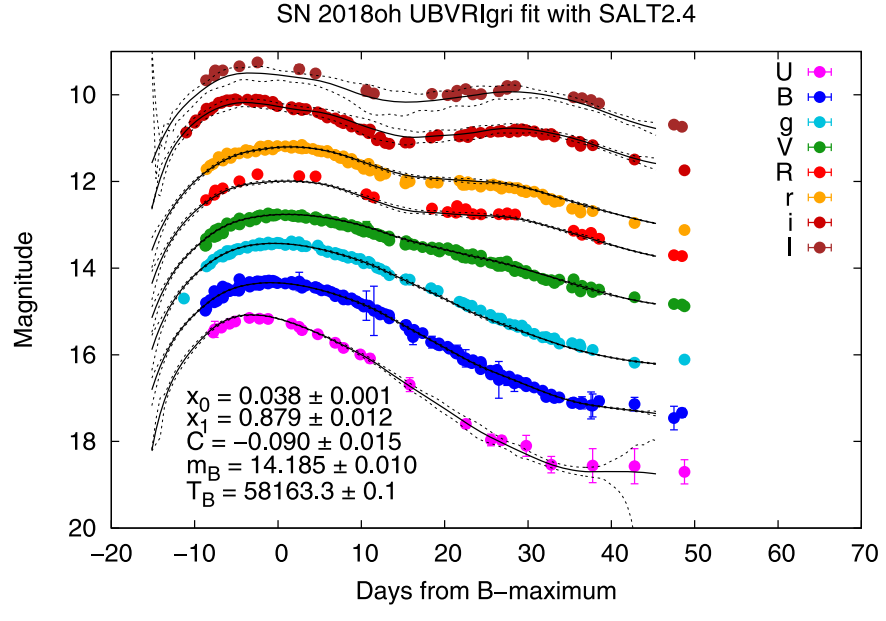


Figure 9. Best-fit light-curve model from SALT 2.4. The light curves are shifted vertically for better visibility. The dashed lines represent the 1σ uncertainty of the light-curve templates.

earliest spectrum of SN 2018oh was taken at $t \sim -9.0$ days. Figure 12(a) compares this spectrum with other SNe Ia at similar phases. The prominent features include Ca II H&K/Si II λ 3858, the "W"-shaped S II lines, and Si II $\lambda 6355$ absorption features. Other features include Si II $\lambda 4130$, Fe II $\lambda 4404/\text{Mg}$ II $\lambda 4481$, Si II $\lambda 5051/\text{Fe}$ II $\lambda 5018$, and Fe III $\lambda 5129$. The minor absorption neighboring with Si II $\lambda 4130$ can be due to C II $\lambda 4267$. The absorption feature appearing on the right edge of the S II doublet, also visible in all of our comparison SNe Ia, is not presently identified. For SN 2018oh, the absorption due to Si II $\lambda\lambda$ 5958, 5979 seems to be weaker than that in SN 2011fe, SN 2003du, and SN 2005cf but is comparable to that in SN 2012cg and SN 2013dy. The strength of Fe III $\lambda 5129$ for SN 2018oh follows the same manner as Si II $\lambda\lambda$ 5958, 5979 relative to the comparison SNe Ia. A smaller line-strength ratio of Si II $\lambda\lambda$ 5958, 5979 to Si II $\lambda 6355$, known as R(Si II), indicates a relatively higher

photospheric temperature for SN 2018oh (Nugent et al. 1995). Recently, Stritzinger et al. (2018) found that SNe Ia exhibiting blue colors in the very early phase all belong to the shallow silicon (SS) subtype among Branch's classification scheme (Branch et al. 2006), i.e., SNe 2012cg, 2013dy, and 2017cbv. The pseudoequivalent widths (pEWs) of Si II $\lambda\lambda$ 5972, 6355 measured near the maximum light for SN 2018oh are 79 and 8 Å, respectively, suggesting that it can also be put into the SS subgroup or at least locates near the boundary between the SS and core-normal subgroups. At about 1 week before the maximum light, absorption features of C II 7234 and O I 7774 are not prominent in SN 2018oh and the comparison SNe Ia except for SN 2011fe, which had more unburned oxygen in the ejecta. A detached HV feature (HVF) can be clearly identified in the Ca II NIR triplet absorption features, and its relative strength is similar to that seen in SN 2013dy but weaker than that in SN 2005cf and SN 2012cg.

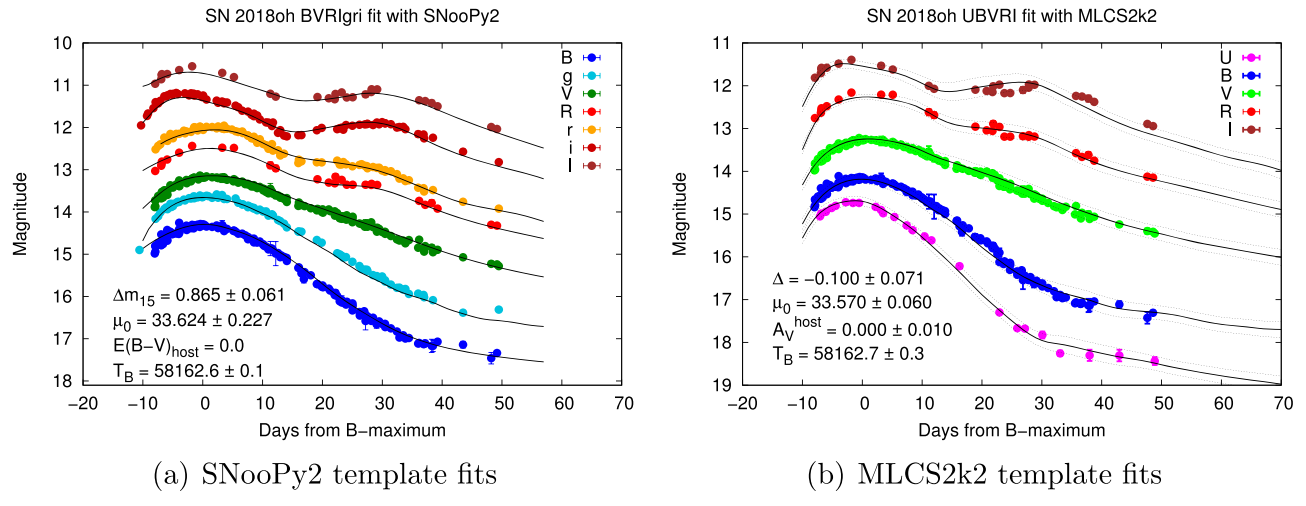


Figure 10. Best-fit light-curve models from SNooPy2 and MLCS2k2. The light curves are shifted vertically for better display. The dashed lines represent the 1σ uncertainty of the light-curve templates.

A weak HVF of Si II 6355 is also visible in SN 2018oh and the comparison SNe Ia but not in SN 2011fe.

Figure 12(b) compares the near-maximum spectra. At this phase, the spectrum of SN 2018oh has evolved while maintaining most of its characteristics from the earlier epochs. The weak features (e.g., Si II λ 4130, Si III λ 4560, and the S II "W") become more prominent with time, as also seen in the comparison SNe Ia. The C II absorption features are still clearly visible near 6300 and 7000 Å in the spectrum of SN 2018oh around maximum light, while they are barely detectable in other SNe Ia at this phase except for SN 2002fk. The O I λ 7774 line gains in strength for all SNe, and the absorption at \sim 7300 Å might be due to an O I HVF. By $t \sim 0$ days, the relative strength of the two absorption components of the Ca II NIR triplet evolves rapidly, with the blue component (HVF) becoming weak and the red (photospheric) component becoming gradually strong and dominant. At this phase, the R(Si II) parameter is measured as 0.15 \pm 0.04, which suggests a high photospheric temperature and luminosity. This is consistent with a smaller decline rate that is characterized by an intrinsically more luminous SN Ia.

At about 1 week after maximum light, most of the spectral features show no obvious evolution relative to those seen near the maximum light, as seen in Figure 12(c). We note that the absorption near 5700 Å becomes stronger in all of our sample, which is likely due to the contamination of Si II λ 5972 by Na I that gradually develops after maximum light. For SN 2018oh, the most interesting spectral evolution is that the C II 6580 Å absorption gains in strength during this phase, which has never been observed in other SNe Ia. Moreover, the C II 6580 Å absorption can even be detected in the $t \sim 20.5$ days spectrum, which is unusually late for a normal SN Ia. The spectral comparison at $t \approx 1$ month is shown in Figure 12(d), where one can see that SN 2018oh exhibits spectral features very similar to other SNe Ia in comparison. With the receding of the photosphere, the Fe II features are well developed and become dominant in the wavelength range from 4700 to 5000 Å. By a few weeks after B maximum, the region of Si II λ 5972 is dominated by Na I absorption, and the Si II $\lambda 6355$ absorption trough is affected by Fe II $\lambda\lambda6238$, 6248 and Fe II $\lambda\lambda6456$, 6518. Although the Ca II NIR triplet shows the most diverse features in the earlier phases, they develop into an absorption

profile that is quite smooth and similar to the comparison sample at this time.

Figure 13 presents the detailed evolution of "W-shaped" S II, Si II 5972, Si II 6355, C II 6580, and the Ca II NIR triplet for SN 2018oh. This evolution is shown in a velocity space. Panel (a) shows the line profile of S II 5460, 5640 and Si II 5972. One notable feature is the asymmetric absorption trough near 5500 Å, where there is a notch on the red wing. This notch feature is likely a detached HV component of Si II 5972, since it has a velocity of \sim 19,000 km s⁻¹, comparable to that of the HVF of Si II 6355, and it became weak and disappeared in the spectra simultaneously with the Si II 6355 HVF. The absorption feature at 5500 Å has not been identified but could be due to an Na I/He I HVF with a velocity at around 17,500 km s⁻¹. Figure 13(b) shows the velocity evolution of Si II 6355 and the neighboring C II 6580 feature. The HVF of Si II 6355 is visible in the two earliest spectra, and it disappeared in the later ones. The presence of C II 6580 is obvious, as also illustrated by the SYNOW (Fisher et al. 1997) fit (red curves). The C II 6580 feature decreased in strength from t = -8.5 to 0 days, and it then became wider and stronger in the first week after the peak. Such an evolution is unusual for an SN Ia, and it is perhaps related to the interaction of the ejecta with the companion star or CSM. The evolution of the Ca II NIR triplet absorption feature is presented in Figure 13(c). In the Ca II NIR triplet, the HVF component is more separated from the photospheric component than in the Si II line, and it dominates at earlier phases but gradually loses its strength with time.

4.2. High-resolution Spectra

A few spectra presented in this paper were observed with higher resolutions, i.e., the two HET spectra taken at -8.5 and -5.5 days and the MMT spectrum taken at +20.5 days. These spectra are shown in Figure 14, where we can see some narrow spectral features that are barely visible in other low-resolution spectra. One can see that the absorption by Na I D and the diffuse interstellar band (DIB) at $\lambda 6283$ from the Milky Way are clearly visible in the high-resolution spectra, consistent with the presence of a modest level of Galactic reddening. There are some minor absorption features in the red wing of Si II 6355, which may also be related to unidentified DIBs. A few SNe have been reported to have host galaxy DIB detections in their spectra (D'Odorico et al. 1989; Sollerman et al. 2005;

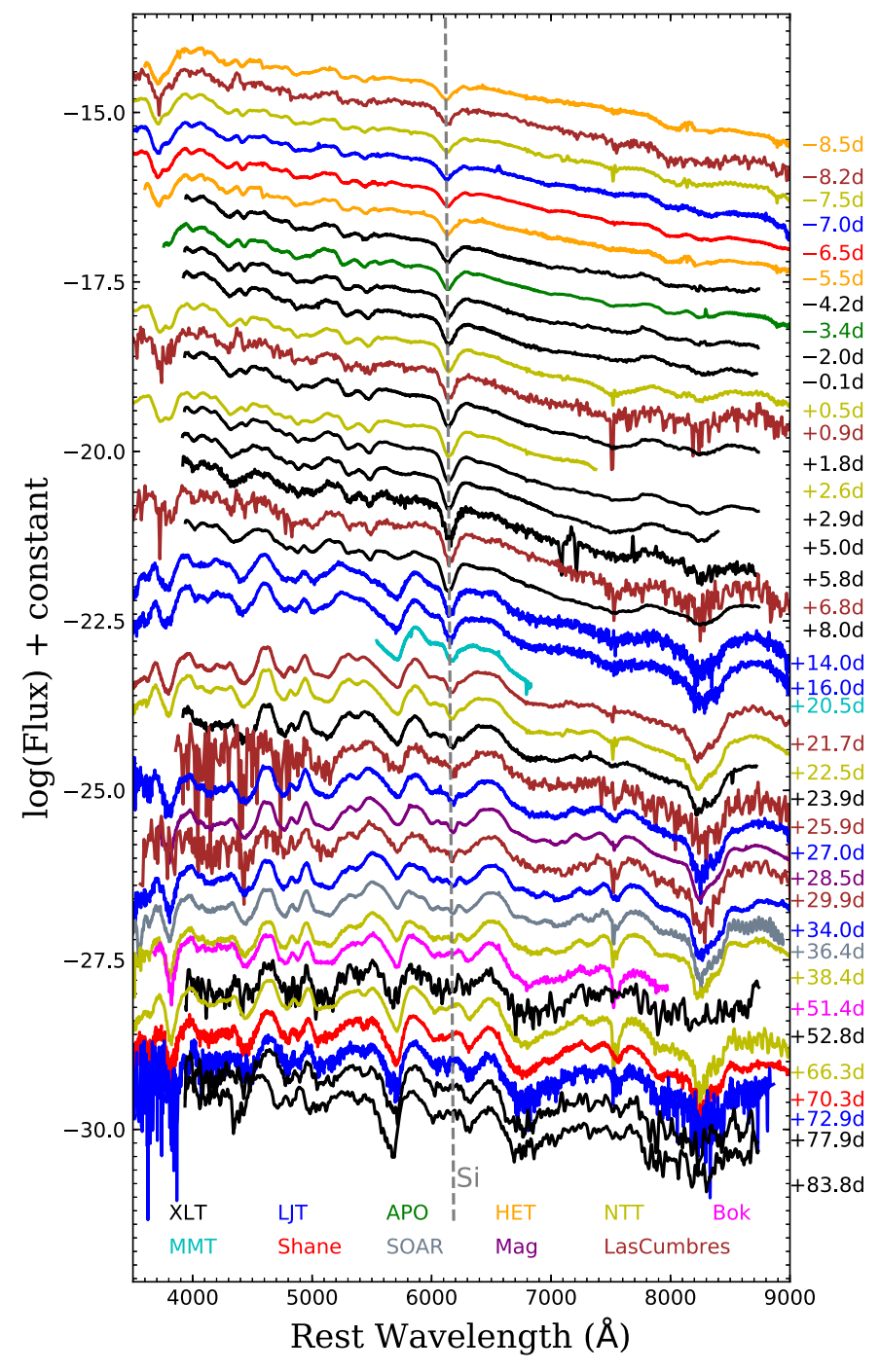


Figure 11. Spectral evolution of SN 2018oh (some spectra are not displayed due to limited space). The spectra have been corrected for the redshift of the host galaxy ($\nu_{hel} = 3270 \text{ km s}^{-1}$) and reddening, and the slopes of the continuum are calibrated by the photometry. For better display, the spectra have been shifted vertically by arbitrary amounts. The epochs on the right side of the spectra represent the phases in days from *B*-band maximum light. The colors of the spectra indicate the instrument used for the observations, as shown at the bottom of the figure.

Cox & Patat 2008; Phillips et al. 2013; Welty et al. 2014). The absence of Na I D and DIB absorption components from UGC 4780 is consistent with SN 2018oh suffering negligible reddening within the host galaxy. A weak, narrow H_{α} emission that is likely from the host galaxy feature can be clearly seen in both the HET and MMT spectra.

4.3. Carbon Features

There are C II features clearly detected in SN 2018oh, and they seem to persist for an unusually long time compared to other

known SNe Ia. As shown in Figure 15, the C II 6580 absorption feature can be detected in the spectra from t=-8.5 to +20.5 days. The C II 4267 and C II 7234 absorptions are also detectable in the spectra from t=-8.5 to +8.0 days. Identifying these carbon features is justified by the agreement in velocity at early phases (see

⁸⁴ Note that there is an instrumental trough around λ 4150 in the HET spectra that nearly coincides with the expected position of the C II λ 4267 feature, and this makes it difficult to judge whether the presence of this feature is real or not. Nevertheless, a weak C II λ 4267 feature can be still identified in the -7.5d spectrum taken by NTT, as shown in the top left panel of Figure 15.

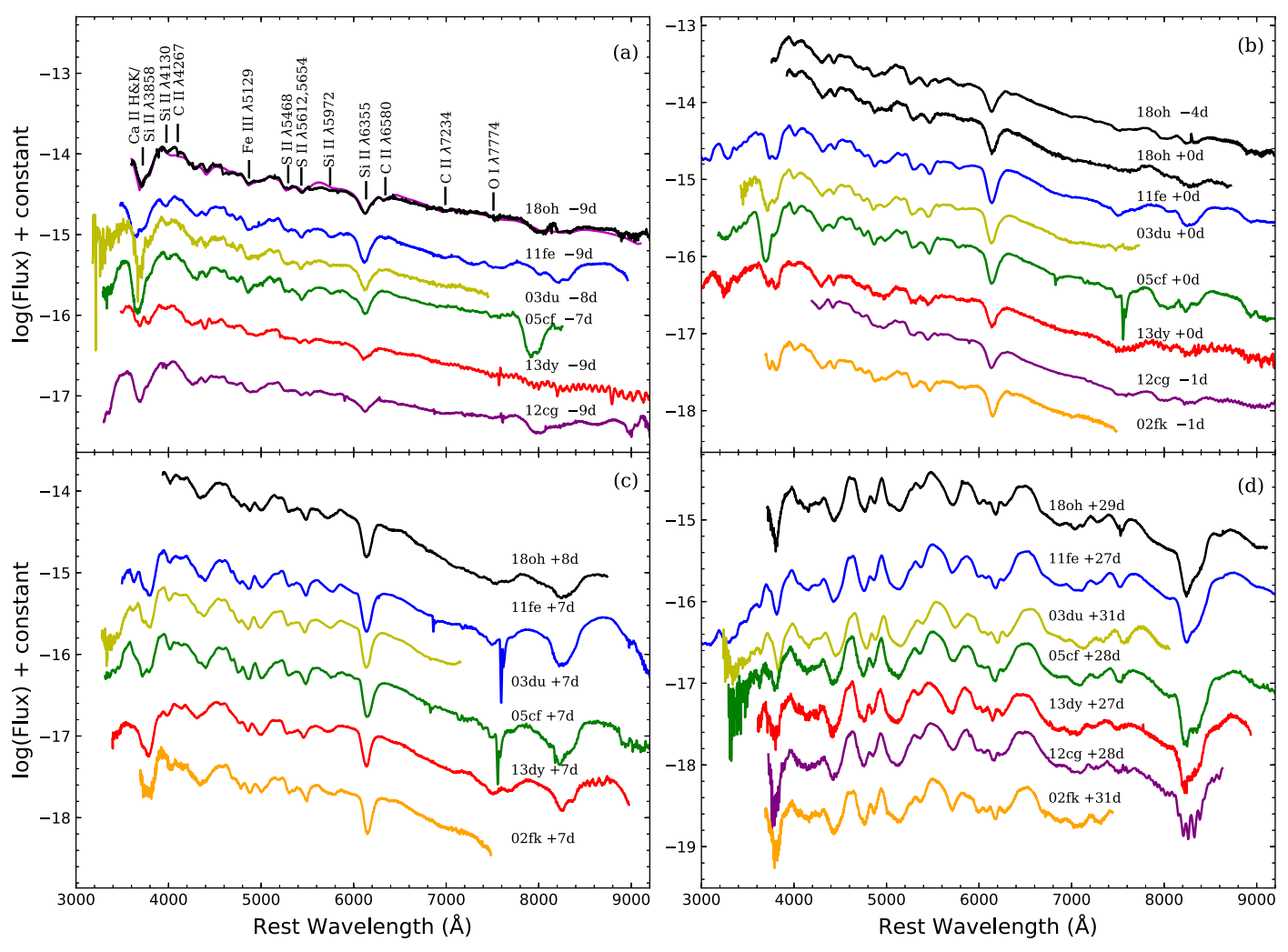


Figure 12. Spectra of SN 2018oh at $t \sim -9$, -4, 0, and +8 days and +1 month after *B* maximum, along with the comparable-phase spectra of SNe 2002fk (Blondin et al. 2012), 2003du (Stanishev et al. 2007), 2005cf (Garavini et al. 2007; Wang et al. 2009a), 2011fe (Mazzali et al. 2014; Zhang et al. 2016), 2012cg (Marion et al. 2016), and 2013dy (Zheng et al. 2013; Pan et al. 2015; Zhai et al. 2016). All spectra have been corrected for reddening and the redshift of the host galaxy. For clarity, the spectra were arbitrarily shifted in the vertical direction. The SYNOW fitting result of the $t \sim -9$ days spectrum of SN 2018oh is also overplotted in panel (a).

Figure 15) and the SYNOW spectral models. It should be noted that the SYNOW velocities shown in Figure 13 are higher than the measured values by $\sim\!2000\,\mathrm{km\,s^{-1}}$ (see Table 9). This offset is due to low optical depths at the line centers in the SYNOW fits producing a steep drop in optical depths blueward of the best-fit velocity, resulting in minimal absorption bluer than the line center, which shifts the apparent minimum in the line profile.

Silverman & Filippenko (2012) measured the velocity ratio between C II λ 6580 and Si II λ 6355 and found a median value of 1.05 at phases earlier than 4 days from maximum. For SN 2018oh, this ratio is 1.05–1.00 at $t \lesssim -4$ days, consistent with Silverman & Filippenko (2012). However, the C/Si velocity ratio keeps decreasing after $t \gtrsim -4$ days and reaches about 0.85 \pm 0.06 at $t \sim +20.5$ days for SN 2018oh, which suggests that unburned carbon may be more strongly mixed than silicon and extends deep into the ejecta.

Folatelli et al. (2012) calculated the pEW evolution of C II 6580 using SYNOW synthetic spectra with different unburned carbon mass. The pEW is found to grow monotonically with the mass of carbon. For SN 2018oh, the C II 6580 absorption has a pEW \sim 4 and 2 Å around -4.3 and -2.0 days, respectively, which is very similar to that of the synthetic spectra with \approx 0.03 M_{\odot} of unburned carbon in the ejecta.

4.4. Ejecta Velocity

We measured the ejecta velocities from the blueshifted absorption features of Si II $\lambda 6355$, S II $\lambda 5468$, C II $\lambda 6580$, C II λ 7234, O I λ 7774, and the Ca II NIR triplet lines, and the velocity evolution is shown in Figure 16. All velocities have been corrected for the host galaxy redshift. The photospheric velocity of Si II 6355, characterized by a linear decline from \sim 11,000 to \sim 8000 km s⁻¹, is comparable to that of other intermediate-mass elements at similar phases. Assuming a homologous expansion of the ejecta, this indicates a complex distribution of carbon in the ejecta. However, it is possible that the position of C II 6580 absorption in late-time spectra might be contaminated by other unknown elements. The best-fit C II velocities from SYNOW show an offset by $\sim 2000 \,\mathrm{km \, s^{-1}}$ relative to the measured values, and this suggests that carbon is detached until $\sim +5$ days from the maximum light. After that, the SYNOW velocity of C II becomes comparable to the photospheric values, matching that of Si II 6355.

The HVFs of Si II λ 6355, O I λ 7774, and the Ca II IR triplet have been systematically examined in the spectra of SNe Ia (Childress et al. 2014; Maguire et al. 2014; Silverman et al. 2015; Zhao et al. 2015, 2016). The HVFs of both Si II λ 6355

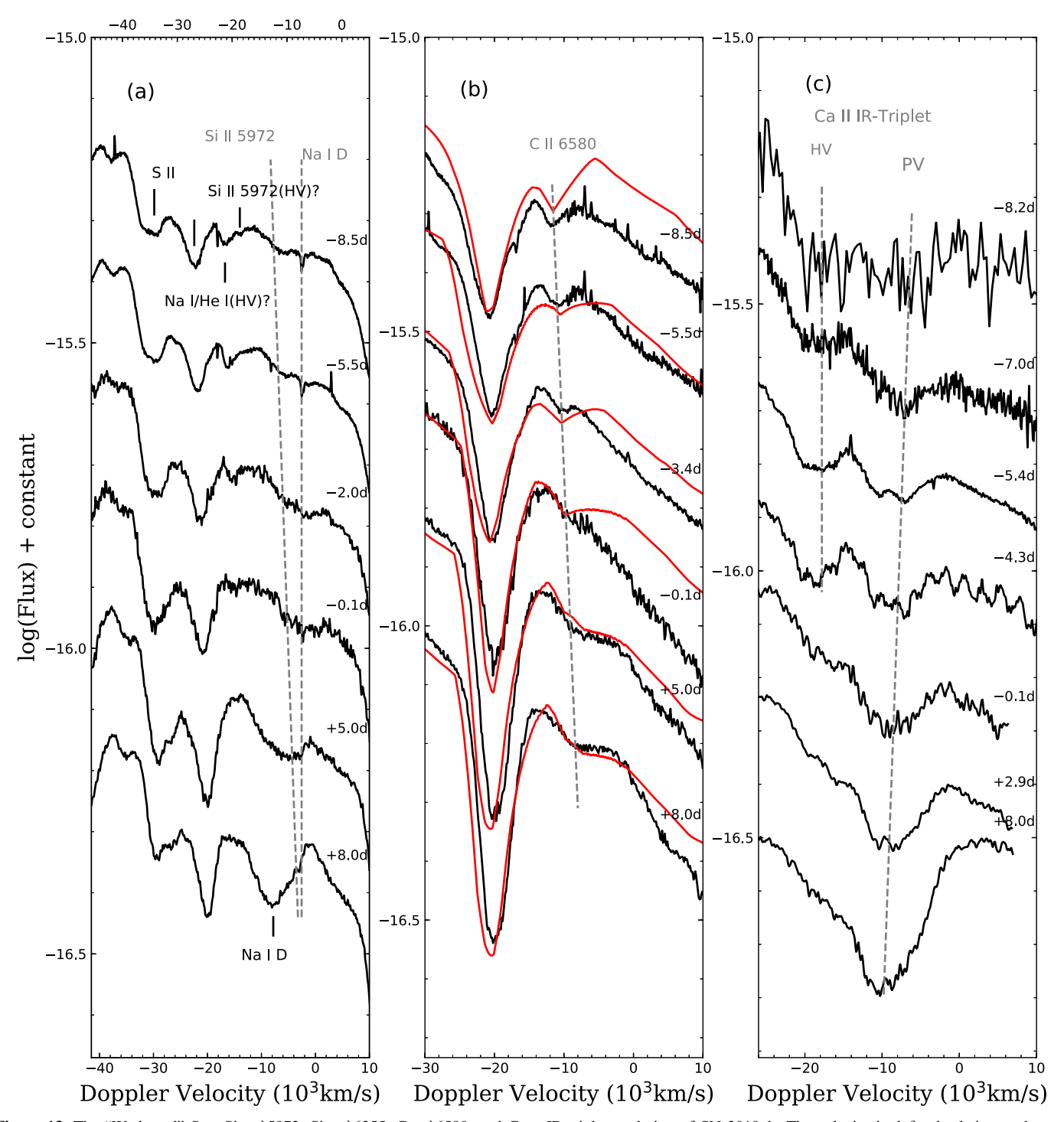


Figure 13. The "W-shaped" S II, Si II λ 5972, Si II λ 6355, C II λ 6580, and Ca II IR triplet evolution of SN 2018oh. The velocity is defined relative to the rest wavelength of (a) He I λ 5876 (upper axis: Si II λ 5972), (b) C II λ 6580, and (c) Ca II λ 8542. The black solid lines label spectral features, while the gray dashed lines indicate the velocity evolution trend for the corresponding lines. Overplotted red curves in panel (b) represent the best-fitting results from SYNOW.

and the Ca II IR triplet can be clearly identified in the early spectra of SN 2018oh. Since the region overlapping with the oxygen absorption has lower spectral quality for our early data, the O HVF cannot be clearly identified. The velocities measured for the HVFs identified for Si II λ 6355 and the Ca II NIR triplet can reach about 19,000–22,000 km s⁻¹, far above the photosphere. According to recent studies by Zhao et al. (2015, 2016), the HVFs cannot be explained by ionization and/or thermal processes alone, and different mechanisms are

required for the creation of HVF-forming regions. Mulligan & Wheeler (2017, 2018) showed that a compact circumstellar shell having $\lesssim 0.01\,M_\odot$ is capable of producing the observed HVF component of the Ca II NIR triplet.

In Figure 17, we compare the Si II velocity evolution of SN 2018oh with some well-observed SNe Ia. The v_{si} evolution of SN 2018oh is comparable to that of SN 2005cf and SN 2011fe, as shown in Figure 17. At around the *B*-band maximum light, SN 2018oh has an expansion velocity of 10,300 km s⁻¹, which

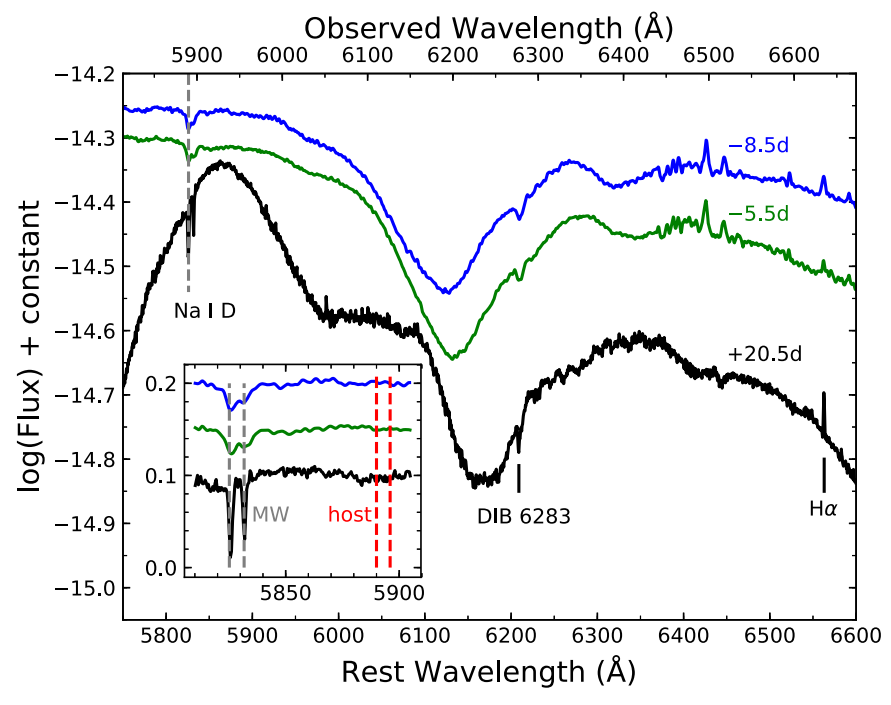


Figure 14. High-resolution spectra taken by the MMT and HET. Some narrow spectral features are labeled. The upper axis shows the observed wavelength. The inset shows the region of the Na I D doublet absorption features due to the Milky Way and the host galaxy.

can be clearly put into the normal velocity (NV) group according to the classification scheme proposed by Wang et al. (2009b). The velocity gradient of Si II λ 6355 during the first 10 days after $t_{\rm Bmax}$ is measured as $\dot{v}_{Si} = 69 \pm 4 \, {\rm km \, s^{-1} \, day^{-1}}$, which locates just around the boundary between HV-gradient (HVG) and low-velocity-gradient (LVG) objects (Benetti et al. 2005). A relatively fast velocity decline might be due to the collision of the ejecta with the nearby companion, as suggested by the early light curve observed by *Kepler* (Dimitriadis et al. 2018) or CSM. However, Shappee et al. (2018b) found that a single power-law rise with a nondegenerate companion or CSM interaction cannot well reproduce the early *Kepler* light curve. They derived that, at a radius of $4 \times 10^{15} \, {\rm cm}$ from the progenitor, the CSM density $\rho_{\rm CSM}$ is less than $4.5 \times 10^5 \, {\rm cm}^{-3}$.

5. Discussion

5.1. Origin of Persistent Carbon Absorption

The unburned carbon features in early spectra can help to discriminate between various explosion mechanisms or progenitor models for SNe Ia. Previous studies show that the C II signatures can be detected in 20%–30% of SNe Ia with ages younger than \sim -4 days from the maximum light, and >40% of SNe Ia have unburned carbon before -10 days (Parrent et al. 2011; Thomas et al. 2011; Silverman & Filippenko 2012; Maguire et al. 2014). The latest detection was at t=-4.4 days for SN 2008sl. In a late study, SN 2002fk showed carbon absorption lasting \sim +7 days after maximum (Cartier et al. 2014), and the 2002cx-like SN iPTF14atg showed C II λ 6580 absorption until about +2 weeks after maximum (Cao et al. 2015).

The carbon absorption persists in the spectra of SN 2018oh for an unusually long time. To examine this abnormal behavior, we further compare the C II 6580 evolution of SN 2018oh with some well-known SNe Ia with prominent carbon absorption features, including SN 2002fk, SN 2009dc, SN 2011fe, SN

2013dy, and iPTF14atg, in Figure 18. The C II absorption is strong in the t=-8.5 and -5.5 days spectra of SN 2018oh. After that, the C II 6580 tends to become flattened, which was not seen in other normal SNe Ia. The strength of the carbon absorption features is found to decrease with time (except for the period at t=-13 to -11 days from the maximum light; Silverman & Filippenko 2012). However, the strength of the C II λ 6580 absorption of SN 2018oh increases after the *B* maximum.

For SN 2012cg and SN 2017cbv, the C II λ 6580 of the former lasted until -8 days (Silverman et al. 2012), while it disappeared in the t = -13 days spectrum of the latter (Hosseinzadeh et al. 2017). The super-Chandrasekhar (SC) SN Ia-like SN 2009dc is known to show prominent carbon absorption (Howell et al. 2006; Scalzo et al. 2010; Silverman et al. 2011; Taubenberger et al. 2011). The C II 4267 absorption is difficult to identify due to several Fe-group features in this wavelength region. It was previously identified in SNLS 03D3bb and SN 2006D (Howell et al. 2006; Thomas et al. 2007), while Scalzo et al. (2010) proposed that this feature might be due to Cr II absorption. However, this feature in SN 2018oh has a similar velocity and strength evolution to that of C II 6580 until $t \sim +8.0$ days (see Figure 15), unlike SN 2009dc (Taubenberger et al. 2011). This gives us more confidence in the identification of C II 4267 absorption in SN 2018oh.

In theory, the pulsating delayed-detonation (PDD) model predicts the presence of carbon in the outer ejecta during the pulsation period (Hoeflich et al. 1996). Dessart et al. (2014) claimed that PDD can leave more unburned carbon than standard delayed-detonation models and thus produce prominent C II lines in the spectra. However, these C II features should disappear within 1 week after explosion. Their models can reproduce the strong C II lines of SN 2013dy but cannot explain the long-lasting C II lines seen in SN 2018oh.

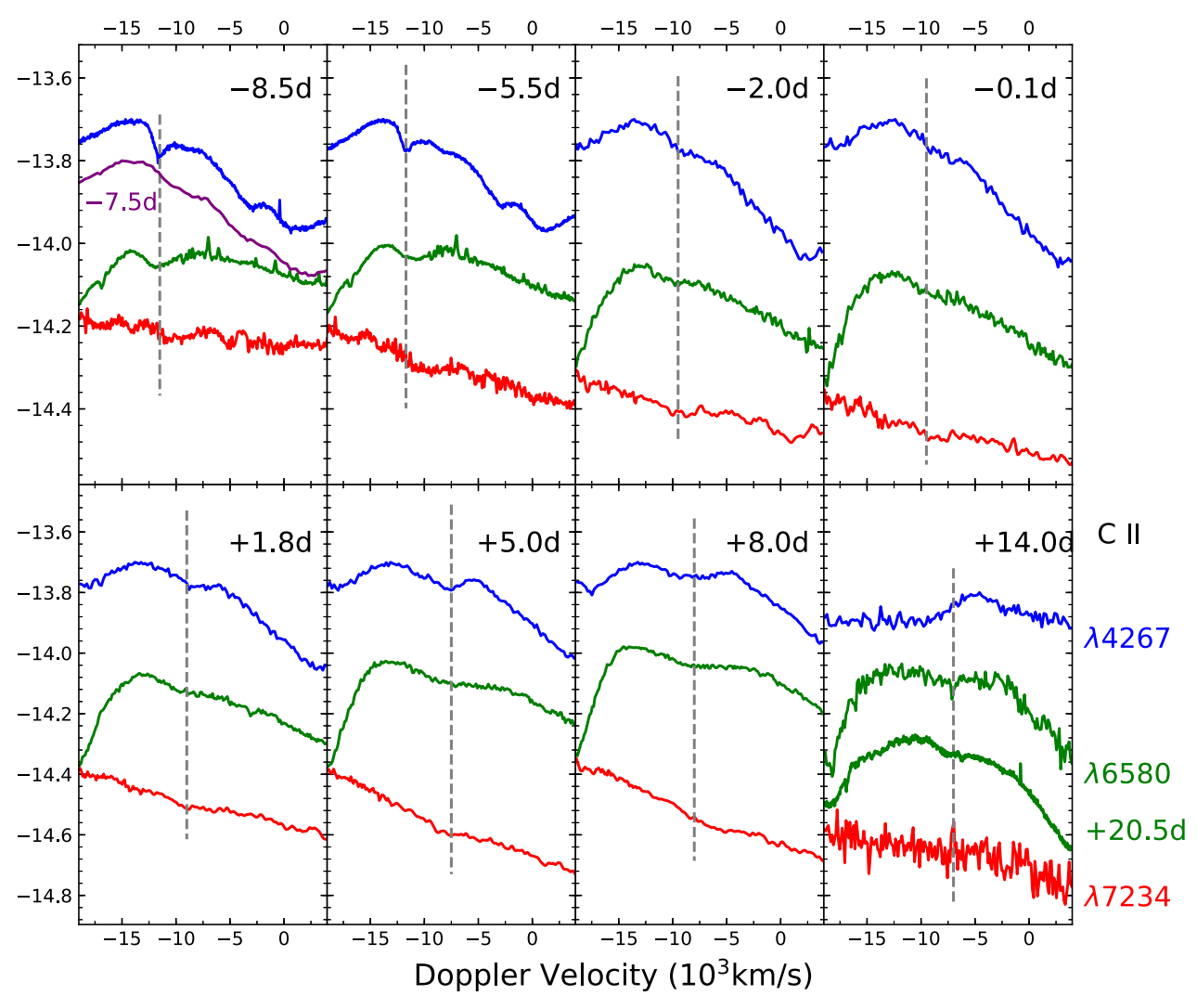


Figure 15. The C II λ 4267, λ 6580, and λ 7234 evolution of SN 20180h in velocity space. Three lines in each subplot are from one spectrum. The purple line in the top left panel displays the C II λ 4267 feature from the -7.5 days spectrum taken by NTT. The gray lines indicate the approximate velocity of the three features.

Table 9
SYNOW Fitting Parameters of SN 2018oh

		Si II			Са п					_
Phase (days)	$T_{\rm bb}$ (kK)	λ 6355 (HV) (10 ³ km s ⁻¹)	Si II $\lambda 6355$ (10^3 km s^{-1})	C II $\lambda 6580$ (10^3 km s^{-1})	$\lambda 8498 \text{ (HV)} $ (10^3 km s^{-1})	Ca II $\lambda 8498$ (10^3 km s^{-1})	S II $\lambda 5454$ (10^3 km s^{-1})	O I $\lambda 7774$ (10^3 km s^{-1})	Fe III $\lambda 5129$ (10^3 km s^{-1})	Fe III $\lambda 4404$ (10^3 km s^{-1})
-8.0	10.20	14.13	11.90	14.00	19.25	12.56	10.40	10.69	10.29	9.81
-5.5	11.20	14.49	11.80	14.00	18.36	11.12	10.34	11.16	10.18	9.81
-3.0	11.81	13.77	11.95	14.50	18.65	11.86	9.63	9.77	9.88	10.15
+0.0	10.45	12.28	11.10	12.00	18.76	10.64	9.52	9.37	10.06	10.08
+5.0	9.79	12.60	9.75	10.00	19.59	12.17	9.57	10.68	10.18	9.67
+8.0	9.41	12.61	9.42	9.67	19.48	11.32	9,79	10.58	10.12	10.15
+14.0	9.43	•••	10.15	8.16		12.43	9.74	10.69	10.06	9.54

Heringer et al. (2017) suggested that the emission of iron near 6100 Å can smear out the C II 6580 absorption. Thus, a smaller amount of IGEs in the outer ejecta could explain the prominent carbon feature in SN 2018oh, which could be due to stringent abundance stratification or lower metallicity for the progenitor. For example, SN 2013cv was a transitional SN Ia between normal and SC SNe Ia with persistent C II 6580 and 7234 until 1 week after maximum. It has high UV luminosity, and its early-phase spectra were absent of Fe II/III features,

suggestive of strong stratified structure in the explosion ejecta and hence the progenitor (Cao et al. 2016). Exhibiting relatively weaker Fe III $\lambda 5129$ than SN 2003du, SN 2005cf, and SN 2011fe (Section 4.1), SN 2018oh has blue UV color (see Figure 7), which suggests that it suffered less mixing in the explosion ejecta.

As an alternative explanation for the abundance stratification, it is possible that the progenitor of SN 2018oh has lower metallicity. In order to study the properties of the host galaxy,

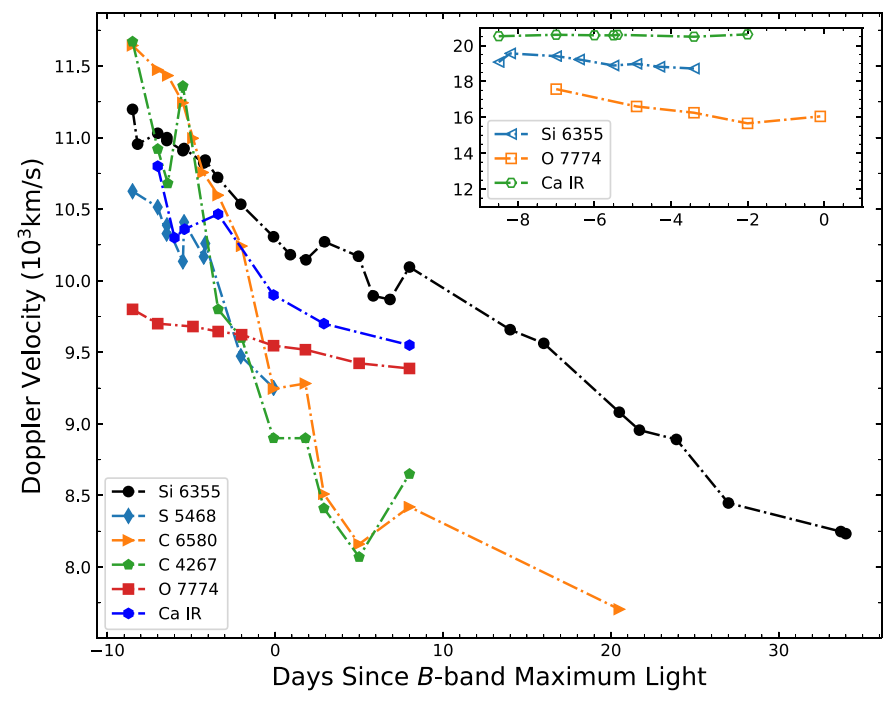


Figure 16. Evolution of the expansion velocity of SN 2018oh as measured from the absorption minimum of Si II λ 6355, S II 5640, C II 6580, C II 7234, O I 7774, and the Ca II NIR triplet. The inset plot illustrates the HV components of three features.

we downloaded the spectrum from the SDSS DR14 (Abolfathi et al. 2018). It corresponds to the light that falls within the 2''diameter fiber that is pointed at the center of the galaxy. Thus, to estimate the total mass of the galaxy, we scaled the synthetic broadband magnitudes measured from the spectrum to match the real photometric measurements of the integrated light of the galaxy (modelMag parameter). However, this procedure has a caveat: it makes the assumption that the mass-to-light ratio (M/L) obtained from the spectrum (and hence representative of the area inside the fiber) is the same as the one outside the fiber. Then, following Galbany et al. (2014), we performed simple stellar population (SSP) synthesis to the spectrum with STARLIGHT (Cid Fernandes et al. 2005) using the Granada-MILES bases (González Delgado et al. 2015) and fit all of the emission lines with Gaussian profiles in the subtracted gas-phase spectrum. We estimated a stellar mass of $\log_{10}(M_{\rm stellar}/M_{\odot}) \sim 6.87 \pm 0.12$, a star formation rate (SFR) of 5.54 ± 0.36 $10^{-4} M_{\odot} \text{yr}^{-1}$, and a subsolar oxygen abundance $12 + \log_{10}(O/H)$ of 8.49 ± 0.09 dex using the O3N2 calibration from Pettini & Pagel (2004), confirming that UGC 04780 is actually a metal-poor galaxy. These findings are in total agreement with reported numbers in the SDSS DR14 from different methods and codes.⁸⁵ In comparison, Shappee et al. (2018b) derived a larger mass of $4.68^{+0.33}_{-0.61}$ \times $10^8 \,\mathrm{M}_\odot$ from *GALEX* and PS1 photometry; they suggested that this value can be regarded as an upper limit, which is thus not inconsistent with our determination.

Based on the above discussions, we suggest that the outer ejecta of SN 2018oh may have few IGEs as a result of less mixing and/or a metal-poor progenitor, which could explain

the presence of a prominent and persistent C II 6580 absorption feature in the spectra.

5.2. Bolometric Light Curves and Explosion Parameters

The extensive photometric observations of SN 20180h enable us to construct a UVOIR "bolometric" light curve spanning the wavelength region from 0.16 to $2.3~\mu m$. The spectral energy distribution (SED) includes the uvw2, uvm2, uvw1, U, g, r, i, Y, J, H, and K bands. We interpolated the UV, optical, and NIR photometry from their neighboring epochs or the corresponding template light curves whenever necessary. The final SED evolution is displayed in Figure 19. Adopting the distance $d = 52.7 \pm 1.2$ Mpc from Section 3.3, the bolometric luminosity evolution is shown in the left panel of Figure 20. Like other comparison SNe Ia (except for SN 2005cf), SN 2018oh reached its peak about 1.5 days earlier than the B-band maximum. The overall shape of the light curve is quite similar to that of SN 2017cbv and shows an apparently slower rise compared to SN 2003du.

To estimate the nickel mass and other physical parameters of the ejecta, we apply the radiation diffusion model of Arnett (1982; see also Chatzopoulos et al. 2012). Adopting the constant opacity approximation, we fit the bolometric light curve using the Minim code (Chatzopoulos et al. 2013). The fit parameters are the time of "first light" t_0 (see below), the initial mass of the radioactive nickel $M_{\rm Ni}$, the light-curve timescale $t_{\rm lc}$, and the gamma-ray leaking timescale t_{γ} (see, e.g., Chatzopoulos et al. 2012 for details).

If t_0 is constrained to the moment of first light in the *Kepler* data (MJD 58,144.3 \pm 0.1), we get $M_{\rm Ni}=0.662\pm0.003\,M_{\odot}$, $t_{\rm lc}=14.89\pm0.07$ days, and $t_{\gamma}=39.56\pm0.18$ days. The model light curve is plotted as a green dashed line together with the observations in the right panel of Figure 20. It is seen that this model poorly fits the light curve, because it deviates from the observed data systematically before and around

⁸⁵ http://skyserver.sdss.org/dr14/en/tools/explore/parameters.aspx?id=1237667430628982959&spec=2573869371524933632&apid=&fieldd=0x112d13f880b60000&ra=136.664749886541&dec=19.3362515108894&plateId=2573807249117964288

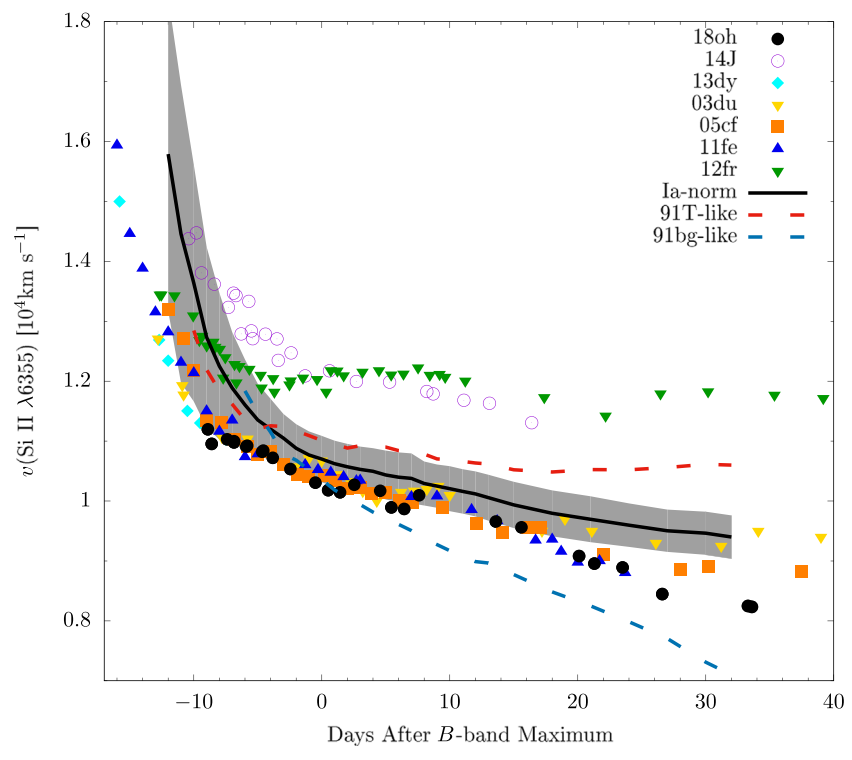


Figure 17. Velocity evolution of SN 2018oh as measured from the absorption minimum of Si II 6355, compared with SNe 2003du, 2005cf, 2011fe, 2012cg, and 2013dy (see text for the references). Overplotted are the mean curves of velocity evolution obtained for SN 1991T-like (red dashed), SN 1991bg-like (blue dotted), and normal (solid black) subclasses of SNe Ia (Wang et al. 2009b). The shaded region represents the 1σ uncertainty for the mean velocity curve of normal SNe Ia.

maximum light: the model is too bright at $\sim+10$ days, while it is too faint (although still within the error bars) compared to the data around the maximum.

The fit quality improves when t_0 is optimized: the model having $t_0 = +3.85 \pm 0.13$ days (black curve in Figure 20) fits the data much better and does not show the kind of systematic deviations around maximum that the model with $t_0 = 0$ does. Having $t_0 > 0$ means that the radioactivity-powered light curve starts to rise \sim 3.8 days after the first light seen by *Kepler*. This is consistent with the finding by Shappee et al. (2018b), who pointed out that the early K2 light curve of SN 2018oh could be modeled with two power laws having different starting moments $(t_1 \text{ and } t_2)$ that are separated by $t_2 - t_1 \sim 4$ days to produce a much better fit than with a single power law starting at MJD 58,144.3. Within the framework of the radiative diffusion model, their second power law ($\sim t^{1.4}$) can be associated with the initial phase of the light curve emerging from the homologously expanding, quasi-spherical SN ejecta that is powered by the radioactive decay of ⁵⁶Ni and ⁵⁶Co located in the center of the ejecta. Such a delay between the moment of explosion and the emergence of the radioactivity-powered light curve is predicted in some SN Ia models as the "dark phase" (Piro & Nakar 2013, 2014; Piro & Morozova 2016) caused by the location of the radioactive ⁵⁶Ni within the ejecta. The duration of the dark phase is determined by the initial diffusion time of the deposited radioactive energy between the location of ⁵⁶Ni and the surface of the ejecta. The Arnett model does not contain such a dark phase because it assumes an initial temperature distribution that remains spatially constant during the SN evolution; i.e., at t = 0, the initial diffusion wave already reached the surface. Piro & Morozova (2016) predicted the length of the dark phase as \lesssim 2 days, while our result ($t_0 \sim 3.8$) is almost a factor of 2 longer. However, after taking into account the model-dependent uncertainties involved in such an estimate, our result of $t_0 \sim 3.8$ days could be interpreted as being this dark phase; i.e., it is the timescale of the initial diffusion wave propagating between the center and the surface of the ejecta.

From our best-fit Arnett model, we also get $t_{\rm lc} = 10.81 \pm 0.14$ days, $t_{\gamma} = 41.36 \pm 0.18$ days, and $M_{\rm Ni} = 0.55 \pm 0.01 \, M_{\odot}$. The ejecta mass $(M_{\rm ej})$ and expansion velocity $(v_{\rm exp})$ are related to the model timescales $(t_{\rm lc}$ and $t_{\gamma})$ as

$$t_{\rm lc}^2 = \frac{2\kappa M_{\rm ej}}{\beta c v_{\rm exp}}$$
 and $t_{\gamma}^2 = \frac{3\kappa_{\gamma} M_{\rm ej}}{4\pi v_{\rm exp}^2}$, (1)

(Arnett 1982; Clocchiatti & Wheeler 1997; Valenti et al. 2008; Chatzopoulos et al. 2012; Wheeler et al. 2015), where κ is the effective optical opacity, κ_{γ} is the opacity for γ rays (assuming full trapping of positrons released in the cobalt decay), and $\beta \sim 13.8$ is the light-curve parameter related to the density profile of the ejecta (Arnett 1982). Combining $t_{\rm lc}$ and t_{γ} , one can find a self-consistent solution for $M_{\rm ej}$ and $v_{\rm exp}$ (or the kinetic energy $E_{\rm kin}=0.3M_{\rm ej}v_{\rm exp}^2$), depending on the chosen value of κ , because the γ -ray opacity is well constrained as $\kappa_{\gamma}\sim 0.03~{\rm cm^2~g^{-1}}$ (Wheeler et al. 2015). There are additional constraints for the other parameters, as $M_{\rm ej}$ must not exceed the Chandrasekhar mass, and $v_{\rm exp}$ must be at least as large as the observed expansion velocities (Section 4.4). For SN 2018oh, $v_{\rm exp}>11,000~{\rm km~s^{-1}}$ requires $\kappa\lesssim 0.09~{\rm cm^2~g^{-1}}$, while $M_{\rm ej}\lesssim M_{\rm Ch}$ implies $\kappa\gtrsim 0.08~{\rm cm^2~g^{-1}}$. Adopting $\kappa\sim 0.085~{\rm cm^2~g^{-1}}$ as a fiducial value, we get $M_{\rm ej}=1.27\pm0.15\,M_{\odot}$ and $E_{\rm kin}=1.08\pm0.25\times10^{51}~{\rm erg}$ (the quoted uncertainties

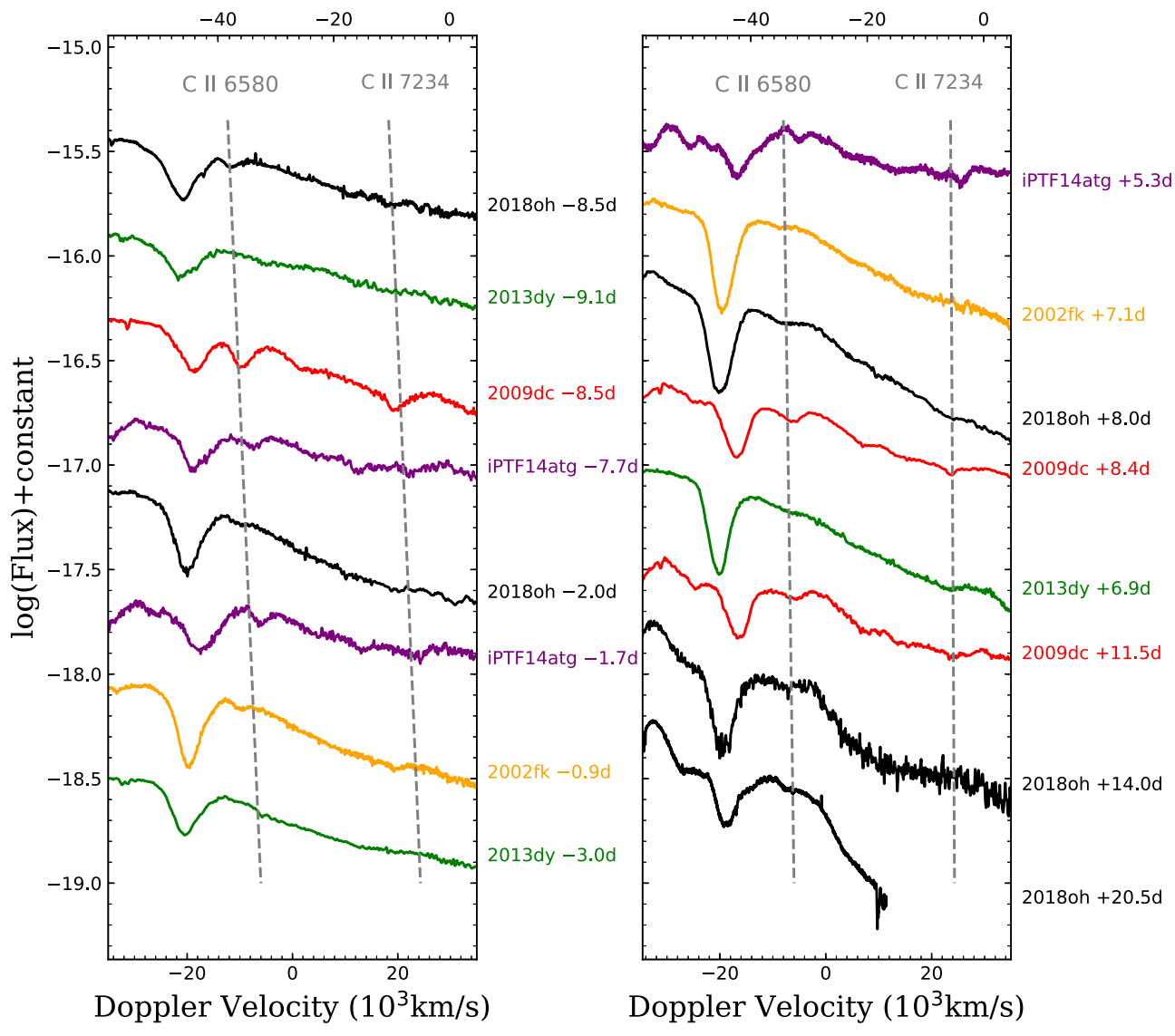


Figure 18. The C II λ6580 evolution of SN 2018oh compared to that of SN 2003du, SN 2011fe, iPTF14atg, and SN 2002fk. The gray dashed lines indicate the velocity evolution trend for the corresponding lines.

reflect the upper and lower value of κ given above). These values are close to the typical ejecta masses and kinetic energies for SNe Ia (e.g., Scalzo et al. 2014a, 2014b).

The uncertainty in the true explosion date has a consequence for the nickel mass estimate. Our first model having t_0 fixed to the moment of first light in the K2 light curve gives $M_{\rm Ni}$ \sim $0.66\,M_{\odot}$, which is very similar to the estimate of $M_{\rm Ni}=0.64\,\pm$ $0.04\,M_{\odot}$ based on "Arnett's rule" (Arnett 1982; Arnett et al. 1985; Branch & Tammann 1992; Stritzinger & Leibundgut 2005; Chatzopoulos et al. 2012). Both of these estimates predict $\sim 0.1 \, M_{\odot}$ higher nickel mass than our best-fit Arnett model described above, due to the \sim 3.5 days longer rise time to maximum light. Since this model gives a much better description of the evolution of the bolometric light curve, we adopt its final nickel mass of $M_{\rm Ni} = 0.55 \pm 0.04 \, M_{\odot}$. This is very similar to the estimate of $\sim 0.57 \, M_{\odot}$ for SN 2011fe (Zhang et al. 2016) and smaller than the estimates of 0.77 \pm 0.11 M_{\odot} for SN 2005cf (Wang et al. 2009a) and 0.68 \pm 0.14 M_{\odot} for SN 2003du (Stanishev et al. 2007).

All of these are based on the assumption that the bolometric light curve of SN 2018oh is entirely powered by the Ni-Co radioactive decay located centrally within the ejecta (Arnett 1982). The early linear rise of the flux observed by Kepler, which could be due to either the interaction with a close companion star (Dimitriadis et al. 2018) or the presence of radioactive ⁵⁶Ni in the outer layers of the ejecta and/or interaction with a nearby CSM (Shappee et al. 2018b), suggests that the assumptions of the Arnett model are not entirely fulfilled. For example, in the interaction model, the flux from the early shock may contribute to the full bolometric light curve nonnegligibly, even around and after maximum light. Subtracting the prediction of the shock-interaction model by Kasen (2010), assuming a Roche-lobe-filling companion at $A \sim 2 \times 10^{12}$ cm from the exploding white dwarf (Dimitriadis et al. 2018) and an optimal viewing angle, would yield $M_{\rm Ni} = 0.54 \pm 0.01 \, M_{\odot}$, $t_{\rm lc} = 10.96 \pm 0.17 \, {\rm days}$, and $t_{\gamma} = 37.89 \pm 0.17$ days. Thus, while $M_{\rm Ni}$ and $t_{\rm lc}$ are not changed significantly, the post-maximum contribution from the shock may slightly decrease the γ -ray leaking timescale. Finally, one

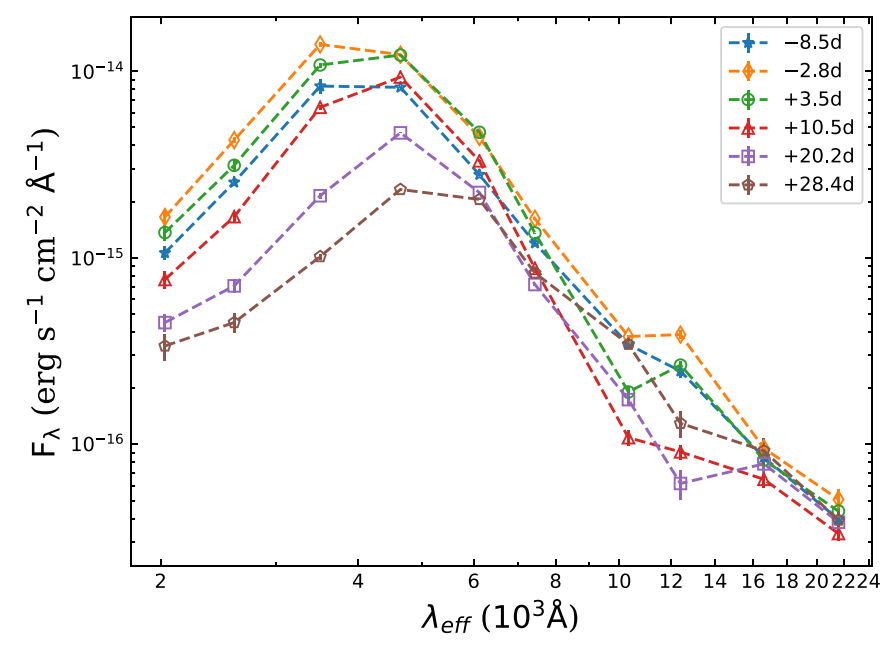


Figure 19. The SED evolution of SN 2018oh. The circles indicate the effective wavelengths of different bands.

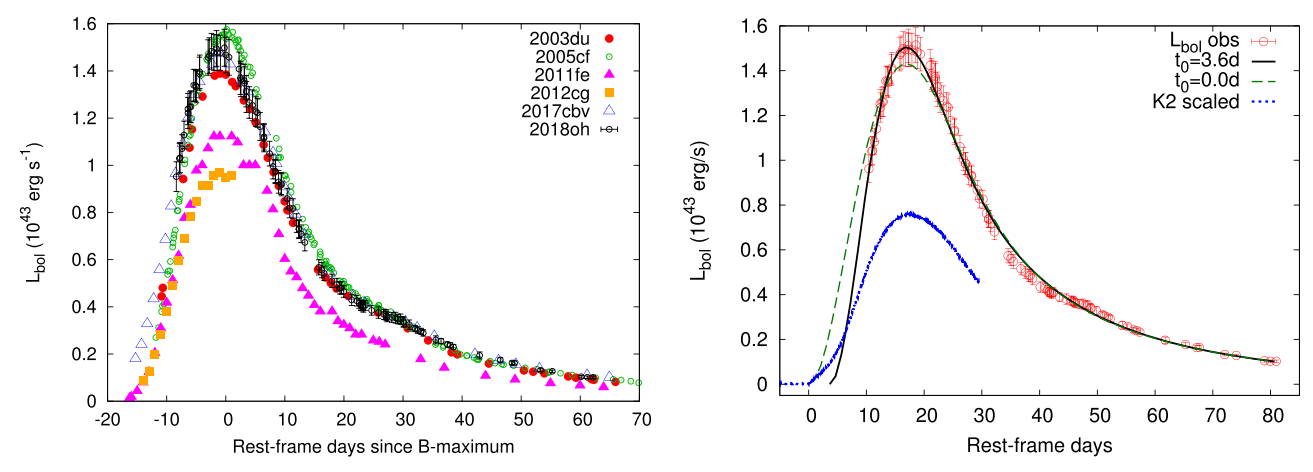


Figure 20. Left panel: luminosity evolution of SN 2018oh compared with that of SNe 2003du, 2005cf, 2011fe, 2012cg, and 2017cbv. Due to the distance uncertainty of SN 2017cbv, we shift it to match the peak of SN 2018oh. Right panel: bolometric light curve (open symbols) with radiation diffusion Arnett models (black curves). The solid line shows the best-fit model, while the dashed line represents the model when the time of explosion is fixed to the appearance of the first light in the *Kepler* data. The scaled *K2* light curve (see Section 2.3) is plotted with a blue dotted line.

can get $\kappa \sim 0.10 \pm 0.1~{\rm cm^2~g^{-1}}$, $M_{\rm ej} \sim 1.15 \pm 0.23\,M_{\odot}$, and $E_{\rm kin} \sim 1.06 \pm 0.4~\times~10^{51}$ erg using the same model as above. Although these parameters are somewhat less than those estimated from the pure Ni–Co model above, they are consistent within their uncertainties. The contribution of an early shock does not have a significant effect on the parameters estimated from the bolometric light curve.

We then compare observational properties and fitting parameters of SN 2018oh with two explosion models of SNe Ia. A thermonuclear explosion near the center of the C + O WD triggered by the detonation of He near the surface of the progenitor (the He detonation scenario; Jiang et al. 2017; Noebauer et al. 2017; Maeda et al. 2018) can produce early flux excess. Our explosion parameters are similar to model 10A/N from Maeda et al. (2018). One major effect of spectral evolution by model 10A/N is the Ti trough at ~ 4000 Å around maximum.

However, we do not see such a feature in our spectra. Therefore, we disfavor this scenario for SN 2018oh. Gravitationally confined detonation (the GCD model; Plewa et al. 2004; Kasen & Plewa 2007; Jordan et al. 2008) is another possible explosion mechanism. In the GCD, a deflagration off-center bubble ignited near the stellar core quickly rises toward the stellar surface with a lateral velocity component that will converge at the opposite side. There, a runaway detonation may be triggered. Seitenzahl et al. (2016) use 3D simulations to produce synthetic observables for one model, GCD200, which met their very optimistic detonation criteria. However, they yielded a nickel mass of $0.74\,M_{\odot}$, which is much larger than that of SN 2018oh. The GCD200 model also failed to reproduce the secondary peak in the I-band light curve. Nevertheless, the GCD model might explain the bump feature in the Kepler data of SN 2018oh, as it has a strong dependence on viewing angle caused by asymmetric

deflagration ashes. The UV flux is expected to enhance if the SN was observed at a viewing angle near the detonation ignition side. However, this specific viewing angle does not produce synthetic spectra that are consistent with the observed ones over multiple epochs. Thus, we conclude that the current GCD200 model cannot explain the bulk properties of SN 2018oh.

6. Conclusion

We present extensive follow-up photometry and spectroscopy for SN 2018oh, the first spectroscopically confirmed SN Ia (at a distance of 52.7 Mpc) observed by *Kepler*. SN 2018oh reached its *B*-band peak on MJD = 58,162.7 \pm 0.3 with an apparent magnitude of $B_{\rm max} = 14.31 \pm 0.03$ and an absolute magnitude of $M_{\rm max}^B = -19.47 \pm 0.10$. It has normal photometric evolution, with a rise time of 18.3 ± 0.3 days and $\Delta m_{15}(B) = 0.96 \pm 0.03$ mag, but it seems to have a relatively bluer B-V color.

Using three light-curve models, we derive a distance to the host galaxy of UGC 4780 as $d = 52.7 \pm 1.2$ Mpc. UGC 04780 is a star-forming dwarf galaxy with $\log_{10}(M_{\rm stellar}/M_{\odot}) \sim$ 6.87 ± 0.12 and a low metallicity. Based on the extensive UV/optical/NIR photometry, we established the generic bolometric light curve of SN 2018oh. Fitting Arnett's radiation diffusion model powered by radioactive decay of Ni and Co to the bolometric light curve, we derived a peak luminosity of $L_{\rm peak} = 1.49 \times 10^{43}\,{\rm erg\,s^{-1}}$ with a synthesized nickel mass $M_{\rm Ni} = 0.55 \pm 0.04\,M_{\odot}$. The moment when the luminosity begin to emerge in the radiation diffusion model, t_0 , is found to be +3.85 days after explosion. This is consistent with the hypotheses explored by Dimitriadis et al. (2018) and Shappee et al. (2018b) that the early flux is either due to interaction between the ejecta and some nearby material (a nondegenerate companion star or a CSM) or a noncentral location of the radioactive ⁵⁶Ni within the ejecta, and it does not emerge directly from the SN ejecta. In addition, we also explored two SN Ia explosion models, He detonation and gravitationally confined detonation, though neither of them can fully explain the properties of SN 2018oh.

The overall spectral evolution of SN 2018oh is similar to that of normal SNe Ia like SN 2003du, but there are still some interesting features that distinguish it from other SNe Ia. For instance, the line-strength ratio of Si II $\lambda\lambda$ 5958, 5979 to Si II $\lambda 6355$ (R(Si II)) is found to increase from the early phase to t = -4 days and then decrease toward the maximum light, suggesting a fluctuation of the photospheric temperature consistent with the line profile change of C II 6580. We can put SN 2018oh into the Branch SS subtype or at the boundary between SS and core-normal subtypes based on the pEWs of Si II $\lambda\lambda$ 5972, 6355, similar to a few other SNe Ia showing excess emissions in the early phase in Stritzinger et al. (2018). The velocity of Si II 6355 (i.e., $\sim 10{,}300 \pm 200 \,\mathrm{km \, s^{-1}}$ at $t \sim 0 \,\mathrm{days}$) suggests that SN 2018oh belongs to the normal subclass, but it shows a somewhat larger velocity gradient (near the boundary between the LVG and HVG groups) after the maximum light. The basic parameters of SN 2018oh are listed in Table 10.

The most striking spectral feature identified for SN 2018oh is the long-lasting C II absorption. We can identify C II 4267, 6580, and 7234 in early spectra, which all have similar velocity and strength evolution from $t \sim -9$ to +8 days. During this phase, the velocity of C II 6580 and 4267 decreases from $\sim 11,700$ to $\sim 8,000$ km s⁻¹, suggesting a strong mixing of carbon in the exploding ejecta. The C II 6580 absorption can even be detected

Table 10 Parameters of SN 2018oh

Parameter		Value
	Photometric	
$B_{ m max}$		$14.32 \pm 0.01 \; \mathrm{mag}$
$B_{\rm max} - V_{\rm max}$		$-0.09 \pm 0.02 \; \mathrm{mag}$
$E(B-V)_{\rm host}$		$0.00\pm0.04~\mathrm{mag}$
$\Delta m_{15}(B)$		$0.96 \pm 0.03 \; \mathrm{mag}$
$t_{\max}(B)$		$58,162.7 \pm 0.3 \text{ days}$
t_0		$58,144.37 \pm 0.04$ days
$ au_{ m rise}$		$18.3 \pm 0.3 \; {\rm days}$
$L_{\rm bol}^{\rm max}$		$1.49 \times 10^{43} \mathrm{erg \ s^{-1}}$
M56 Ni		$0.55 \pm 0.04 M_{\odot}$
	Spectroscopic	_
$v_0(Si II)$	1 1	$10,300 \pm 300 \mathrm{km s^{-1}}$
ν(Si II)		$69 \pm 4 \text{ km s}^{-1} \text{ day}^{-1}$
R(Si II)		0.15 ± 0.04

in the t = +20.5 days spectrum, which is never seen in other SNe Ia. The origin of the persistent carbon in SN 2018oh is unclear but may be related to the nature of progenitor systems such as lower metallicity. Detailed modeling is needed to clarify this issue.

This work is supported by Ma Huateng Foundation. We acknowledge the support of the staff of the Lijiang 2.4 m and Xinglong 2.16 m telescopes. Funding for the LJT has been provided by Chinese Academy of Sciences and the People's Government of Yunnan Province. The LJT is jointly operated and administrated by Yunnan Observatories and the Center for Astronomical Mega-Science, CAS. This work is supported by the National Natural Science Foundation of China (NSFC grants 11325313, 11633002, and 11761141001), the National Program on Key Research and Development Project (grant No. 2016YFA0400803), and the Tsinghua University Initiative Scientific Research Program (20161080144). This work was also partially supported by the Collaborating Research Program (OP201702) of the Key Laboratory of the Structure and Evolution of Celestial Objects, Chinese Academy of Sciences. This work is sponsored (in part) by the Chinese Academy of Sciences (CAS) through a grant to the CAS South America Center for Astronomy (CASSACA) in Santiago, Chile. J-JZ is supported by the NSFC (grants 11403096 and 11773067), the Key Research Program of the CAS (grant No. KJZD-EW-M06), the Youth Innovation Promotion Association of the CAS (grant 2018081), and the CAS "Light of West China" Program. FH is supported by the Collaborating Research Program (OP201702) of the Key Laboratory of the Structure and Evolution of Celestial Objects, Chinese Academy of Sciences.

This work makes use of observations from Las Cumbres Observatory. DAH, CM, and GH are supported by the US National Science Foundation under grant 1313484. Support for IA was provided by NASA through the Einstein Fellowship Program, grant PF6-170148. The work made use of *Swift/UVOT* data reduced by P. J. Brown and released in the *Swift Optical/Ultraviolet Supernova Archive (SOUSA)*. SOUSA is supported by NASA's Astrophysics Data Analysis Program through grant NNX13AF35G. Research by DJS is supported by NSF grants AST-1821967, 1821987, 1813708, and 1813466.

This work includes data obtained with the Swope Telescope at Las Campanas Observatory, Chile, as part of the Swope Time Domain Key Project (PI: Piro; co-PIs: Shappee, Drout, Madore, Phillips, Foley, and Hsiao). We thank I. Thompson

and the Carnegie Observatory Time Allocation Committee for approving the Swope project and scheduling this program. Parts of this research were supported by the Australian Research Council Centre of Excellence for All Sky Astrophysics in 3 Dimensions (ASTRO 3D) through project number CE170100013. EB and JD acknowledge partial support from NASA grant NNX16AB5G.

JV and his group at Konkoly Observatory are supported by the project "Transient Astrophysical Objects" GINOP 2.3.2-15-2016-00033 of the National Research, Development and Innovation Office (NKFIH), Hungary, funded by the European Union, and by the "Lendület" Program of the Hungarian Academy of Sciences, project Nos. LP2012-31 and LP2018-7/ 2018. This project has been supported by NKFIH grant K-115709. ZsB acknowledges the support provided by the National Research, Development and Innovation Fund of Hungary, financed under the PD 17 funding scheme, project No. PD123910. Support for JJH was provided by NASA through Hubble Fellowship grant #HST-HF2-51357.001-A, awarded by the Space Telescope Science Institute, which is operated by the Association of Universities for Research in Astronomy, Inc., under NASA contract NAS5-26555, as well as NASA K2 Cycle 4 grant NNX17AE92G.

Based on observations obtained at the Southern Astrophysical Research (SOAR) telescope, which is a joint project of the Ministério da Ciência, Tecnologia, e Inovação da República Federativa do Brasil, the U.S. National Optical Astronomy Observatory, the University of North Carolina at Chapel Hill, and Michigan State University.

Based in part on observations collected at the European Organisation for Astronomical Research in the Southern Hemisphere under ESO program 199.D-0143. LG was supported in part by the US National Science Foundation under grant AST-1311862. KM acknowledges support from the STFC through an Ernest Rutherford Fellowship and EU Horizon 2020 ERC grant No. 758638. CPG acknowledges support from EU/FP7-ERC grant No. [615929].

We thank the Las Cumbres Observatory and its staff for its continuing support of the ASAS-SN project. ASAS-SN is supported by the Gordon and Betty Moore Foundation through grant GBMF5490 to Ohio State University and NSF grant AST-1515927. Development of ASAS-SN has been supported by NSF grant AST-0908816, the Mt. Cuba Astronomical Foundation, the Center for Cosmology and AstroParticle Physics at Ohio State University, the Chinese Academy of Sciences South America Center for Astronomy (CASSACA), the Villum Foundation, and George Skestos.

SB, PC, and SD acknowledge Project 11573003, supported by NSFC. This research uses data obtained through the Telescope Access Program (TAP), which has been funded by the Strategic Priority Research Program—The Emergence of Cosmological Structures of the Chinese Academy of Sciences (grant No. 11 XDB09000000) and the Special Fund for Astronomy from the Ministry of Finance. The UCSC group is supported in part by NASA grants NNG17PX03C and 80NSSC18K0303, NSF grant AST-1518052, the Gordon & Betty Moore Foundation, the Heising-Simons Foundation, and fellowships from the Alfred P. Sloan Foundation and the David and Lucile Packard Foundation to RJF.

This paper includes data collected by the *K*2 mission. Funding for the *K*2 mission is provided by the NASA Science Mission directorate. KEGS is supported in part by NASA *K*2

cycle 4 and 5 grants NNX17AI64G and 80NSSC18K0302, respectively. AR and his groups are supported in part by *HST* grants GO-12577 and *HST* AR-12851.

Software: IRAF (Tody 1986, 1993), Minim (Chatzopoulos et al. 2013), FITSH (Pál 2012), SNCOSMO (Barbary et al. 2016), PESSTO pipeline (Smartt et al. 2015), SALT2.4 (Betoule et al. 2014), SNooPy2 (Burns et al. 2011), MLCS2k2 (Jha et al. 2007), photpipe (Rest et al. 2005, 2014), SYNOW (Fisher et al. 1997), STARLIGHT (Cid Fernandes et al. 2005), SExtractor (Bertin & Arnouts 1996).

ORCID iDs

```
X. Wang https://orcid.org/0000-0002-7334-2357
J. Vinkó https://orcid.org/0000-0001-8764-7832
G. Hosseinzadeh https://orcid.org/0000-0002-0832-2974
D. J. Sand https://orcid.org/0000-0003-4102-380X
J. Zhang https://orcid.org/0000-0002-8296-2590
E. Baron https://orcid.org/0000-0001-5393-1608
L. Wang https://orcid.org/0000-0002-1094-3817
C. McCully https://orcid.org/0000-0001-5807-7893
I. Arcavi https://orcid.org/0000-0001-7090-4898
S. Valenti https://orcid.org/0000-0001-8818-0795
P. Garnavich https://orcid.org/0000-0003-4069-2817
G. Narayan https://orcid.org/0000-0001-6022-0484
E. Shaya https://orcid.org/0000-0002-3234-8699
S. Margheim https://orcid.org/0000-0001-8205-9441
A. Villar https://orcid.org/0000-0002-5814-4061
D. A. Coulter https://orcid.org/0000-0003-4263-2228
O. D. Fox https://orcid.org/0000-0003-2238-1572
S. W. Jha https://orcid.org/0000-0001-8738-6011
D. O. Jones https://orcid.org/0000-0002-6230-0151
C. D. Kilpatrick https://orcid.org/0000-0002-5740-7747
A. L. Piro https://orcid.org/0000-0001-6806-0673
T. W.-S. Holoien https://orcid.org/0000-0001-9206-3460
K. Auchettl https://orcid.org/0000-0002-4449-9152
C. S. Kochanek https://orcid.org/0000-0001-6017-2961
J. S. Brown https://orcid.org/0000-0002-1885-6419
S. Bose https://orcid.org/0000-0003-3529-3854
D. Bersier https://orcid.org/0000-0001-7485-3020
J. A. Muñoz https://orcid.org/0000-0001-9833-2959
R. L. Mutel https://orcid.org/0000-0003-1511-6279
J. L. Prieto https://orcid.org/0000-0003-0943-0026
J. Shields https://orcid.org/0000-0002-1560-5286
S. J. Smartt https://orcid.org/0000-0002-8229-1731
K. C. Chambers https://orcid.org/0000-0001-6965-7789
H. A. Flewelling https://orcid.org/0000-0002-1050-4056
M. E. Huber https://orcid.org/0000-0003-1059-9603
E. A. Magnier https://orcid.org/0000-0002-7965-2815
C. Z. Waters https://orcid.org/0000-0003-1989-4879
J. Bulger https://orcid.org/0000-0003-4641-2003
K. Sárneczky https://orcid.org/0000-0003-0926-3950
A. Pál https://orcid.org/0000-0001-5449-2467
J. C. Wheeler https://orcid.org/0000-0003-1349-6538
Zs. Bognár https://orcid.org/0000-0002-8493-9781
O. Hanyecz https://orcid.org/0000-0002-9415-5219
R. Szabó https://orcid.org/0000-0002-3258-1909
R. Szakáts https://orcid.org/0000-0002-1698-605X
P. Milne https://orcid.org/0000-0002-0370-157X
P. J. Brown https://orcid.org/0000-0001-6272-5507
S. C. Williams https://orcid.org/0000-0002-4237-3994
L. Galbany https://orcid.org/0000-0002-1296-6887
```

I. M. Hook https://orcid.org/0000-0002-2960-978X

```
C. Inserra https://orcid.org/0000-0002-3968-4409
C. P. Gutiérrez https://orcid.org/0000-0002-7252-4351
J. L. Tonry https://orcid.org/0000-0003-2858-9657
A. N. Heinze https://orcid.org/0000-0003-3313-4921
B. Stalder https://orcid.org/0000-0003-0973-4900
G. Barentsen https://orcid.org/0000-0002-3306-3484
J. Dotson https://orcid.org/0000-0003-4206-5649
T. Barclay https://orcid.org/0000-0001-7139-2724
M. Gully-Santiago https://orcid.org/0000-0002-3385-8391
A. M. Cody https://orcid.org/0000-0002-3656-6706
S. Howell https://orcid.org/0000-0002-2532-2853
```

References

```
Abolfathi, B., Aguado, D. S., Aguilar, G., et al. 2018, ApJS, 235, 42
Albareti, F. D., Allende Prieto, C., Almeida, A., et al. 2017, ApJS, 233, 25
Aldering, G., Antilogus, P., Bailey, S., et al. 2006, ApJ, 650, 510
Arnett, W. D. 1982, ApJ, 253, 785
Arnett, W. D., Branch, D., & Wheeler, J. C. 1985, Natur, 314, 337
Barbary, K., Barclay, T., Biswas, R., et al. 2016, SNCosmo: Python library for
   supernova cosmology, Astrophysics Source Code Library, ascl:1611.017
Benetti, S., Cappellaro, E., Mazzali, P. A., et al. 2005, ApJ, 623, 1011
Bertin, E., & Arnouts, S. 1996, A&A, 117, 393
Betoule, M., Kessler, R., Guy, J., et al. 2014, A&A, 568, A22
Blondin, S., Matheson, T., Kirshner, R. P., et al. 2012, AJ, 143, 126
Branch, D., Dang, L. C., Hall, N., et al. 2006, PASP, 118, 560
Branch, D., & Tammann, G. A. 1992, ARA&A, 30, 359
Breeveld, A. A., Landsman, W., Holland, S. T., et al. 2011, in AIP Conf. Ser.
   1358, Gamma-Ray Bursts 2010 (Melville, NY: AIP), 373
Brown, J. S., Stanek, K. Z., Vallely, P., et al. 2018, ATel, 11253
Brown, P. J., Breeveld, A. A., Holland, S., Kuin, P., & Pritchard, T. 2014,
         S, 354, 89
Brown, P. J., Dawson, K. S., de Pasquale, M., et al. 2012, ApJ, 753, 22
Brown, P. J., Landez, N. J., Milne, P. A., & Stritzinger, M. D. 2017, ApJ,
Brown, T. M., Baliber, N., Bianco, F. B., et al. 2013, PASP, 125, 1031
Burns, C. R., Stritzinger, M., Phillips, M. M., et al. 2011, AJ, 141, 19
Burns, C. R., Stritzinger, M., Phillips, M. M., et al. 2014, ApJ, 789, 32
Buzzoni, B., Delabre, B., Dekker, H., et al. 1984, Msngr, 38, 9
Cao, Y., Johansson, J., Nugent, P. E., et al. 2016, ApJ, 823, 147
Cao, Y., Kulkarni, S. R., Howell, D. A., et al. 2015, Natur, 521, 328
Cardelli, J. A., Clayton, G. C., & Mathis, J. S. 1989, ApJ, 345, 245
Cartier, R., Hamuy, M., Pignata, G., et al. 2014, ApJ, 789, 89
Chambers, K. C., Magnier, E. A., Metcalfe, N., et al. 2016, arXiv:1612.05560
Chatzopoulos, E., Wheeler, J. C., & Vinko, J. 2012, ApJ, 746, 121
Chatzopoulos, E., Wheeler, J. C., Vinko, J., Horvath, Z. L., & Nagy, A. 2013,
     pJ, 773, 76
Childress, M. J., Filippenko, A. V., Ganeshalingam, M., & Schmidt, B. P.
   2014, MNRAS, 437, 338
Chonis, T. S., Hill, G. J., Lee, H., et al. 2016, Proc. SPIE, 9908, 99084C
Cid Fernandes, R., Mateus, A., Sodré, L., Stasińska, G., & Gomes, J. M. 2005,
    INRAS, 358, 363
Clemens, J. C., Crain, J. A., & Anderson, R. 2004, Proc. SPIE, 5492, 331
Clocchiatti, A., & Wheeler, J. C. 1997, ApJ, 491, 375
Contreras, C., Hamuy, M., Phillips, M. M., et al. 2010, AJ, 139, 519
Cousins, A. W. J. 1981, SAAOC, 6, 4
Cox, N. L. J., & Patat, F. 2008, A&A, 485, L9
D'Odorico, S., di Serego Alighieri, S., Pettini, M., et al. 1989, A&A, 215, 21
Dessart, L., Blondin, S., Hillier, D. J., & Khokhlov, A. 2014, MNRAS,
   441, 532
Dilday, B., Howell, D. A., Cenko, S. B., et al. 2012, Sci, 337, 942
Dimitriadis, G., Foley, R. J., Rest, A., et al. 2018, ApJL, 870, L1
Fan, Y.-F., Bai, J.-M., Zhang, J.-J., et al. 2015, RAA, 15, 918
Fisher, A., Branch, D., Nugent, P., & Baron, E. 1997, ApJL, 481, L89
Flaugher, B., Diehl, H. T., Honscheid, K., et al. 2015, AJ, 150, 150
Flewelling, H. A., Magnier, E. A., Chambers, K. C., et al. 2016, arXiv:1612.
Folatelli, G., Phillips, M. M., Morrell, N., et al. 2012, ApJ, 745, 74
Foley, R. J. 2012, ApJ, 748, 127
Foley, R. J., & Kasen, D. 2011, ApJ, 729, 55
Foley, R. J., Sanders, N. E., & Kirshner, R. P. 2011, ApJ, 742, 89
```

```
Galbany, L., Stanishev, V., Mourão, A. M., et al. 2014, A&A, 572, A38
Ganeshalingam, M., Li, W., Filippenko, A. V., et al. 2012, ApJ, 751, 142
Garavini, G., Nobili, S., Taubenberger, S., et al. 2007, A&A, 471, 527
Gehrels, N., Chincarini, G., Giommi, P., et al. 2004, ApJ, 611, 1005
González Delgado, R. M., García-Benito, R., Pérez, E., et al. 2015, A&A,
González Hernández, J. I., Ruiz-Lapuente, P., Tabernero, H. M., et al. 2012,
   Natur, 489, 533
Guy, J., Sullivan, M., Conley, A., et al. 2010, A&A, 523, A7
Haas, M. R., Batalha, N. M., Bryson, S. T., et al. 2010, ApJL, 713, L115
Hamuy, M., Phillips, M. M., Suntzeff, N. B., et al. 2003, Natur, 424, 651
Heringer, E., van Kerkwijk, M. H., Sim, S. A., & Kerzendorf, W. E. 2017, ApJ,
Hoeflich, P., Khokhlov, A., Wheeler, J. C., et al. 1996, ApJL, 472, L81
Honscheid, K., DePoy, D. L. & for the DES Collaboration 2008,
  arXiv:0810.3600
Hosseinzadeh, G., Sand, D. J., Valenti, S., et al. 2017, ApJL, 845, L11
Howell, D. A., Sullivan, M., Nugent, P. E., et al. 2006, Natur, 443, 308
Huang, F., Li, J.-Z., Wang, X.-F., et al. 2012, RAA, 12, 1585
Iben, I., Jr., & Tutukov, A. V. 1984, ApJS, 54, 335
Jha, S., Riess, A. G., & Kirshner, R. P. 2007, ApJ, 659, 122
Jiang, J.-A., Doi, M., Maeda, K., et al. 2017, Natur, 550, 80
Johnson, H. L., Mitchell, R. I., Iriarte, B., & Wisniewski, W. Z. 1966, CoLPL,
Jordan, G. C., IV, Fisher, R. T., Townsley, D. M., et al. 2008, ApJ, 681, 1448
Kasen, D. 2010, ApJ, 708, 1025
Kasen, D., & Plewa, T. 2007, ApJ, 662, 459
Krisciunas, K., Contreras, C., Burns, C. R., et al. 2017, AJ, 154, 211
Landolt, A. U. 1992, AJ, 104, 340
Leadbeater, R. 2018, Transient Name Server Classification Report 159, https://
  wis-tns.weizmann.ac.il/object/2018oh/classification-cert
Leonard, D. C. 2007, ApJ, 670, 1275
Li, W., Bloom, J. S., Podsiadlowski, P., et al. 2011, Natur, 480, 348
Maeda, K., Benetti, S., Stritzinger, M., et al. 2010, Natur, 466, 82
Maeda, K., Jiang, J.-a., Shigeyama, T., & Doi, M. 2018, ApJ, 861, 78
Magnier, E. A., Schlafly, E. F., Finkbeiner, D. P., et al. 2016, arXiv:1612.
Maguire, K., Sullivan, M., Pan, Y.-C., et al. 2014, MNRAS, 444, 3258
Maguire, K., Sullivan, M., Patat, F., et al. 2013, MNRAS, 436, 222
Maguire, K., Taubenberger, S., Sullivan, M., & Mazzali, P. A. 2016, MNRAS,
Mandel, K. S., Foley, R. J., & Kirshner, R. P. 2014, ApJ, 797, 75
Maoz, D., Mannucci, F., & Nelemans, G. 2014, ARA&A, 52, 107
Marion, G. H., Brown, P. J., Vinkó, J., et al. 2016, ApJ, 820, 92
Matheson, T., Joyce, R. R., Allen, L. E., et al. 2012, ApJ, 754, 19
Mattila, S., Lundqvist, P., Sollerman, J., et al. 2005, A&A, 443, 649
Maund, J. R., Höflich, P., Patat, F., et al. 2010, ApJL, 725, L167
Mazzali, P. A., Sullivan, M., Hachinger, S., et al. 2014, MNRAS, 439, 1959
Mennekens, N., Vanbeveren, D., De Greve, J. P., & De Donder, E. 2010,
   A&A, 515, A89
Miller, A. A., Cao, Y., Piro, A. L., et al. 2018, ApJ, 852, 100
Miller, J. S., & Stone, R. P. S. 1993, Lick Obs. Tech. Rep. 66, Lick Obs.,
   Santa Cruz
Milne, P. A., Brown, P. J., Roming, P. W. A., Bufano, F., & Gehrels, N. 2013,
   ApJ, 779, 23
Molnár, L., Pál, A., Plachy, E., et al. 2015, ApJ, 812, 2
Mulligan, B. W., & Wheeler, J. C. 2017, MNRAS, 467, 778
Mulligan, B. W., & Wheeler, J. C. 2018, MNRAS, 476, 1299
Munari, U., Henden, A., Belligoli, R., et al. 2013, NewA, 20, 30
Noebauer, U. M., Kromer, M., Taubenberger, S., et al. 2017, MNRAS,
  472, 2787
Nomoto, K. 1982, ApJ, 253, 798
Nomoto, K., Iwamoto, K., & Kishimoto, N. 1997, Sci, 276, 1378
Nugent, P., Phillips, M., Baron, E., Branch, D., & Hauschildt, P. 1995, ApJL,
  455, L147
Olling, R. P., Mushotzky, R., Shaya, E. J., et al. 2015, Natur, 521, 332
Pál, A. 2012, MNRAS, 421, 1825
Pál, A., Szabó, R., Szabó, G. M., et al. 2015, ApJL, 804, L45
Pan, Y.-C., Foley, R. J., Kromer, M., et al. 2015, MNRAS, 452, 4307
Parrent, J. T., Thomas, R. C., Fesen, R. A., et al. 2011, ApJ, 732, 30
Patat, F., Chandra, P., Chevalier, R., et al. 2007, Sci, 317, 924
Perlmutter, S., Aldering, G., Goldhaber, G., et al. 1999, ApJ, 517, 565
Pettini, M., & Pagel, B. E. J. 2004, MNRAS, 348, L59
Phillips, M. M., Lira, P., Suntzeff, N. B., et al. 1999, AJ, 118, 1766
Phillips, M. M., Simon, J. D., Morrell, N., et al. 2013, ApJ, 779, 38
Piro, A. L., & Morozova, V. S. 2016, ApJ, 826, 96
```

```
Piro, A. L., & Nakar, E. 2013, ApJ, 769, 67
Piro, A. L., & Nakar, E. 2014, ApJ, 784, 85
Plewa, T., Calder, A. C., & Lamb, D. Q. 2004, ApJL, 612, L37
Poole, T. S., Breeveld, A. A., Page, M. J., et al. 2008, MNRAS, 383, 627
Rest, A., Scolnic, D., Foley, R. J., et al. 2014, ApJ, 795, 44
Rest, A., Stubbs, C., Becker, A. C., et al. 2005, ApJ, 634, 1103
Riess, A. G., Casertano, S., Yuan, W., et al. 2018, ApJ, 855, 136
Riess, A. G., Filippenko, A. V., Challis, P., et al. 1998, AJ, 116, 1009
Riess, A. G., Macri, L. M., Hoffmann, S. L., et al. 2016, ApJ, 826, 56
Roming, P. W. A., Kennedy, T. E., Mason, K. O., et al. 2005, SSRv, 120, 95
Sand, D. J., Graham, M. L., Botyánszki, J., et al. 2018, ApJ, 863, 24
Scalzo, R., Aldering, G., Antilogus, P., et al. 2014a, MNRAS, 440, 1498
Scalzo, R. A., Aldering, G., Antilogus, P., et al. 2010, ApJ, 713, 1073
Scalzo, R. A., Ruiter, A. J., & Sim, S. A. 2014b, MNRAS, 445, 2535
Schaefer, B. E., & Pagnotta, A. 2012, Natur, 481, 164
Schlafly, E. F., & Finkbeiner, D. P. 2011, ApJ, 737, 103
Scolnic, D., Casertano, S., Riess, A., et al. 2015, ApJ, 815, 117
Seitenzahl, I. R., Kromer, M., Ohlmann, S. T., et al. 2016, A&A, 592, A57
Shappee, B. J., Holoinen, T. W.-S., Drout, M. R., et al. 2018b, ApJ, 870, 13
Shappee, B. J., Piro, A. L., Stanek, K. Z., et al. 2018a, ApJ, 855, 6
Shappee, B. J., Prieto, J. L., Grupe, D., et al. 2014, ApJ, 788, 48
Shappee, B. J., Stanek, K. Z., Pogge, R. W., & Garnavich, P. M. 2013, ApJL,
   762, L5
Silverman, J. M., & Filippenko, A. V. 2012, MNRAS, 425, 1917
Silverman, J. M., Ganeshalingam, M., Cenko, S. B., et al. 2012, ApJL, 756, L7
Silverman, J. M., Ganeshalingam, M., Li, W., et al. 2011, MNRAS, 410, 585
Silverman, J. M., Nugent, P. E., Gal-Yam, A., et al. 2013, ApJS, 207, 3
Silverman, J. M., Vinkó, J., Marion, G. H., et al. 2015, MNRAS, 451, 1973
Smartt, S. J., Valenti, S., Fraser, M., et al. 2015, A&A, 579, A40
Sollerman, J., Cox, N., Mattila, S., et al. 2005, A&A, 429, 559
```

Stanishev, V., Goobar, A., Benetti, S., et al. 2007, A&A, 469, 645

Sternberg, A., Gal-Yam, A., Simon, J. D., et al. 2011, Sci, 333, 856

```
Stritzinger, M., & Leibundgut, B. 2005, A&A, 431, 423
Stritzinger, M. D., Shappee, B. J., Piro, A. L., et al. 2018, ApJL, 864, L35
Taubenberger, S., Benetti, S., Childress, M., et al. 2011, MNRAS, 412, 2735
Thomas, R. C., Aldering, G., Antilogus, P., et al. 2007, ApJL, 654, L53
Thomas, R. C., Aldering, G., Antilogus, P., et al. 2011, ApJ, 743, 27
Tody, D. 1986, Proc. SPIE, 627, 733
Tody, D. 1993, adass II, 52, 173
Toonen, S., Nelemans, G., & Portegies Zwart, S. 2012, A&A, 546, A70
Valenti, S., Benetti, S., Cappellaro, E., et al. 2008, MNRAS, 383, 1485
Villanueva, S., Jr., Gaudi, B. S., Pogge, R. W., et al. 2018, PASP, 130, 015001
Vinko, J., Ordasi, A., Szalai, T., et al. 2018, PASP, 130, 064101
Wang, X., Filippenko, A. V., Ganeshalingam, M., et al. 2009b, ApJL, 699,
  L139
Wang, X., Li, W., Filippenko, A. V., et al. 2008, ApJ, 675, 626
Wang, X., Li, W., Filippenko, A. V., et al. 2009a, ApJ, 697, 380
Wang, X., Wang, L., Filippenko, A. V., Zhang, T., & Zhao, X. 2013, Sci,
  340, 170
Waters, C. Z., Magnier, E. A., Price, P. A., et al. 2016, arXiv:1612.05245
Webbink, R. F. 1984, ApJ, 277, 355
Welty, D. E., Ritchey, A. M., Dahlstrom, J. A., & York, D. G. 2014, ApJ,
  792, 106
Wheeler, J. C., Johnson, V., & Clocchiatti, A. 2015, MNRAS, 450, 1295
Whelan, J., & Iben, I., Jr. 1973, ApJ, 186, 1007
Williams, G. G., Milne, P. A., Park, H. S., et al. 2008, in AIP Conf. Ser. 1000,
  Gamma-Ray Bursts 2007 (Melville, NY: AIP), 535
Yaron, O., & Gal-Yam, A. 2012, PASP, 124, 668
Zhai, Q., Zhang, J.-J., Wang, X.-F., et al. 2016, AJ, 151, 125
Zhang, J., Xin, Y., Li, W., et al. 2018, ATel, 11267
Zhang, K., Wang, X., Zhang, J., et al. 2016, ApJ, 820, 67
Zhao, X., Maeda, K., Wang, X., et al. 2016, ApJ, 826, 211
Zhao, X., Wang, X., Maeda, K., et al. 2015, ApJS, 220, 20
Zheng, W., Silverman, J. M., Filippenko, A. V., et al. 2013, ApJL, 778, L15
```